

FINITE ELEMENT MODELING OF BLAST-INDUCED TRAUMATIC BRAIN INJURY

by

Chenzhi Wang

B.E., Nanjing University of Science and Technology, 2006

M.E., Nanjing University of Science and Technology, 2008

Submitted to the Graduate Faculty of
Swanson School of Engineering in partial fulfillment
of the requirements for the degree of
Doctor of Philosophy

University of Pittsburgh

2013

UNIVERSITY OF PITTSBURGH
SWANSON SCHOOL OF ENGINEERING

This dissertation was presented

by

Chenzhi Wang

It was defended on

September 11th, 2013

and approved by

Carey D. Balaban, PhD, Professor, Departments of Otolaryngology, Neurobiology,
Communication Science & Disorders, and Bioengineering

Mark C. Miller, PhD, Associate Research Professor, Department of Mechanical Engineering
& Materials Science

Xudong Zhang, PhD, Associate Professor, Department of Mechanical Engineering &
Materials Science

Dissertation Director: Jeffrey S. Vipperman, PhD, Associate Professor, Department of
Mechanical Engineering & Materials Science

Copyright © by Chenzhi Wang

2013

FINITE ELEMENT MODELING OF BLAST-INDUCED TRAUMATIC BRAIN INJURY

Chenzhi Wang, PhD

University of Pittsburgh, 2013

Human exposure to a blast wave itself without any fragment impact can still result in primary blast-induced traumatic brain injury (bTBI). To investigate the mechanical response of human brain to primary blast waves and to identify the injury mechanisms of bTBI, a three-dimensional finite element head model consisting of the scalp, skull, cerebrospinal fluid, nasal cavity, and brain was developed from the imaging data set of a human head. The finite element head model was implemented with material models and was partially validated against a published cadaveric experiment.

This study included three scenarios of blast-head interaction simulations using the same five TNT doses: the simulations of head exposures to the blast waves coming from three horizontal orientations (anterior, right lateral, posterior), to the blast waves generated from the explosives laid on the ground, and to the blast waves within a small room. For the horizontal blast-head simulations, the influences of the blast levels and exposure orientations on the pressure and shear stress responses of brain were analyzed. For the simulation scenarios of the ground blasts and the room blasts, the influences of the blast levels and the blast wave reflections on the pressure and shear stress responses of brain were assessed. The patterns of intracranial pressure waves and the high-pressure locations were investigated. Based on a published pressure-based injury criterion of cerebral contusion, the locations and injury severities of cerebral contusion for every simulation scenario were predicted. High von-Mises stresses were

found on the cortex, brainstem, and spinal cord in every simulation. However, it was predicted that diffuse axonal injury (DAI) did not occur in any simulation using a DAI criterion based on von-Mises stress.

The mechanical properties of human bridging vein in an anisotropic, hyperelastic constitutive model were obtained by fitting the data of an inflation test of a real human bridging vein to the analytical equation of the inflation test. The obtained mechanical properties were implemented in the finite element analysis of bridging vein rupture to predict the blast-induced subdural hemorrhage by using the peak CSF pressures at the SSS of the anterior blast-head simulations as the loading conditions.

TABLE OF CONTENTS

TABLE OF CONTENTS	VI
LIST OF TABLES	VIII
LIST OF FIGURES	IX
PREFACE.....	XII
1.0 INTRODUCTION.....	1
1.1 MOTIVATION	1
1.2 BACKGROUND	4
1.3 LITERATURE REVIEW ON NUMERICAL SIMULATIONS OF TBI	9
1.4 OVERVIEW OF RESEARCH PROCEDURES	12
2.0 FINITE ELEMENT HEAD MODELING.....	15
2.1 HEAD GEOMETRIC MODELING AND FINITE ELEMENT DISCRETIZATION	16
2.2 MATERIAL MODELING OF HEAD.....	24
2.3 VALIDATION OF FINITE ELEMENT HEAD MODEL	28
3.0 NUMERICAL IMPLEMENTATION OF SIMULATIONS OF BLAST-HEAD INTERACTIONS.....	33
3.1 MATERIAL MODELS OF EXPLOSIVES AND AIR	33
3.2 NUMERICAL FORMULATIONS	35

3.3	MODELING PROCEDURES OF BLAST-HEAD SIMULATION	39
4.0	BLAST-HEAD INTERACTION SIMULATIONS OF HORIZONTAL EXPOSURE TO BLAST	45
4.1	PREPROCESSING OF SIMULATIONS	45
4.2	BRAIN PRESSURE RESPONSE TO HORIZONTAL BLAST.....	49
4.3	BRAIN SHEAR STRESS RESPONSE TO HORIZONTAL BLAST	64
5.0	BLAST-HEAD INTERACTION SIMULATIONS OF EXPOSURE TO GROUND BLAST.....	70
5.1	PREPROCESSING OF SIMULATIONS	70
5.2	BRAIN PRESSURE RESPONSE TO GROUND BLAST.....	73
5.3	BRAIN SHEAR STRESS RESPONSE TO GROUND BLAST	81
6.0	BLAST-HEAD INTERACTION SIMULATIONS OF EXPOSURE TO BLAST IN A SMALL ROOM	87
6.1	PREPROCESSING OF SIMULATIONS	87
6.2	BRAIN PRESSURE RESPONSE TO BLAST IN A SMALL ROOM.....	90
6.3	BRAIN SHEAR STRESS RESPONSE TO BLAST IN A SMALL ROOM	99
7.0	FINITE ELEMENT ANALYSIS OF SUBDURAL HEMORRHAGE.....	104
7.1	MECHANICAL TESTING OF HUMAN BRIDGING VEIN.....	104
7.2	CONSTITUTIVE MODELING AND MATERIAL CURVE FITTING OF BRIDGING VEIN	107
7.3	INJURY PREDICTION OF SUBDURAL HEMORRHAGE.....	112
8.0	CONCLUSIONS AND DISCUSSIONS	116
	BIBLIOGRAPHY	124

LIST OF TABLES

Table 2-1. Number of every element type in each of the anatomical components of the FE human head model	19
Table 2-2. Constitutive models and associated material parameters of FE human head model for this study	28
Table 3-1. Material parameters of TNT explosive.....	34
Table 4-1. Predicted contusion injury severities at typical cerebral sites with respect to impinging BOPs at the blast incident side in the anterior blast-head simulations	60
Table 4-2. Predicted contusion injury severities at typical cerebral sites with respect to impinging BOPs at the blast incident side in the right lateral blast-head simulations	61
Table 4-3. Predicted contusion injury severities at typical cerebral sites with respect to impinging BOPs at the blast incident side in the posterior blast-head simulations	62
Table 5-1. Pressure ranges in kPa at various cerebral locations: No. 3 (cortex at SSS), No. 6 (frontal cortex), No. 11 (brain parenchyma), No. 14 (occipital cortex), No. 19 (lower brainstem), No. 21 (hypothalamus), No. 22 (right temporal cortex)	78
Table 5-2. Peak von-Mises stresses in kPa at frontal cortex (gauge No. 6), occipital cortex (gauge No. 14), right temporal cortex (No. 22) of the five simulations cases.....	86
Table 6-1. Predicted contusion injury severities at typical cerebral sites with respect to impinging BOPs at the blast incident side in the room blast-head simulations	98
Table 7-1. Material parameters of human bridging vein	111
Table 7-2. Peak pressure tracked by the gauge No. 2 in the CSF at SSS, and the respective maximum axial Cauchy stress and failure prediction of the BV with respect to the impinging BOP at the blast incident side	115

LIST OF FIGURES

Figure 1-1. Ideal Friedlander wave (Bauman et al. 2009)	5
Figure 1-2. The most common cerebral locations of contusion (blue) and subdural hemorrhage (purple) (Taber et al. 2006).....	6
Figure 1-3. Human cerebral bridging veins in the superior sagittal sinus (SSS) on a lateral view of a cadaver (Han et al. 2007).....	6
Figure 2-1. The three-dimensional finite element model of scalp: (a) Overall view, (b) Sagittal cross-sectional view showing the internal details.....	20
Figure 2-2. The three-dimensional finite element model of skull: (a) Overall view, (b) Transverse cross-sectional view showing the internal details.....	21
Figure 2-3. Three-dimensional finite element models of CSF and nasal cavity.....	22
Figure 2-4. Three-dimensional finite element model of brain: (a) Overall view of brain model, (b) Bottom view showing the cerebrum, cerebellum, brainstem, and spinal cord.....	23
Figure 2-5. Validation of the FE head model by applying the measured input force of Nahum's experiment.....	30
Figure 2-6. Comparison between the pressure-time histories of simulation and Nahum's cadaveric test at (a) Frontal cortex and (b) Posterior fossa.....	32
Figure 3-1. (a) 2D 450g TNT air-blast model was remapped into the Euler-FCT grid of the air space model in order to form (b) the complete 3D blast-head model of 450g TNT.....	43
Figure 3-2. Locations of gauges: (a) Sagittal cross-sectional view, (b) Transverse cross-sectional view.....	44
Figure 4-1. (a) The five surfaces of the air space were assigned with the open boundary condition indicated by orange color, (b) The FE head model was exposed to the blasts from the anterior, posterior, and right lateral horizontal orientations.....	48

Figure 4-2. Blast wave propagating through the head during the first 0.5 ms of the 250g TNT blast-head simulation of the anterior blast scenario: (a) 0.2 ms, (b) 0.4 ms, (c) 0.5 ms, (d) 0.75 ms 50

Figure 4-3. Pressure-time histories recorded by various gauge points for the anterior blast-head simulations: (a) No. 24 in atmosphere (b) No. 2 in the CSF at SSS, (c) No. 6 on the frontal cortex, (d) No. 14 in the occipital cortex, (e) No. 18 at the posterior margin of the tentorium cerebelli, (f) No. 19 on the lower brainstem 52

Figure 4-4. Pressure distributions of the brain in the 400g TNT blast-head simulations of all blast orientations..... 56

Figure 4-5. Predicted contusion injury location and severity of the anterior blast-head simulations 60

Figure 4-6. Predicted contusion injury location and severity of the right lateral blast-head simulations 61

Figure 4-7. Predicted contusion injury location and severity of the posterior blast-head simulations 62

Figure 4-8. von-Mises stress time histories of the gauge points No. 6 (frontal cortex), No. 14 (occipital cortex), No. 22 (right temporal cortex), and No. 23 (left temporal cortex) in the 450g TNT blast-head simulation cases: (a) Anterior blast orientation, (b) Right lateral blast orientation, (c) Posterior blast orientation..... 67

Figure 4-9. von-Mises stress time-histories of gauge No. 19 at lower brainstem and the associated von-Mises stress distributions showing peak von-Mises stresses in the 450g TNT blast-head simulation cases: left - anterior orientation (2.45 ms), middle - right lateral orientation (1.85 ms), right - posterior orientation (3.43 ms) 68

Figure 5-1. Ground blast exposure simulation scenario: (a) 3D view, (b) Y-Z plane view 72

Figure 5-2. Blast wave propagating during the first 1.2 ms of the 250g TNT ground blast-head simulation..... 74

Figure 5-3. Pressure distributions of the brain in the 250g TNT ground blast-head simulation from 1.3 ms to 1.8 ms 75

Figure 5-4. Pressure-time histories recorded by various gauge points of the five ground blast-head simulations: (a) No. 24 in atmosphere (b) No. 2 in the CSF at SSS, (c) No. 6 on the frontal cortex, (d) No. 14 on the occipital cortex, (e) No. 19 on the lower brainstem, (f) No. 21 on the hypothalamus 77

Figure 5-5. Distributions of von-Mises stress of the brain were shown in the sagittal cross-sectional view for the 250g TNT ground blast-head simulation at different times from 1.6 ms to 2.1 ms.....	82
Figure 5-6. The time histories of von-Mises stress recorded by various gauge points of the five ground blast-head simulations: (a) No. 3 on cortex at SSS, (b) No. 6 on the frontal cortex, (c) No. 14 on the occipital cortex, (d) No. 19 on the lower brainstem, (e) No. 21 on the hypothalamus, (f) No. 22 on the right temporal cortex	83
Figure 6-1. Computational schematic of 3D air blast within the small room which was assigned with open boundary condition (B.C.) at the anterior surface.....	89
Figure 6-2. Time-lapse contours of a blast wave propagating within the room at 2.0 ms, 3.0 ms, 4.0 ms, 4.5 ms, 5.0 ms and at 8.0 ms for the 250g TNT room blast-head simulation	91
Figure 6-3. Atmospheric pressure time histories tracked by (a) the air gauge point No. 24 in the frontal space of the head model, (b) the air gauge point No. 25 in the rear space of the head model.....	92
Figure 6-4. Pressure-time histories recorded by various gauge points for the room blast-head simulations: (a) No. 2 in CSF at SSS, (b) No. 6 in the frontal cortex, (c) No. 14 in the occipital cortex, (d) No. 18 at the posterior margin of the tentorium cerebelli, (e) No. 19 on the lower brainstem, (f) No. 22 on the right temporal cortex	95
Figure 6-5. Pressure distributions of the brain in the 400g TNT room blast-head simulation from 4.5 ms to 5.0 ms	96
Figure 6-6. Predicted contusion injury location and severity of the room blast-head simulations	98
Figure 6-7. Distributions of von-Mises stress in the sagittal cross-sectional view of the brain for the 400g TNT room blast-head simulation at different times from 4.5 ms to 5.0 ms	100
Figure 6-8. The time histories of von-Mises stress recorded by various gauge points for the room blast-head simulations with five amounts of TNT: (a) No. 3 on cortex at SSS, (b) No. 6 on the frontal cortex, (c) No. 14 on the occipital cortex, (d) No. 19 on the lower brainstem, (e) No. 21 on the hypothalamus, (f) No. 22 on the right temporal cortex.....	102
Figure 7-1. Human bridging vein mounted in the inflation-extension vascular testing system (Wang et al. 2012).....	106
Figure 7-2. Experimental data and analytical solution from fitted material parameters	111
Figure 7-3. Axial Cauchy stress of the bridging vein finite element analysis corresponding to impinging BOP at the blast incident side: (a) 291 kPa, (b) 321 kPa, (c) 349 kPa, (d) 379 kPa, (e) 413 kPa.....	114

PREFACE

I would like to thank my advisor, Dr. Jeffrey S. Vipperman, sincerely for his guidance and supervision. His profound knowledge, patient guidance, and constant encouragement were the biggest driving forces to make this dissertation appear. I would like to thank Dr. Carey D. Balaban for his research suggestions, providing the bridging vein samples, and for teaching me the anatomy of human head and the pathology of blast-induced traumatic brain injury. I sincerely thank Dr. Jae Bum Pak and Adam R. Wood for their collaborations on the 3D modeling of human head. I would express my appreciation to Dr. Mark C. Miller for his help on revising the research proposal which was eventually granted by NSF to support me. I thank Dr. David A. Vorp and Joseph E. Pichamuthu for their help on the experiments of human bridging veins.

I thank Dr. Xudong Zhang, Dr. Mark C. Miller, and Dr. Carey D. Balaban for serving on my dissertation committee and their invaluable comments.

I thank Dr. Kai Liu, Ms. Yali Yang, and all my friends who help me during my living in Pittsburgh.

My deeply thanks to my wife Weiwei Jiao, my father Shaoqing Wang, my mother Shuling Qiu, my father in law Jie Jiao, and my mother in law Chunling Wang, for their love, understanding, help, and encouragement.

1.0 INTRODUCTION

1.1 MOTIVATION

The number of civilians and army personnel diagnosed with blast-induced traumatic brain injury (bTBI) has increased significantly due to the growing use of the improvised explosive devices (IEDs) in the current conflicts and terrorist activities at Iraq and Afghanistan. Improvement in protection devices and medical treatment has also contributed to the lowest mortality of the people who experienced blast assaults. IED detonation can produce primary blast wave and high-velocity fragments. The brain injury resulting from the primary blast waves, the impacts of blast-propelled fragments, the collisions between blast-propelled people and stagnant object are categorized to primary, secondary, and tertiary bTBI, respectively.

The clinical observations have led to the hypothesis that bTBI is a stress wave dominated phenomenon as opposed to impact/acceleration/deceleration-induced brain injury, typically encountered in automobile and sports accidents (DePalma et al. 2005, Taber et al. 2006). Cerebral contusion, subdural hematoma (SDH), and diffuse axonal injury (DAI) are the major injury types of bTBI (Taber et al. 2006, Kocsis and Tessler 2009). The challenge in determining the mechanism of primary bTBI comes from the difficulties in measuring the injury process of bTBI *in vivo* and from the difficulty of distinguishing the blast wave dominated brain injury from other types of injuries in the chaotic environment of the battlefield. Rigorous

epidemiological studies are not available so far. Cerebral contusion and diffuse cerebral edema have been reported in the clinical cases of primary bTBI detected by CT or MRI (Benzinger et al. 2009). Case reports have shown intracranial hemorrhage including subdural hematoma happened following IED blast and industrial explosion accident (Murthy et al. 1979, Ling et al. 2009). However clinical studies are not able to fully explain the precise neuropathology of primary bTBI. So far, much of what we know about bTBI was determined from animal studies (Bauman et al. 2009, Long et al. 2009, Cheng et al. 2010). These studies have helped researchers better understand the pathology of bTBI, but the findings still have not explained well the detailed mechanisms of bTBI. Moreover, the results of animal studies are not able to parametrically interpret the injury mechanism of human bTBI due to the geometrical differences. However, the development of protection device and medical treatment requires a clear understanding of the injury mechanisms of bTBI. In biomechanical engineering, finite element (FE) modeling and simulation, serving as an alternative to experiment, is able to help understand the biomechanical details and to increase research efficiency.

The primary goal of this study is to understand the biomechanical mechanisms of blast-induced traumatic brain injury using finite element modeling and simulation. Three FE simulation scenarios of blast waves and head interactions including the horizontal blast-head interaction simulations, the ground blast-head interaction simulations, and the room blast-head interaction simulations were taken in this dissertation with the motivation to investigate the mechanism, injury occurrence possibility, and potential injury severity of cerebral contusion, diffuse axonal injury, and subdural hematoma (bSDH). The horizontal blast-head interaction simulations reproduced the human brain exposures to blast waves from the anterior, right lateral, and posterior orientations, and were motivated to evaluate the sensitivity of brain responses to

various pathways of blast waves. The simulations of human head exposures to the blast waves generated near the ground were developed with the motivation to evaluate the brain response of a standing person to a blast wave generated by an IED and to predict whether ground blasts with the same explosive charges as the horizontal blast-head simulations could lead to more severe brain injuries. The simulations of human head exposures to the blast waves loaded in a room were built in order to evaluate the effects of the wall reflections of blast waves on the cerebral mechanical responses. The obtained intracranial pressures and von-Mises stresses can help to understand the biomechanical behaviors of brain subjected to blast waves and the brain sensitivities to various blast factors.

There is currently a lack of fundamental understanding in the literature about the mechanism of blast-induced human bridging vein rupture. In order to study the blast-induced subdural hemorrhage, known to be caused by bridging vein rupture, an experimental approach on a human bridging vein segment was taken in this dissertation to calibrate the mechanical properties of bridging vein by measuring the intraluminal pressure and diameter of the bridging vein under the internal fluid inflation. The material parameters related to an anisotropic hyperelastic constitutive model were calculated by using a nonlinear regression method which fitted the results of bridging vein inflation experiment to the constitutive model. The injury severities of subdural hemorrhage in the anterior blast-head simulations, which were concluded as the most injurious case, were evaluated by implementing the calculated material parameters to the finite element analysis of bridging vein rupture.

1.2 BACKGROUND

Blast-induced traumatic brain Injury (bTBI), called as the signature injury of the wars in Iraq and Afghanistan (Elder and Cristian 2009), is more prevalent nowadays due to the intensive use of improvised explosive devices (IED). Some recent reports estimated that a significant number of service members had been affected by TBI, for example, the study of RAND company estimated 320,000 TBIs from a total number of 1.64 million US Armed forces deployed since 9/11 (Tanielian and Jaycox 2008). Mild TBI constituted 10-20% of the cases of those service members diagnosed as TBI positive (Moore et al. 2009). Unlike previous wars, improved battlefield medical care and improved body armor significantly reduced the mortality rate of the service members who experienced blasts (Chen and Huang 2011). However, the soldiers survived the exposures to blasts are suffering blast-induced traumatic brain injury (bTBI). The primary bTBI is the cerebral lesion caused by the direct effects of the blast-generated blast waves propagating through the head.

When an explosion occurs, ambient pressure rises sharply and forms a blast wave, a shock front of high atmospheric pressure (positive impulse) higher than the standard atmospheric pressure. As the initial overpressure wave dissipates, ambient pressure plummets, causing a negative pressure impulse that is lower than the ambient pressure (Taber et al. 2006). This negative impulse in atmosphere attracts the air from the areas of normal pressure, therefore causes a reversed blast wind toward the low pressure area. The pressure-time history of blast wave is described by the ideal Friedlander wave which has positive phase and negative phase (Figure 1-1).

It is believed that over-pressurization waves cause hemorrhages and diffuse neuronal damage throughout the brain, therefore inducing neurological dysfunction (Taber et al. 2006,

Kocsis and Tessler 2009). Headache, hearing impairment, and balance dysfunction are the major symptoms of mild TBI that occur acutely after exposure to low level blasts. Mild TBI impedes its sufferers returning to normal activities, and can persist chronically (Hoge et al. 2008 , Terrio et al. 2009, Hoffer et al. 2010, Hoffer et al. 2013). Blast over-pressurization waves instantaneously increase pressure in body tissues, forming pressure waves traveling in the intracranial tissues. Once the resultant stresses in the intracranial tissues exceed the tolerable threshold, traumatic brain injury occurs.

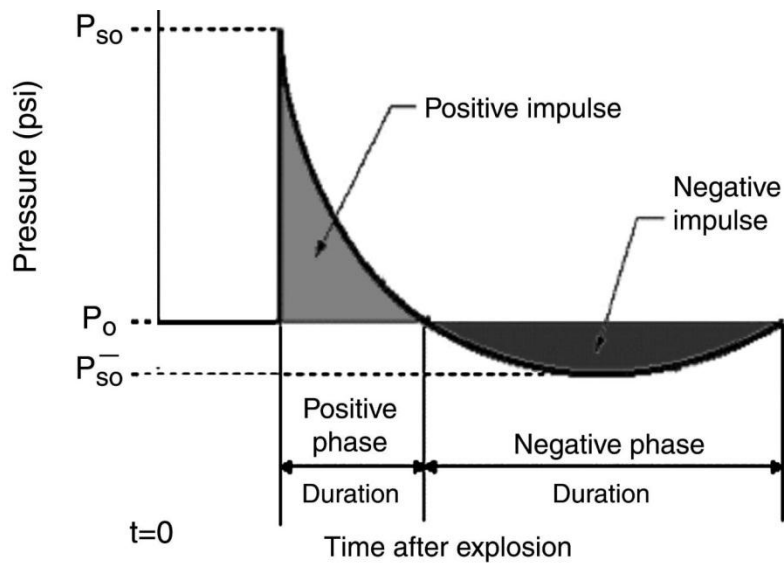


Figure 1-1. Ideal Friedlander wave (Bauman et al. 2009)

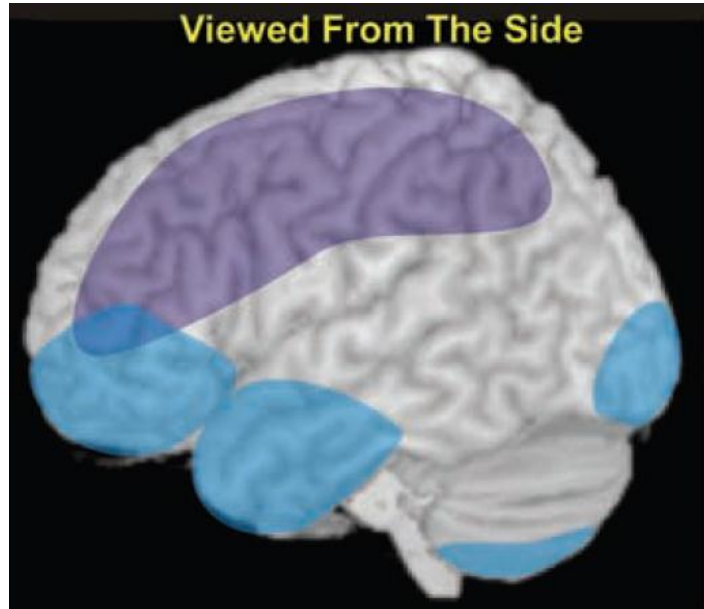


Figure 1-2. The most common cerebral locations of contusion (blue) and subdural hemorrhage (purple) (Taber et al. 2006)

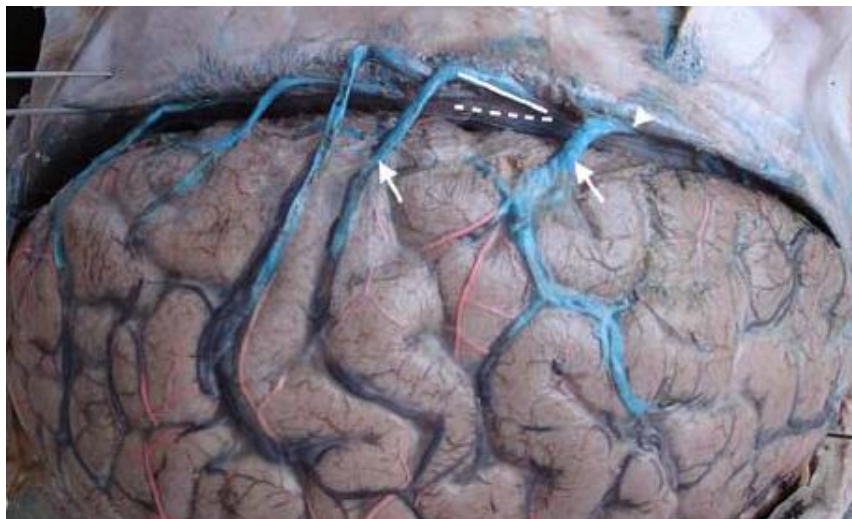


Figure 1-3. Human cerebral bridging veins in the superior sagittal sinus (SSS) on a lateral view of a cadaver (Han et al. 2007)

Although the pathophysiology of blast-related TBI is very complicated and has not been fully understood, it is thought that the rapid ambient pressure changes lead to traumas such as concussion, subdural hematoma (SDH), and diffuse axonal injury (DAI) (Taber et al. 2006, Kocsis and Tessler 2009). Figure 1-2 shows that contusion has the most common locations at the inferior, lateral, and anterior cortex of the frontal and temporal lobes, and that subdural hemorrhage commonly occurs at the frontal and parietal convexities (Taber et al. 2006). The subdural space contents appear to be particularly vulnerable to over-pressurization damage. Subdural hemorrhage, known as the bleeding between the dura matter and the arachnoid matter, is caused by the rupture of bridging veins (Figure 1-3) which cross the subdural space. Diffuse axonal injury is a type of shear-induced injury, resulting from the disruption of axons and small vessels. The cortico-medullary (gray matter-white matter junctions) is particular vulnerable to the shearing and stretching forces (Taber et al. 2006).

The experimental studies of both large and small animals provide important data to help identify the pathophysiological characteristics of bTBI. Several animal studies found evidence supporting that cerebral contusion, diffuse axonal injury, and subdural hematoma/hemorrhage are the major pathophysiological characteristics of bTBI. Most of large-animal models of blast injury utilized chemical explosives as the source of blast wave (Saljo et al. 2008, Bauman et al. 2009), while the majority of small-animal studies (Long et al. 2009, Rafaels et al. 2011, Sundaramurthy et al. 2012) utilized compressed air-driven shock tubes to produce shock waves.

In the study of Saljo et al. (2008), pigs were exposed to the controlled blasts which simulated real battlefield blast scenarios such as the explosions generated by howitzer, bazooka, automatic rifle in free field, the explosions in an enclosure, and underwater blasts. The rats were exposed to blast waves generated by a shock tube. Pressure-time histories recorded by the gauges

within the pig brains in the howitzer experiments were found to have a strong similarity with those in air. Macroscopic examinations revealed that subdural hemorrhages were observed in 21% of the animals exposed to the automatic rifle in free field and in 7% of those exposed to the bazooka. Histological examination of porcine brains also revealed that small parenchymal and subarachnoid hemorrhages predominated in the occipital lobe, cerebellum, and medulla oblongata/lower brainstem.

Bauman et al. (2009) used a bi-directionally open-ended blast tube, a surrogate of a HUMVEE crew-compartment, a building consisted of four walls without roof, to perform blast experiments on swines. The blast tube included the heavy-walled driver chamber where the chemical explosives were immobilized, the expansion cone, and the test section in which swine was restrained to sustain blasts from different distances. The angiography data reported by the blast-tube experiment indicated that the emergence of vasospasm was one salient pathophysiological characteristic of exposure to explosion.

Long et al. (2009) studied the striking neuro-pathological changes of rat brains exposed to the 126 and 147 kPa air blasts by using a shock tube. Rats exposed to the 147 kPa air blast had prominent areas of cortical cell loss, gliosis, and infiltration, along with extensive fiber degeneration shown by histological studies of rat brain slices. The rat brains in the 126 kPa air blast did not show any cell loss despite extensive fiber degeneration.

Cheng et al. (2010) developed a unique blast on rat model to simulate the blast effects on brain. An electric detonator with the equivalent of 400 mg TNT was developed as the explosive source while the rat was fixed in the specially designed cabin in which the restricted rat brain could only be exposed to the blast wave. Capillary damage, enlarged intercellular and vascular

space in the cortex, diffuse subarachnoid hemorrhage, edema, and degeneration of nerve fibers were observed.

Rafaels et al. (2011) exposed twelve male New Zealand white rabbits whose bodies were protected by test fixtures to shock waves. Histological evaluation revealed subdural and subarachnoid hemorrhages in the nonresponsive respiratory-arrested specimens. Cerebral contusion, subdural hemorrhage, and subarachnoid hemorrhage occurred together in all non-surviving specimens. Injury risk was evaluated by scaling techniques on the blast over-pressure and duration combinations.

Sundaramurthy et al. (2012) examined the role of animal placement location along the length of the shock tube in which rats were placed to measure the surface and intracranial pressures. In addition, they developed an anatomically accurate rat head model to simulate blast effects on rats under the same experimental conditions.

1.3 LITERATURE REVIEW ON NUMERICAL SIMULATIONS OF TBI

A number of finite element head models have been created by researchers to study bTBI. Taylor and Ford (2009) developed a finite element head model consisting of skull, white matter, gray matter, CSF and air in sinuses by segmenting a data set of high resolution photographic images. The direct exposure of this head model to a blast wave of 1.3 MPa peak pressure from anterior, posterior, and lateral directions were simulated for 2 ms, showing focal areas of elevated pressure, volumetric tension, and deviatoric stress in the brain. The authors concluded that multifocal axonal injury might happen due to stress localization initially before the onset of any linear or angular acceleration. Chafi et al. (2009) simulated the blast loadings of three different

TNT amounts on a finite element head model comprised of brain, falx and tentorium, CSF, dura matter, pia matter, skull bone, and scalp for up to 5 ms, and predicted significant positive and negative pressures alternating at the coup and contrecoup sites. They assessed the possibility of bTBI using three different injury predictors based on intracranial pressure (ICP), shear stress, and principal strain. Moore et al. (2009) used an numerical head model which is based on MRI images for three simulations of a 5.2 atmosphere pressure blast, an 18.6 atmospheric pressure blast, and a 5m/s impact on a head. The highest pressures and stresses experienced were located at the right temporal region, for which the blast wave was incident. The results suggested that the blast effects on the head of a 50% lethal dose of blast lung injury were comparable to the concussive impact injury. Grujicic et al. (2010) developed a finite element head model assembled with a helmet to study the mitigation effect of the advanced combat helmet against blast. By comparing the simulation results using the helmet protected head and unprotected head, it was concluded that the current combat helmet did provide some level of protection against mild bTBI. By using the same finite element head model, Grujicic and his colleagues also studied the effects of using polyurea as the helmet pad material to protect human heads from blast (Grujicic et al. 2010). Nyein et al. (2010) developed a FE head model based on the geometric segmentation of MRI images, and studied the intracranial pressure and von-Mises stresses of the head under three conditions: unprotected head, head protected by a helmet, and the head protected by both helmet and face shield. Head exposure to an anterior blast wave with an incident overpressure of 10 atm was simulated for each of the conditions. It was suggested that the existing combat helmet did not significantly mitigate blast harmfulness, but did not worsen it either. In contrast, the harmfulness of blast wave was reduced by combinative use of the helmet and face shield. Ganpule et al. (2012) simulated the blast wave-head interactions as

the blast wave traversed the finite element head model consisting of the skin, skull, subarachnoidal space, and brain. They also built a shock tube to test the surface effects of blast wave impinging on a dummy head. The measured surface pressure of the dummy head model was used to validate their numerical simulations. It was concluded that the “coup and contrecoup” injury patterns encountered in impact TBI also occurred in their blast-head simulations.

There also had been a long history of finite element modeling of human head to study impact-induced TBI before the computational studies of bTBI sprung up recently. Ruan (1994) built a FE head model using pure hexahedral elements and investigated the model sensitivities to various material models and to various loading characteristics of impacts. Zhang et al. (2001) investigated the human brain responses to the frontal and lateral impacts to study the directional sensitivity by using a partially validated three-dimensional finite element head model (WSUBIM) with various anatomic structures. Later on, combining the results of finite element studies and actual field accident data, Zhang et al. (2004) derived the injury threshold of impact-induced cerebral contusion based on the predicted intracranial pressures using a pressure-based contusion criterion (Ward et al. 1980). Zhang et al. (2004) also derived the injury threshold of diffuse axonal injury based on von-Mises shear stress in the midbrain of the brainstem. Kleiven (2006) investigated the brain responses to impacts of different directions and durations by using an experimentally validated finite element head model comprised of the scalp, skull, brain, meninges, CSF, and simplified models of eleven pairs of parasagittal bridging veins. Sayed et al. (2008) studied diffuse axonal injury and brain cavitation due to impact using a partially validated finite element human head model. A novel constitutive model capable of capturing the cerebral damage mechanisms was developed for the head modeling. Although the injury mechanism of

impact TBI is distinct from that of bTBI, the mechanical properties used in the computational studies of impact TBI were often used by the computational studies of bTBI (Chafi et al. 2009, Moss et al. 2009, Taylor and Ford 2009, Ganpule et al. 2012).

1.4 OVERVIEW OF RESEARCH PROCEDURES

The primary objective for this research is to find out the injury severity of the blast-induced traumatic brain injury under the blast loadings from various blast scenarios of five different explosive charges using the methods of finite element modeling and simulation.

In the first stage of this study, an anatomically correct human head model was generated from the segmentation of a high resolution MRI data set of a real human head. The head model was constituted by five major anatomical structures: scalp, skull, nasal cavity, cerebrospinal fluid, and brain matter. The segmented 3D head model was meshed by the Lagrangian meshing algorithm as volume meshes. State of art constitutive relations were adopted for the material modeling of the FE head model. In order to verify the accuracy of FE head model, the FE head model was numerically validated against the frontal cadaveric impact experiment of Nahum et al. (1977). The loading and boundary conditions of the head model in the validation simulation were applied according to the protocol of the cadaveric experiment. The frontal pressure-time history in the validation simulation was compared with that measured at the same gauge location in the Nahum's cadaveric experiment to evaluate the predictive accuracy of the FE head model.

After the FE head model was numerically validated, the FE head model was immersed into the numerical air space model for the further simulations of blast wave loading on the head. The air space model was developed as a 3m by 1.8m by 3m cuboid volume which was

discretized as an Eulerian region in order to allow the numerical treatment of the formation and propagation of primary blast waves. The air space model was assigned with the material properties of ideal air which were described by the equation of state. Three scenarios of blast-head interaction simulations involving the horizontal blast-head scenario, the ground blast-head scenario, and the room blast-head scenario using the 250g, 300g, 450g, 400g, and 450g TNT charges. The finite element simulations of blast-head simulations were solved using the commercial explicit finite element package ANSYS AUTODYN[®] (ANSYS 2012) with its embedded Euler-Lagrangian coupling method for the fluid-structure interaction (FSI). For each TNT weight, the three horizontal blast-head simulation sets and the room blast-head simulation scenario predicted the same impinging blast overpressure (BOP) at the blast incident side. The pressure time histories and von-Mises stress time histories at various intracranial locations were tracked for the simulations in each blast-head simulation scenario. The patterns of pressure distributions and von-Mises stress distributions in the brain were studied. The sensitivities of brain mechanical responses to the blast factors including the blast intensities, blast orientations, blast wave reflections by the ground and room walls were investigated. How the predicted intracranial pressures and von-Mises stresses were related to the blast waves was discussed for each blast-head simulation scenario. The predicted intracranial pressures and von-Mises stresses at several cerebral locations helped to evaluate the occurrences and severities of cerebral contusion and diffuse axonal injury based on the published injury criterions. The predicted injury severities of contusions at various cerebral locations in the horizontal blast-head simulations and the room blast-head simulations were related to the predicted impinging BOPs at the proximal side to blast. The relative skull and brain motion was predicted to be nearly zero in every blast-head simulation. The peak positive pressures in the CSF at the superior sagittal sinus (SSS) were

speculated to be the main mechanical causation of the bridging vein rupture which led the subdural hematoma. The anterior blast-head simulations and the ground blast-head simulations had the most injurious cases of subdural hemorrhage. In addition, they have the same values of peak positive pressures in the CSF at the SSS, therefore, the finite element analyses of subdural hemorrhage were only based on the results of the anterior blast-head simulations.

Due to the fact that there was no reported experimental data on human cerebral bridging veins to derive the accurate material properties, vascular inflation experiments were conducted in this study on a human bridging vein sample to obtain the data of the relationship between the inflating pressure and the vascular outer diameter. This experimental data was essential for the calculations of the material parameters in a selected anisotropic constitutive model, known as the Holzapfel-Gasser-Ogden model (Holzapfel et al. 2000), in order to numerically model the nonlinear mechanical behavior of human bridging veins. The material parameters of human bridging vein were calculated by fitting the experimental results to the Holzapfel-Gasser-Ogden model using the nonlinear regression analysis.

A series of separate finite element analyses of bridging vein rupture for the anterior blast-head simulations, concluded to be the most injurious cases, were carried out using an axisymmetric finite element bridging vein model assigned with the calculated material parameters. The predicted maximum axial Cauchy stresses of bridging vein were compared with the yielding criterion of bridging vein to forecast the injury occurrence of the blast-induced subdural hemorrhage.

2.0 FINITE ELEMENT HEAD MODELING

This chapter describes the details of the geometric development of the 3D head model, the procedure of finite element discretization of the head geometric model, and the constitutive modeling of each of the anatomical components of the FE head model. One of the main efforts to build the FE head model was the development of the three-dimensional geometric model reflecting the real anatomy of human head. The three dimensional geometry was created from the two-dimensional magnetic resonance imaging (MRI) files of a real human head. Once the geometry of a human head was established, it was imported into the finite element meshing tool ANSYS ICEM-CFD[®] (ANSYS 2012) to be spatially discretized into a finite element grid. Before using the FE head model for the blast simulations, it is essential to clarify the numerical accuracy of the FE head model which was constituted by the finite element grid and the material models. Although the cadaveric experiments of blast TBI are not reported so far in academia, there is a widely recognized cadaveric human head impact test which provides bTBI researchers valuable data to evaluate their numerical head models (Nahum et al. 1977). The mechanical process involved in the impact on the structure is similar to that which exists in the blast loading on structure - both of them can be categorized as nonlinear transient dynamic processes, so once the FE head model is validated by this impact experimental data, some confidence can be assumed for the simulation of the blast-head interaction. Therefore, a FE impact analysis of the MRI based anatomically correct human head model is carried out by comparing the pressure

response of the FE head model and its counterpart in the experimental results under the same impact loading conditions as the experiment (Nahum et al. 1977).

2.1 HEAD GEOMETRIC MODELING AND FINITE ELEMENT DISCRETIZATION

The three-dimensional geometric model of a human head was developed from a set of two-dimensional MRI images of an actual human head. Reconstructing a three dimensional geometric model of human head from MRI data has become the widely recognized method to capture the detailed anatomical features of the complex geometry of the human head for the computational studies of bTBI (Chafi et al. 2009, Moore et al. 2009, Taylor and Ford 2009, Grujicic et al. 2010, Ganpule et al. 2012). Some of them include more cerebral parts (Chafi et al. 2009, Moore et al. 2009, Grujicic et al. 2010), than others (Taylor and Ford 2009, Ganpule et al. 2012). The FE head model built by Chafi et al. (2009) from CT data included scalp, skull, CSF, and brain meshed by solid elements, as well as dura, falx, tentorium, and pia meshed by shell elements. The FE head model built by Moore et al. (2009) segmented eleven distinct anatomical structures including skin/fat, skull, ventricle, glia, white matter, gray matter, eyes, venous sinus, CSF, air sinus, and muscle from MRI. Grujicic et al. (2010) purchased a CAD head model of six distinct sections including brain, CSF, small brain, brainstem, pituitary gland, and skull. Taylor and Ford (2009) constructed a FE head model based on the segmentation of MRI to represent skull, white matter, gray matter, and CSF. The FE head model constructed by Ganpule et al. (2012) included skin, skull, brain, and subarachnoid space.

The MRI data for this study were obtained from the International Consortium for Brain Mapping database (ICBM 2011). The head modeling was based on the same MR images used in

the previous studies (Wang et al. 2011, Wang et al. 2012), while it was improved by segmenting more structural details for this study. The MRI data of a female head consisted of 176 T1-weighted slices of 256^2 pixels taken at 1 mm intervals. In order to form the anatomically correct three-dimensional solid model of a human head, each image slice of the MRI data was segmented into five different anatomical components: (1) scalp, (2) skull, (3) cerebrospinal fluid (CSF), (4) nasal cavity, and (5) brain. BrainSuite software was employed for the first stage of the segmentation (BrainSuite 2011), i.e. to initially segment the MRI data into four different anatomical masks including scalp, skull, CSF, and brain. A mask was referred to the surface or contour representation of an anatomical component. The advantage of using the BrainSuite software was that its automatic segmentation tool can automatically segment a human head MRI into scalp, skull, CSF, brain. The automatic segmentation was not only very efficient compared to the manual user segmentation, it was also accurate in segmenting the geometrical detail of the brain gyri. However, the accuracy of the anatomical masks obtained in this stage was not perfect. For example, the nasal cavity was geometrically segmented together with the CSF in the automatic segmentation. Therefore, the second stage of the segmentation task was to correct the inaccurate geometric representations produced in the first stage.

During the second stage, the masks created in BrainSuite were output as IMG files which were imported into the MIMICS[®] 13.0 software (Materialise 2011) for further editing. MIMICS[®] software is a powerful medical image (for CT, MRI, microCT, CBCT, Ultrasound, Confocal Microscopy) processing tool capable of segmentation, three-dimensional modeling, and FEA meshing. In MIMICS[®], the mask of the nasal cavity was segmented from the CSF as an independent anatomical component; the skull layer between the nasal cavity and the CSF was also segmented; the inaccurate geometrical representation at the vertebrae was corrected. During

the third stage, the five masks were used to create the three-dimensional non-manifold assembly which assembled a three-dimensional representation of the human head geometric model in MIMICS[®]. Finally, the three-dimensional model of the human head was output in the form of a Stereolithography file (STL), which can be input into a finite element meshing tool. Due to the resolution of the MRI data, some essential simplifications were adopted in the geometric modeling. The skin, muscle, fat, and any other tissues covering the skull model were modeled together as the whole scalp model. The dura mater, a semi-rigid layer firmly attached to the skull, was modeled together with the skull because it was too thin to be distinguished from the skull. CSF, a natural fluid shock-absorber protecting brain, separates the brain from the skull and enables the relative motion between skull and brain. In this study, the whole CSF model integrated all the cerebrospinal fluid, sinuses, ventricles, and any other tissues in the space between the skull model and the brain model. The cerebrum, cerebellum, brainstem, and spinal cord were modeled together as the whole brain model.

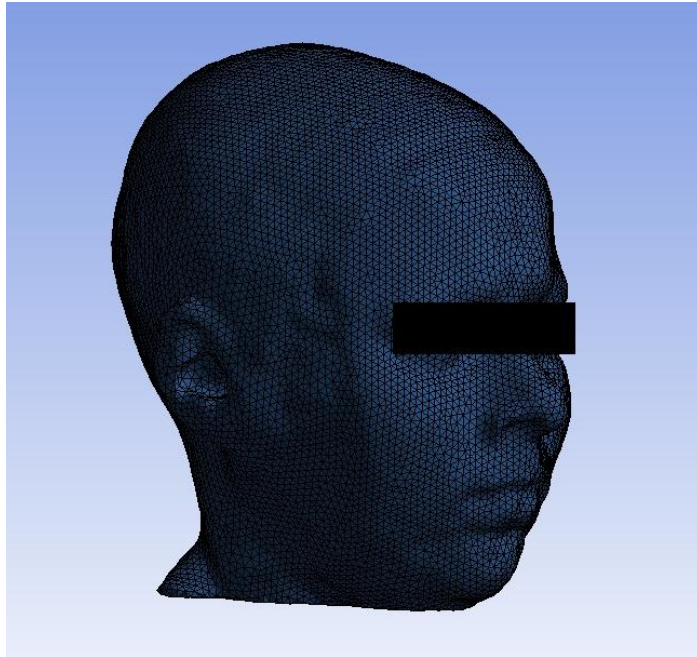
In the present study, the three-dimensional geometric model of human head in STL format was imported and meshed by the mesh generation software ANSYS ICEM CFD[®], which allowed users to produce high-quality volume meshes or surface meshes. Due to some of the very complex geometrical areas of the brain model and the CSF model, such as the gyri, a pure hexahedral mesh could not be achieved in the present study. The three-dimensional geometric model of human head was automatically meshed into a mixture of linear hexahedral elements, pentahedral elements, and tetrahedral elements. For each component, a core region of large volume was filled by hexahedral elements, which have a more robust performance than pentahedral elements and tetrahedral elements. The pentahedral elements and tetrahedral elements have a better geometric adaptability than hexahedral elements, and thus were used to

mesh the very complex regions which could not be meshed by hexahedral elements. The whole scalp model contained 280,175 elements (Figure 2-1). The eyes were covered for the sake of anonymity. The whole skull model contained 154,658 elements (Figure 2-2). The CSF was meshed into 54,878 elements. The nasal cavity, completely enveloped by skull, was meshed into 12,024 elements. The three dimensional FE models of the CSF and nasal cavity are shown in Figure 2-3. The models of the cerebrum, cerebellum, brainstem and spinal cord were also modeled together to constitute the whole brain model consisting of 105,575 elements (Figure 2-4). The whole FE human head model consisted of 607,310 elements. The element types and the respective element numbers for each anatomical component can be found in Table 2-1.

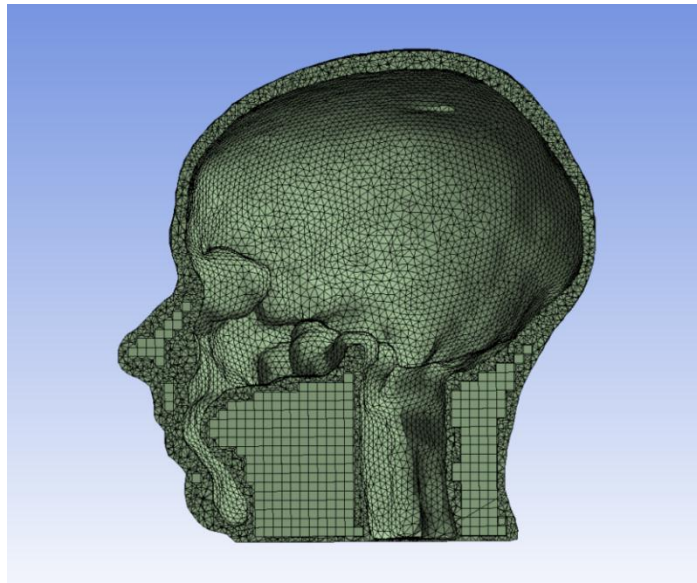
The final FE head model was imported into the explicit nonlinear FE software ANSYS AUTODYN[®] for the assignment of material models, and subsequent blast-head interaction simulations.

Table 2-1. Number of every element type in each of the anatomical components of the FE human head model

<i>Element Type</i>	<i>Number of finite elements</i>				
	Scalp	Skull	CSF	Nasal Cavity	Brain
Hexahedron	6782	164	21	179	12758
Pentahedron	7340	518	84	316	4652
Tetrahedron	266053	153976	54773	11529	88165

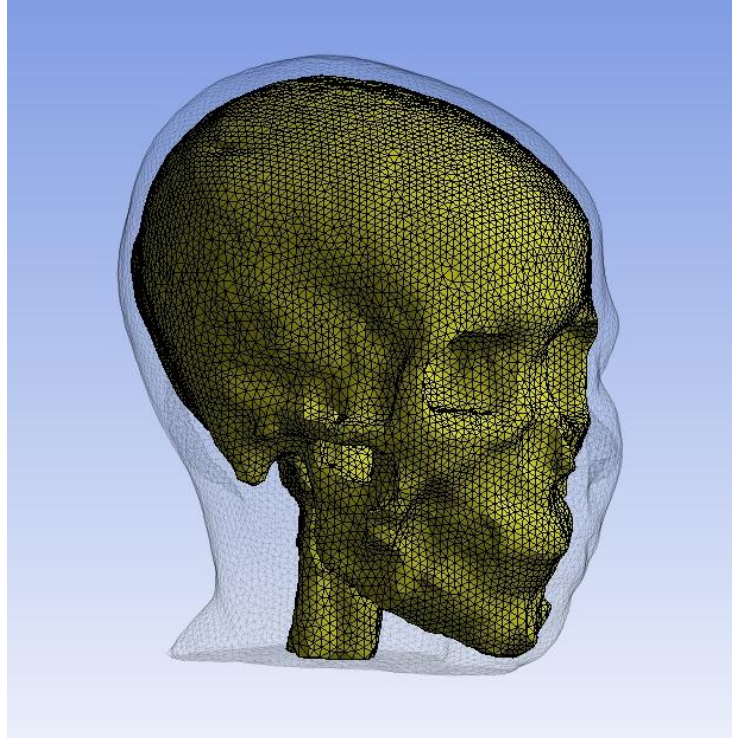


(a)

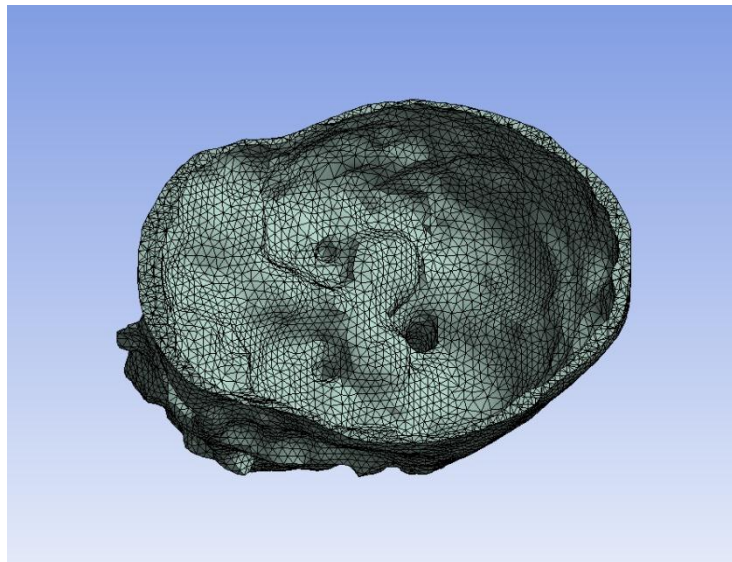


(b)

Figure 2-1. The three-dimensional finite element model of scalp: (a) Overall view, (b) Sagittal cross-sectional view showing the internal details



(a)



(b)

Figure 2-2. The three-dimensional finite element model of skull: (a) Overall view, (b) Transverse cross-sectional view showing the internal details

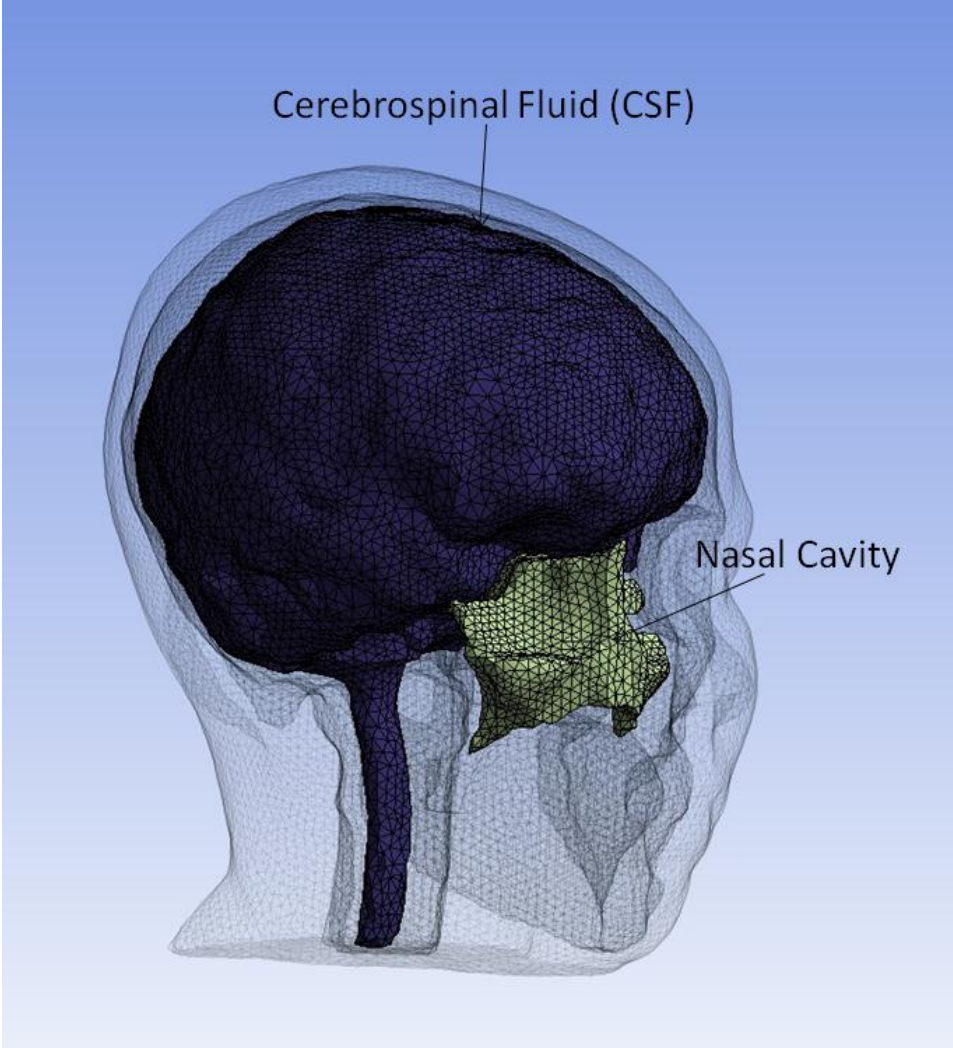
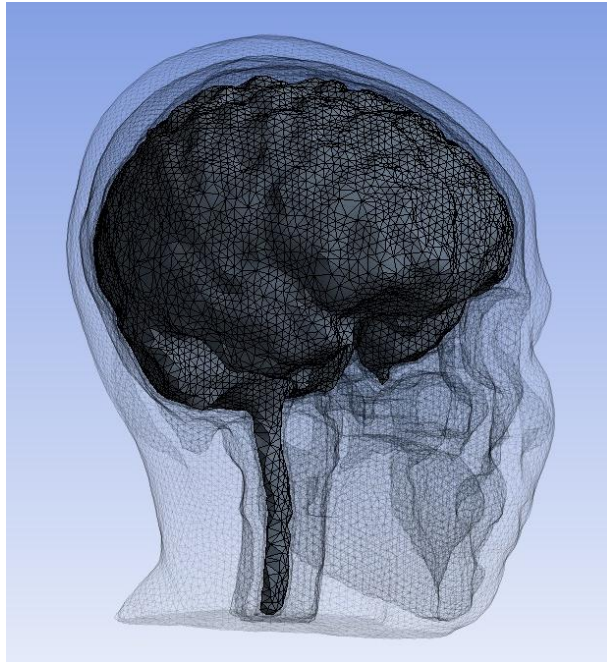
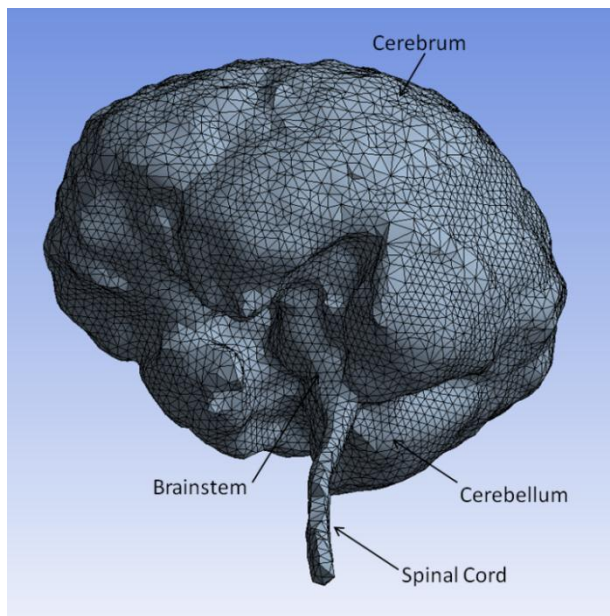


Figure 2-3. Three-dimensional finite element models of CSF and nasal cavity



(a)



(b)

Figure 2-4. Three-dimensional finite element model of brain: (a) Overall view of brain model, (b) Bottom view showing the cerebrum, cerebellum, brainstem, and spinal cord

2.2 MATERIAL MODELING OF HEAD

The constitutive models and their associative material parameters of the five anatomical constituents of the head model were adopted from the literature. The constitutive relation of scalp and nasal cavity was linear elastic and was described by the bulk modulus and shear modulus, representing dilatational/volumetric and deviatoric/shear responses respectively. The dilatational behavior described only by bulk modulus has the form of a linear equation of state in AUTODYN[®]:

$$P = K\mu \quad (2.1)$$

where P is the hydrostatic pressure, K is bulk modulus, and μ is the compression. The material constants of the scalp and the nasal cavity were chosen from the bTBI study of Moore et al. (2009). Bulk modulus K , density ρ , and shear modulus G of the scalp were 34.7 MPa, 1.04 g/cm³, and 5.88 MPa respectively. The bulk modulus K and shear modulus G of the scalp in this study were also identical to the corresponding values calculated by $K = E/3(1-2\nu)$ and $G = E/2(1+\nu)$ using the Young's modulus E and Poisson's ratio ν of scalp/skin in other literatures (Zhang et al. 2001, Chafi et al. 2009, Ganpule et al. 2012). Most of the computational studies of bTBI did not include the model of nasal cavity (Chafi et al. 2009, Moss et al. 2009, Taylor and Ford 2009, Panzer et al. 2012), while some of the literature just modeled the nasal cavity together with skull (Grujicic et al. 2010), or with the subarachnoid space (Ganpule et al. 2012). It was found that only Moore et al. (2009) included the air sinus in their FE head model, so bulk modulus, density, and shear modulus of the nasal cavity in the present study were 2.19 GPa, 1.04 g/cm³, and 225.3 Pa, respectively, picked from the study by Moore et al. (2009).

Skull is composed of bone material, and it has the highest rigidity among all the anatomical parts of the head. In order to capture the large volumetric compressions of the skull that may arise in the severe blast events with high overpressures, the dilatational part of the skull constitutive model was represented by the Mie-Gruneisen equation of state (EOS), which is also known as the "shock-Hugoniot" EOS, and is expressed by:

$$P = \frac{\rho_0 C_0^2 \left(1 - \frac{\rho_0}{\rho}\right)}{\left[1 - s \left(1 - \frac{\rho_0}{\rho}\right)\right]^2} \quad (2.2)$$

$$U_s = C_0 + s \cdot U_p \quad (2.3)$$

In equation (2.2), P is pressure, ρ is the density; in equation (2.3), U_s is the shock velocity, U_p is the particle velocity. The reference density ρ_0 , sound speed C_0 and s are the material parameters. For the modeling of skull, the reference density was $\rho_0 = 1.412 \text{ g/cm}^3$, the parameter C_0 was 1,850 m/s, and the dimensionless parameter s was 0.94. Similar to the scalp and the nasal cavity, the deviatoric response of the skull was only described by a single material parameter, the shear modulus G , calculated as 2.664 GPa by the corresponding Young's modulus E and Poisson's ratio ν from literature. Since Grujicic et al. (2010) picked the material parameters of skull from the study of Moore et al. (2009), all the material parameters of the skull for the present study can be viewed as identical to those in the study of Moore et al. (2009). Hence, the complete mechanical properties of the skull model were characterized by the combination of the Mie-Gruneisen equation of state (EOS) and shear modulus, describing the dilatational and deviatoric responses respectively.

CSF is known as a Newtonian fluid that fills the subarachnoid space and ventricular system. The mechanical properties of CSF were recognized to be very close to that of water since the density and viscosity of CSF are very similar to that of water (Zhang et al. 2001). Some

of the simulation studies of bTBI used a linear elastic model for the dilatational part of the constitutive model of CSF (Chafi et al. 2009, Taylor and Ford 2009, Ganpule et al. 2012), they used the value 0.5 or 0.49 for the Poisson's ratio of CSF to describe the CSF as an incompressible solid. Moore et al. (2009) used the Tait EOS for the modeling of CSF. However, The Tait EOS was not supported by AUTODYN[®] 14.0. Panzer et al. (2012) used the Mie-Gruneisen EOS for the CSF and assigned it to have the material constants of water. In the present study, the volumetric/hydrostatic properties of the CSF model were characterized by equation (2.2) and equation (2.3) (Mie-Gruneisen/Hugoniot equation of state). The material parameters C_0 (1,647 m/s), ρ_0 (0.998 g/cm³), s (1.921) for the CSF model were chosen to have the corresponding properties of water from the published engineering standards (Cooper 1996). Since tetrahedral elements and pentahedral elements in the finite element CSF model were only supported by Lagrangian formulations in AUTODYN[®] 14.0, a very low shear modulus of 500 Pa was assigned to the CSF model to accommodate the hydrostatic property, following what Zhang et al. (2001) did for the material modeling of the CSF shear property.

The cerebrum, cerebellum, brainstem, and spinal cord mainly consist of white and gray matter. The material properties of white and gray matters are different, but both exhibit complex mechanical properties including structural anisotropy and viscoelasticity. White matter is mainly composed of axonal fibers with various directions, therefore exhibiting regional difference of mechanical behavior. Gray matter is mainly composed of cell bodies of neurons, and can be viewed as isotropic. Much research efforts have been put by academia into developing state of art constitutive models of brain matter in order to better numerically model the mechanical behavior of brain (Miller 1999, Ning et al. 2006, Shen et al. 2006, Prevost et al. 2011). In the present study, a linear elastic model for dilatational response and a linear viscoelastic constitutive

law for deviatoric response were adopted for the whole brain model. The constitutive relations and the associated material constants of brain were derived by Zhang et al. (2001) based on *in vitro* vibration tests of human brain tissue (Shuck and Advani 1972). In addition, Zhang et al. (2001) validated their finite element head model by simulating the same impact on their head model against the impact test conducted by Nahum et al. (1977) on a cadaver human head. The volumetric property of brain tissue was characterized by bulk modulus only. The deviatoric property of brain tissue was described by a generalized three-term Maxwell viscoelastic model which expresses the shear modulus by:

$$G(t) = G_{\infty} + (G_0 - G_{\infty})e^{-\beta t} \quad (2.4)$$

where G_0 is the short-term shear modulus, G_{∞} is the long-term shear modulus, β is the viscous decay constant, and t is time. The properties of white matter and gray matter reported by Zhang et al. (2001) were different. But in our study, we did not separate white matter and gray matter in the stage of geometrical modeling. Since white matter accounts for a higher portion of brain than gray matter, in the present study, the material parameters of the whole brain were assigned as those of the white matter reported by Zhang et al. (2001). So, G_0 was 41 KPa, G_{∞} was 7.8 KPa, and β was 700 s^{-1} for the shear properties of the brain model. The density ρ and bulk modulus K of the brain model were assigned by 1.04 g/cm^3 and 2.19 GPa respectively. The constitutive models and the associated material parameters used for the finite element head model in this study were summarized in Table 2-2.

Table 2-2. Constitutive models and associated material parameters of FE human head model for this study

<i>Part</i>	<i>Constitutive model</i>	<i>Material Parameters</i>
Scalp	Linear Elastic	$K = 34.7 \text{ MPa}, G = 5.88 \text{ MPa}, \rho = 1.04 \text{g/ cm}^3$
Nasal cavity	Linear Elastic	$K = 2.19 \text{ GPa}, G = 225.3 \text{ Pa}, \rho = 1.04 \text{g/ cm}^3$
Skull	Mie-Gruneisen EOS	$C_0 = 1,850 \text{ m/s}, s = 0.94, \rho_0 = 1.412 \text{ g/cm}^3$ $G = 2.664 \text{ GPa}$
CSF	Mie-Gruneisen EOS	$C_0 = 1,647 \text{ m/s}, s = 1.921, \rho_0 = 0.998 \text{ g/cm}^3$ $G = 500 \text{ Pa}$
Brain	Viscoelastic	$K = 2.19 \text{ GPa}, \rho = 1.04 \text{g/ cm}^3$ $G_0 = 41 \text{ KPa}, G_\infty = 7.8 \text{ KPa}, \beta = 700 \text{ s}^{-1}$

2.3 VALIDATION OF FINITE ELEMENT HEAD MODEL

The anatomically fidelic human FE head model generated from the MRI data set was validated using the experimental data of a published experiment of frontal impact on a cadaveric head (Nahum et al. 1977). A large number of researchers validated their finite element head models using this published data of the cadaveric test for their computational studies of impact TBI (Ruan and Prasad 1995, Willinger et al. 1999, Zhang et al. 2001, Horgan and Gilchrist 2003, Kleiven 2006, Elsayed et al. 2008, Chen and Ostoja-Starzewski 2010, Sporns et al. 2012). Ganpule et al. (2012) validated their FE head model using the published data of the cadaveric impact experiments previously mentioned (Nahum et al. 1977), indicating a good match between the result of the head impact simulation and that of the experiment although the head model of

Ganpule et al. (2012) only had four anatomical parts. This indicated that the number of the individual anatomical structures in the head model does not play a significant role in the numerical accuracy of head model as long as the major structures have been created.

This cadaveric experiment has been widely recognized by TBI researchers as a standard to validate their FE head models. In this experiment, the foreheads of seated stationary human cadavers were impacted by a rigid mass moving at a constant velocity along the anterior-posterior direction in the mid-sagittal plane. The heads were rotated forward in order to incline the Frankfort anatomical plane 45° to the horizontal plane. Several padding materials were placed in between the skull and rigid mass to adjust the duration of the loading forces. The input force on the skull was measured during the impact test. The intracranial pressure-time histories at several cerebral locations were recorded by transducers. Only the figures of the pressure-time history and the input force-time history of the experiment No. 37 were reported. Therefore we only referred to the No. 37 experiment in this report as the Nahum's experiment in the following content.

In order to simulate Nahum's experiment, the measured input force of this test was applied to the center area of the forehead of head model in the anterior-posterior direction with 45° inclined to the horizontal as a form of a distributed load, as shown in Figure 2-5.

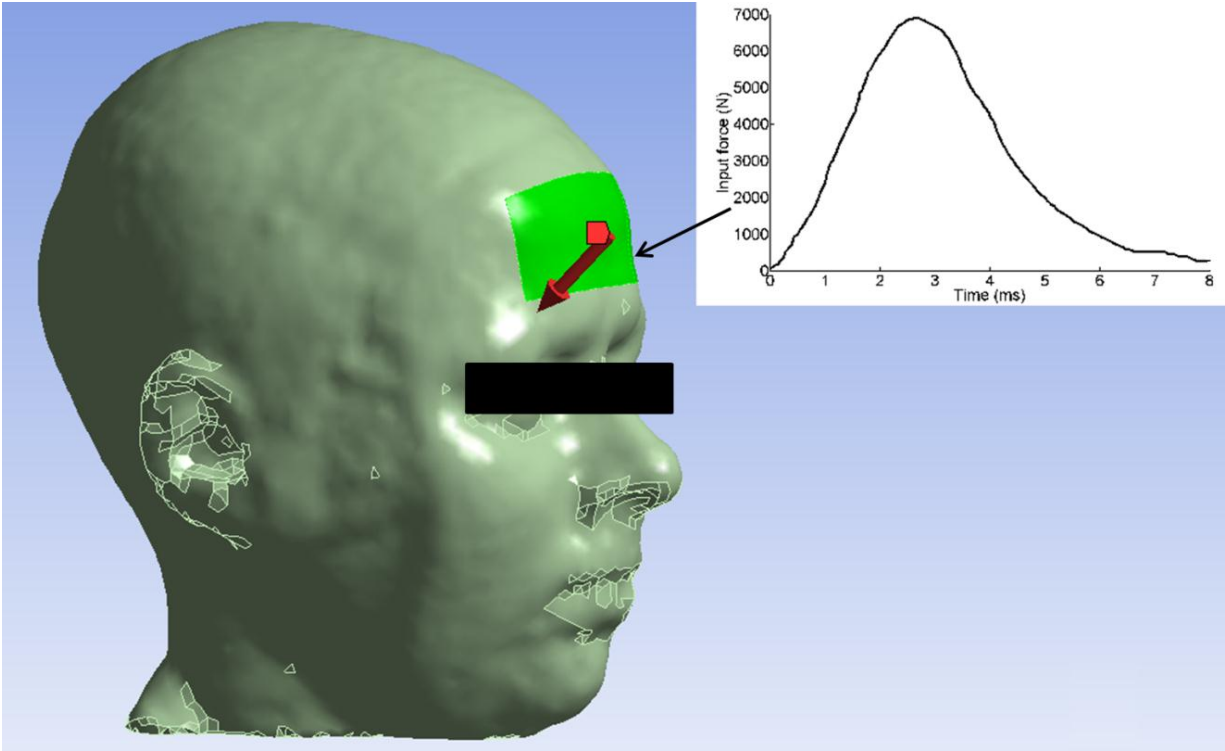
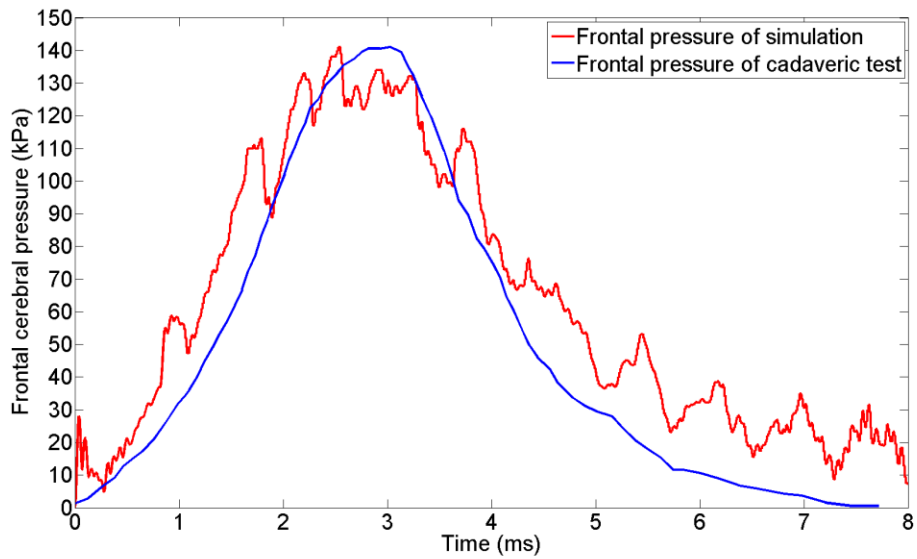
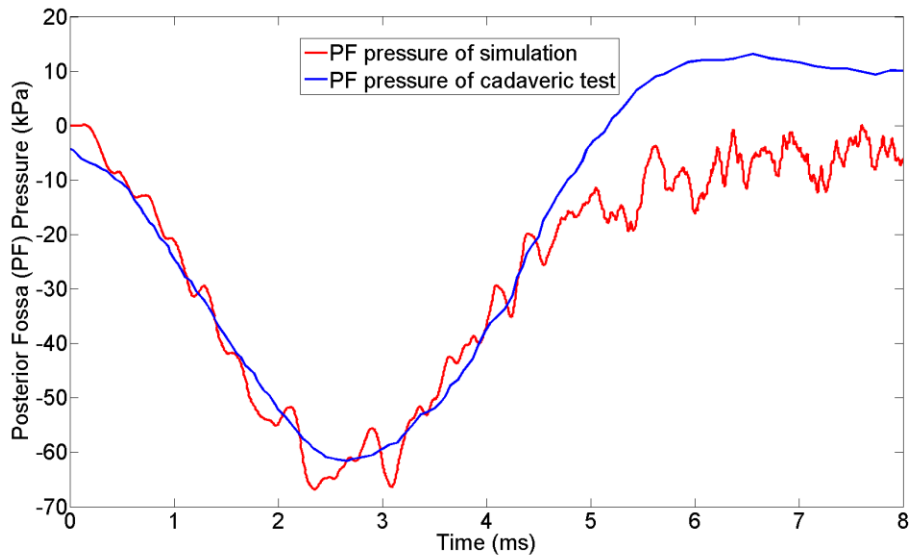


Figure 2-5. Validation of the FE head model by applying the measured input force of Nahum's experiment

The pressure-time histories were recorded at the same frontal cortex and the posterior fossa areas as in the Nahum's experiment during the simulation of the FE head model validation. The comparison between the simulated profile and the experimental profile for each of the two areas shows good agreement (Figure 2-6). The frontal peak pressure of the validation simulation was almost the same as that of the Nahum's experiment, while the peak negative pressure at posterior fossa of the simulation was 7.74 % less than that of the cadaveric experiment. So, the present FE head model was considered basically accurate to be used as the blast-head simulations. Since the FE head model was not validated against any cadaveric head experiments under blast loadings, it currently can only be claimed as partially validated. Once a valid blast-cadaveric head experiment is performed, it would be used to fully validate the current FE head model.



(a)



(b)

Figure 2-6. Comparison between the pressure-time histories of simulation and Nahum's cadaveric test at (a) Frontal cortex and (b) Posterior fossa

3.0 NUMERICAL IMPLEMENTATION OF SIMULATIONS OF BLAST-HEAD INTERACTIONS

This chapter examines the modeling and simulation methods of TNT air blasts using Euler formulations. The governing equations of shock wave generation and propagation, along with the material models of explosives and air are explained. Numerical techniques in AUTODYN[®] for solving the governing equations and the associated constitutive models of air blast are introduced. It also explained how the Euler-Lagrange coupling algorithm was applied to solve the fluid-structure interaction (FSI) problem involved in the blast-head simulations.

3.1 MATERIAL MODELS OF EXPLOSIVES AND AIR

The material model used for the detonation modeling in the present study was the so called Jones-Wilkins-Lee (JWL) equation of state (Lee et al. 1968), which is suitable for hydrodynamic computations of a wide range of explosive expansions. The JWL EOS is able to model most types of high explosives with the form stated as

$$P = A \left(1 - \frac{\omega}{R_1 V}\right) e^{-R_1 V} + B \left(1 - \frac{\omega}{R_2 V}\right) e^{-R_2 V} + \frac{\omega E}{V} \quad (3.1)$$

where P is the pressure, V is the relative volume. A , B , R_1 , R_2 , and ω are all material constants determined from the experiments of the explosive materials, such as TNT and PETN.

The material parameters of TNT used in this study are listed in Table 3-1 based on literature (Lee et al. 1973).

Table 3-1. Material parameters of TNT explosive

<i>Density</i>	<i>Detonation</i>	<i>Energy/unit</i>	<i>C-J</i>	<i>A</i>	<i>B</i>	<i>R1</i>	<i>R2</i>	<i>ω</i>
(g/cm ³)	velocity (m/s)	volume (kJ/m ³)	pressure (GPa)	(GPa)	(GPa)			
1.63	6930	6.0e6	21	373.77	3.75	4.15	0.9	0.35

The constitutive property of air was represented by an equation of state for an ideal gas:

$$P = (\gamma - 1) \frac{\rho}{\rho_0} E \quad (3.2)$$

where P is the current absolute pressure in air, E is the initial internal volumetric energy density, and ρ is the current mass density. ρ_0 is the initial mass density of the ideal gas (0.001225g/cm³ for air). As the adiabatic exponent, γ has the value 1.4 for air. It can be shown that if the expansion ratios are very large, the first and second terms on the right side of the JWL equation tend to negligible and therefore making the behavior of explosive approaches that of an ideal gas. At large expansion ratios, where the explosive has expanded by a factor of approximately 10 from its original volume, ANSYS AUTODYN[®] 14.0 automatically switches from the JWL to the ideal gas law, and thus avoid potential numerical difficulties.

3.2 NUMERICAL FORMULATIONS

The numerical formulations adopted in this study are identical to those used in the previous studies (Wang et al. 2011, Wang et al. 2012). Explosives generate a very rapid release of energy in the order of microseconds when subjected to suitable stimuli. In the theory of blast mechanics, a detonation is assumed to be a shock wave which propagates through the unreacted explosive material instantaneously releasing energy and converting the explosive into blast products (AUTODYN 2003). The Rankine-Hugoniot relations, representing the conservation of mass, momentum and energy across the front of shock wave, are used to describe the shock wave generation and propagation in explosives across the reaction zone, and to describe the shock wave traveling in ordinary media. For detonation in explosives, the Rankine-Hugoniot relations for the unreacted explosive and the detonation products are expressed as:

$$D^2 = v_0^2 (p - p_0)/(v_0 - v) \quad (3.3)$$

$$u^2 = (p - p_0)(v_0 - v) \quad (3.4)$$

$$e - e_0 = Q + \frac{1}{2}(p + p_0)(v_0 - v) \quad (3.5)$$

In equations (3.3), (3.4), and (3.5), v_0 , p_0 , e_0 , Q are the specific volume, pressure, specific internal energy, and the specific chemical energy of the unreacted explosive, respectively. In the detonation products, u is the particle velocity, D is the detonation velocity, v , p , e are the specific volume, pressure, and specific internal energy, respectively. The equation (3.3) and equation (3.5) are known as the Rayleigh line, and the Hugoniot curve.

In order to relate the state variables before and behind the shock front in ordinary media such as in fluids and gases, the other form of Rankine-Hugoniot relations, expressing the conservation of mass, momentum, and energy across the discontinuity, were used (Hiermaier

2008). The effective variables of state beyond and behind the shock wave front are the pressures denoted by p_0, p_1 , the densities denoted by ρ_0, ρ_1 , the specific integral energies denoted by e_0, e_1 , and the particle velocities denoted by u_0, u_1 . The velocity of shock front propagation is denoted by u_s . The particle velocity in the medium ahead of the shock wave front is commonly assumed to be stagnant ($u_0 = 0$). Therefore, the equations of the conservation of mass, momentum, and energy are stated as:

$$\rho_0 u_s = \rho_1 (u_s - u_1) \quad (3.6)$$

$$\rho_0 u_s u_1 = p_1 - p_0 \quad (3.7)$$

$$p_1 u_1 = (e_1 - e_0) \rho_0 u_s + \frac{1}{2} \rho_0 u_s u_1^2 \quad (3.8)$$

ANSYS AUTODYN[®] has both 2D and 3D explicit numerical analysis solvers, known as "hydrocodes" where the equations of conservations of mass, momentum, and energy (governing equations) along with material models are simultaneously solved. AUTODYN[®] integrates finite difference, finite volume, finite elements, and meshless methods depending on solution needs, making it particular advantageous to use for modeling explosion, blast wave propagation, and the interactions between solids and blast waves. The governing equations of explosive detonation, blast wave generation and propagation in AUTODYN[®], are solved by Euler methods (Fairlie 1998, AUTODYN 2003). Various Euler solvers are applied for different needs of numerical computation. Based on finite volume methods, the multi-material Euler solver uses an immovable grid and tracks the states and flows of the materials throughout its grid, which therefore allows for multi-material flows and material strengths to be included in computation. The multi-material Euler processors in AUTODYN[®], also known as Godunov multi-material high-order Euler solvers, follow the techniques developed by van Leer (1977, 1979). Due to the high expansion and short time frame of the detonation of high explosives, a two dimensional

multi-material Euler solver is used to solve the dynamic gas and fluid problems involving multiple materials, such as the 2D detonation model constituted by TNT and air in the present study. The simulation of the 2D detonation model of TNT and air generated blast wave that transformed from the detonation energy of the TNT explosive, which was ignited in its center. This is the first step of the entire modeling process of the 3D blast-head simulations of the present study.

A fast single-material high-order Flux-corrected transport (FCT) 3D Euler processor was used for the numerical solution of the blast wave propagation through the 3D air space in the present study. The single-material FCT processor is more efficient at addressing the problems of shock wave propagations in fluids and gases, and it is based on the algorithm developed by Zalesak (1979). The states of the 1D blast wave originated from an initial simulation of 2D TNT detonation can be "remapped" into the 3D Euler-FCT coarser grid filled by fluid or gas material (with initial internal energy) to continue the numerical simulation of blast wave propagation through the 3D space (AUTODYN 2003). The "remap" technique for blast simulation provided by AUTODYN[®] was developed for two reasons: first, more accurate results of the detonations of high explosives can be obtained by the 2D multi-material Euler processor using a finer grid consisting of more cells; second, physical simulation time can be saved because 3D simulation of shock wave propagation consumes more computational resource than the 2D grid does. Therefore, a "remap" technique is very suitable for solving the shock wave propagation problems in a large space or say in the far-field. Once the end states of the 1D initial blast wave model are imported into the 3D Euler-FCT space, a spherical 3D blast wave model is formed and is symmetrical to the detonation center specified. Then, the 3D blast wave model is processed as a

high-pressure ideal gas region which can continue propagating, reflecting, or coupling with solids.

The powerful Euler-Lagrange coupling algorithm provided by AUTODYN[®] solves the FSI problems encountered in fluid-structure interaction, and in gas-structure interaction, such as the interaction between a blast wave and a solid structure. The Euler-Lagrange coupling transfers the loading from the propagating blast wave within the Euler-FCT grid to the impinging solid structures. Solid structures represented by the Lagrange formulation can "cut" through the fixed Euler mesh in an arbitrary manner. The Euler cells intersected by the Lagrange interface generate stress states forming the boundary conditions of the Lagrange interface. In turn, the Lagrange interface geometrically constrains the mass flow traveling within the Euler grid. The Euler solver employs a control volume to solve the equations governing the conservations of mass, momentum, and energy. As the Lagrange grid moves across the interacting Euler grid, the Euler control volumes can become very small, and even tends to zero when completely covered. To maintain the stability of the numerical solution, AUTODYN[®] combines small control volumes with their large neighbors as new larger control volumes. If a cell becomes sufficiently uncovered, it can be released as independent (AUTODYN 2003).

AUTODYN[®] can solve a number of time-varying dynamic problems including blast, impact, and contact by using the explicit finite element method. The direct time integration algorithms to solve the equation of motion are commonly classified as explicit or implicit. In explicit methods, the displacements at future time steps are computed using the information from previous time steps. The advantage of an explicit-time integration algorithm is that the solution can be computed without solving a system of equations, therefore this algorithm adapts to a variety of problem types. In comparison, in implicit-time integration method, the displacements

at future time steps depend not only on the past displacements, velocities, and accelerations, but also on the velocities and accelerations at the time step that is being solved. Therefore, the implicit algorithm will require the solution of a system of equations at each time step, resulting in a significant increase in computational demand as compared to explicit algorithm. To date, the implicit algorithm only applies to limited types of problems.

A drawback of the explicit method is that it is conditionally stable. If the time step is too big, a stable solution will not be reached. So, a smaller time step is usually indicated for a stable and accurate solution. AUTODYN[®] will adjust the time increment during simulation for stability and accuracy according to the complexity of the simulation at current time step. For the entire mathematical formulations of the explicit and implicit finite element methods, interested readers can refer to the books about finite element methods (Belytschko et al. 2000, Hughes 2000).

3.3 MODELING PROCEDURES OF BLAST-HEAD SIMULATION

Three simulation scenarios of human head exposure to blasts were performed. The first scenario simulated the human head exposures to the blasts from three horizontal orientations, i.e. anterior, right lateral, and posterior, such that the influence of blast orientations to the injury mechanism and the associated injury threshold could be analyzed. The second scenario involved the simulations of the human head exposures to the blast waves coming from the TNT explosions on the ground. The third scenario of blast-head simulations examined the mechanical responses of the human head model sustaining blast loadings in a small room. The first simulation scenario consisted of three blast-head simulation sets which corresponded to the three exposure orientations respectively. In addition, each simulation set had five blast-head simulations which

corresponded to five different intensities of the blast waves from the detonations of 250g, 300g, 350g, 400g, and 450g center-ignited TNT spherical charges at one meter distance from the head. The ground blast-head simulations and the small room blast-head simulations also used the 250g, 300g, 350g, 400g, and 450g TNT spherical charges.

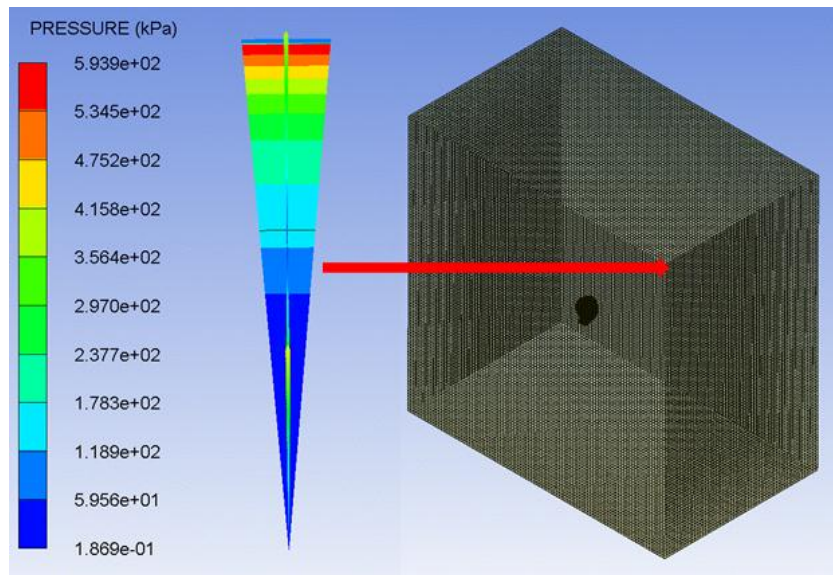
For each simulation scenario, the full computational model consisted of an idealized air space consisting of an Euler-FCT grid and the Lagrange FE head model. As shown in Figure 3-1, the air space was modeled as a 3 m by 1.8 m by 3 m volume meshed by the 30 mm length hexahedron Euler element. The material property of air was characterized by the ideal gas material constitutive model and was assigned the internal energy of a standard atmosphere. An Euler grid maintains its shape while the fluid moves within the grid domain, thus it was suitable for the numerical simulation of blast wave propagation. The head model was formulated with Lagrange elements, which deform with the materials contained. Solid material undergoes relatively smaller deformations than fluid media, so Lagrange elements could better simulate the mechanical responses of human head.

In order to save the computational expense of the blast wave generation and propagation, and to obtain a more accurate result, the provided "remapping" tool in AUTODYN[®] was used to simulate an initial 2D blast model for every blast scenario. In the 2D TNT air-blast model, the length of TNT was set to the radius of the 3D TNT spherical charge. The states of the 1D blast wave obtained from the initial 2D blast were transferred into the 3D air space to construct a complete 3D spherical blast wave (Figure 3-1b). Before the onset of the blast simulations, the internal energy of the air space was set to ambient conditions such that the atmospheric pressure could return to the standard atmosphere after the blast energy fully dissipated from the air space.

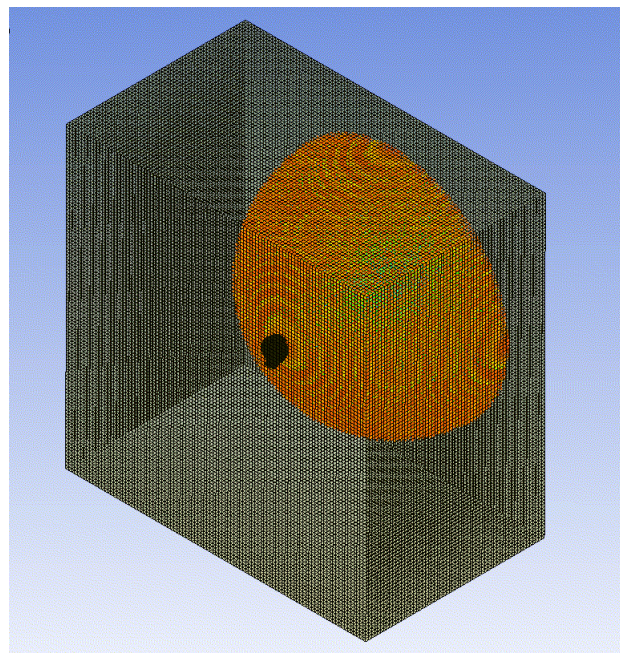
The complete FE head model was embedded into the 3D air space model for every blast-head simulation. The neck of the head model was assigned to have a free boundary condition since this boundary condition was a more realistic reflection of the mobility of the neck during the blast event. At every time step, the fully coupled Euler-Lagrange algorithm coordinated the two different numerical formulations of the blast wave and the FE head model, therefore enabling the blast wave to transmit through the FE head model. In order to monitor the mechanical responses of the head to blast waves, 23 gauge points, similar to real sensors, were placed inside the head (Figure 3-2). Particularly, in the SSS region, gauges No. 1, No. 2 and No. 3 were placed in the skull, CSF, and cortex respectively, in order to record the complete mechanical responses of the three distinct tissue layers surrounding the SSS. Gauges No. 4 to No. 16 were placed in the head at various locations along the anterior-posterior direction in the mid-sagittal plane, in order to track the evolution of the intracranial mechanical responses along the pathway of the blast waves. From gauge No. 6 to gauge No. 13, a distance of 20 mm between two gauges was specified. Gauge No. 24 was fixed near the head model in the air to track the pressure-time histories of the blast wave near the head, without any change of location as the blast specification switched. An additional air gauge was placed in the rear space of the head model for the room blast-head simulation scenario.

The simulation results were analyzed to identify the patterns of the pressure wave propagation in the head during the various blast scenarios, and to identify the locations and the strengths of the high-level volumetric and deviatoric stresses, and to understand how the stresses evolved during the whole process of blast-head interactions. The intracranial pressures and deviatoric stresses were used to estimate the injury severities or perhaps thresholds of the cerebral contusion and DAI, respectively. The mechanical responses of the SSS were used to

determine the loading conditions assigned on the independent bridging vein finite element analysis which would estimate the injury occurrence of the blast-induced subdural hemorrhage.

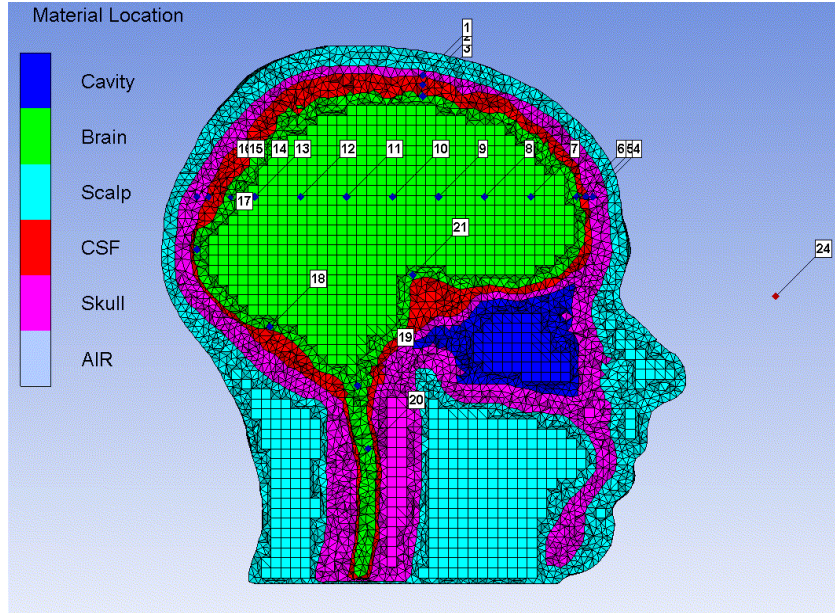


(a)

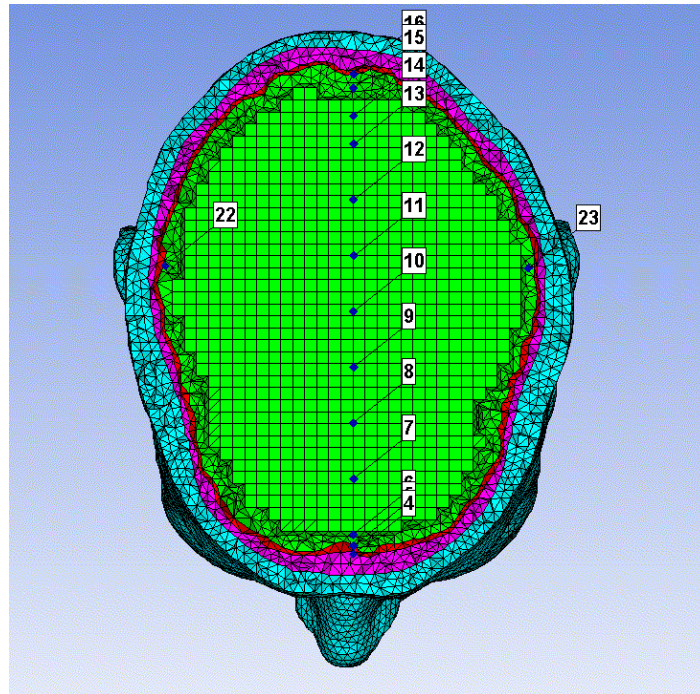


(b)

Figure 3-1. (a) 2D 450g TNT air-blast model was remapped into the Euler-FCT grid of the air space model in order to form (b) the complete 3D blast-head model of 450g TNT



(a)



(b)

Figure 3-2. Locations of gauges: (a) Sagittal cross-sectional view, (b) Transverse cross-sectional view

4.0 BLAST-HEAD INTERACTION SIMULATIONS OF HORIZONTAL EXPOSURE TO BLAST

This chapter presents the mechanical responses of the human head for the first blast-head simulation scenario, i.e., the simulations of FE human head subjected to the blast waves from the anterior, right lateral, and posterior directions. The charges of the TNT explosives were 250g, 300g, 350g, 400g, and 450g for each direction. The sensitivities of the human head responses to the blast overpressure (BOP) levels and orientations were investigated. The distribution patterns of the intracranial pressure and the von-Mises stress of the brain model were investigated to estimate the possible injured cerebral regions. The influences of the impinging BOPs at the blast incident side and the exposure orientations on the injury severities of cerebral contusion at various cerebral regions were assessed based on the corresponding levels of the intracranial pressures. The possibility of diffuse axonal injury (DAI) based on the levels of von-Mises stresses at the focal regions was also evaluated.

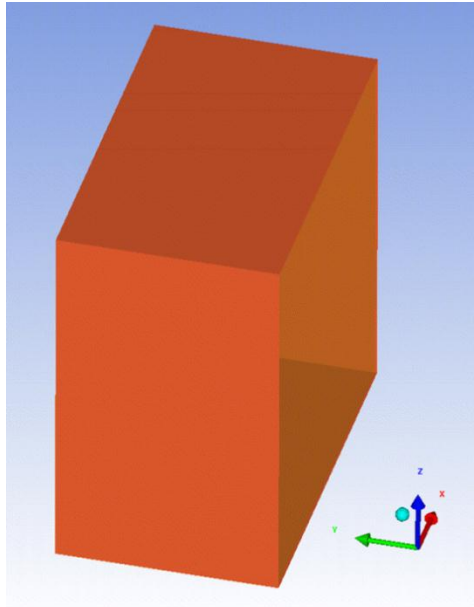
4.1 PREPROCESSING OF SIMULATIONS

The air space model was established as described in the section 3.3. An open boundary condition was assigned to the surfaces of the 3D air space except the surface where the detonation center was located such that the blast waves could propagate out of the space without reflection. The

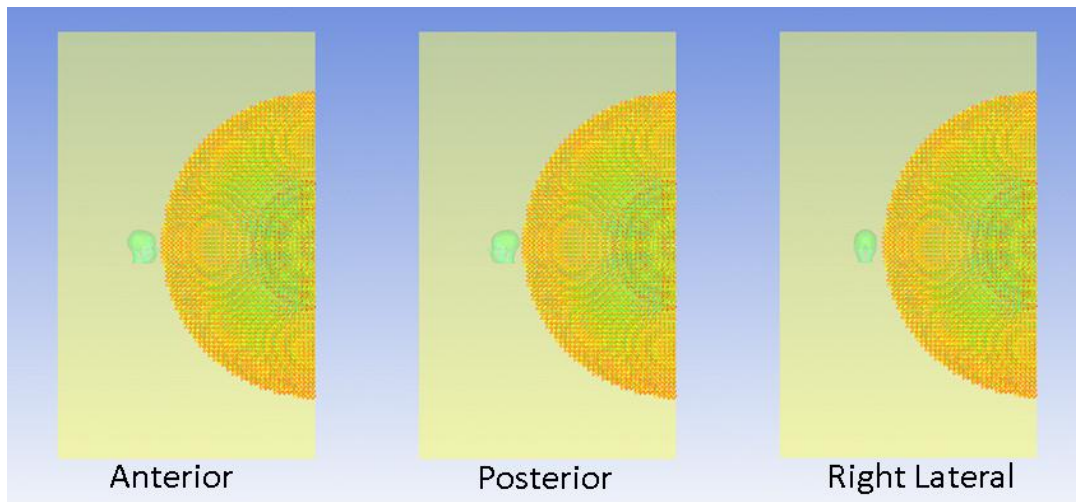
boundary condition settings of the air space along with the three pre-processed blast-head models for the three horizontal blast orientations are shown in Figure 4-1. The six surfaces of the 3D air space were named according to their locations and orientations in the Cartesian coordinate system of AUTODYN[®], in order to facilitate the following discussions. Among the three surfaces containing the zero point of the coordinate system, the surface perpendicular to the Y axis was named as the anterior surface; the surface perpendicular to the X axis was named as the right lateral surface; the surface perpendicular to the Z axis was named as the bottom surface. In contrast, among the three surfaces at the distal locations with respect to the zero point, the surface perpendicular to the Y axis was named as the posterior surface; the surface perpendicular to the X axis was named as the left lateral surface; the surface perpendicular to the Z axis was named as the top surface.

The three simulation sets corresponded to the three horizontal blast orientations which were anterior, right lateral, and posterior, according to the orientations from which the head was exposed to the blasts. In every simulation set, the FE head was subjected to the spherical air blast waves generated from the 250g, 300g, 350g, 400g, and 450g spherical TNT blasts. For every TNT explosive mass, a 2D TNT air-blast model was established to simulate the 1D blast wave propagating to a one meter distance. The states of the 1D blast waves were then transferred into the 3D air space to form the 3D spherical blast waves. The FE head model was placed one meter from the detonation center which was located at the center of the anterior surface of the air space. The durations of all the fifteen blast-head simulations were set to 5 ms, which was adequate for the typical Friedlander wave to fully exhibit and to dissipate completely from the air space. The simulations represented the ideal scenario where a people horizontally experienced the open-

field blasts with various explosive intensities from the three principal directions at the same horizontal level.



(a)

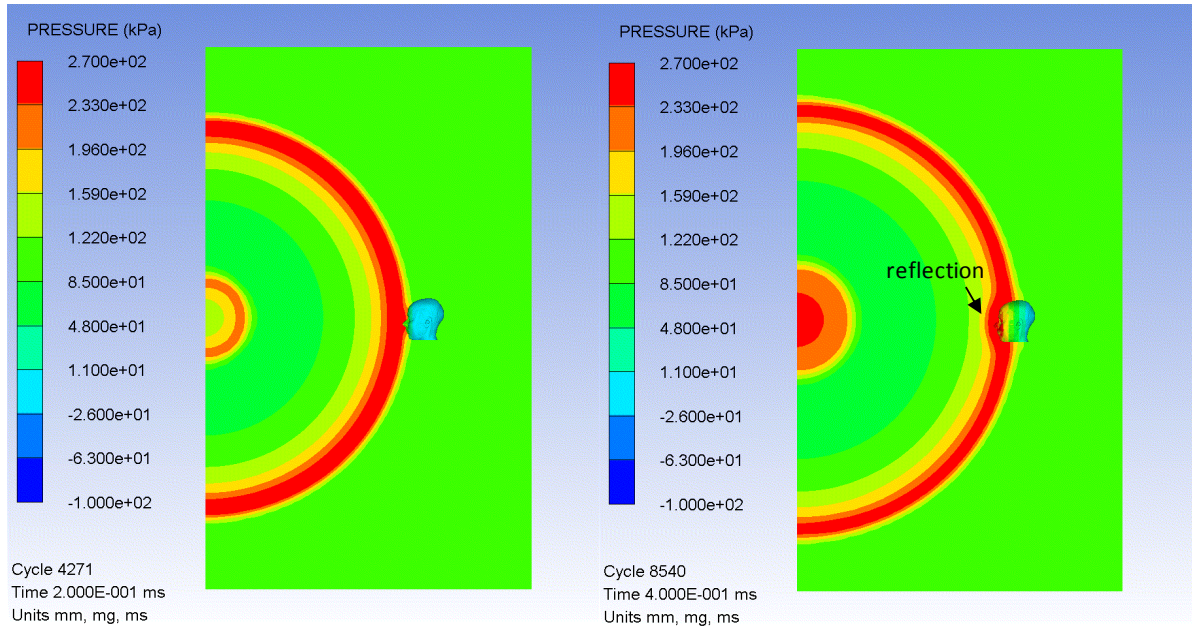


(b)

Figure 4-1. (a) The five surfaces of the air space were assigned with the open boundary condition indicated by orange color, (b) The FE head model was exposed to the blasts from the anterior, posterior, and right lateral horizontal orientations

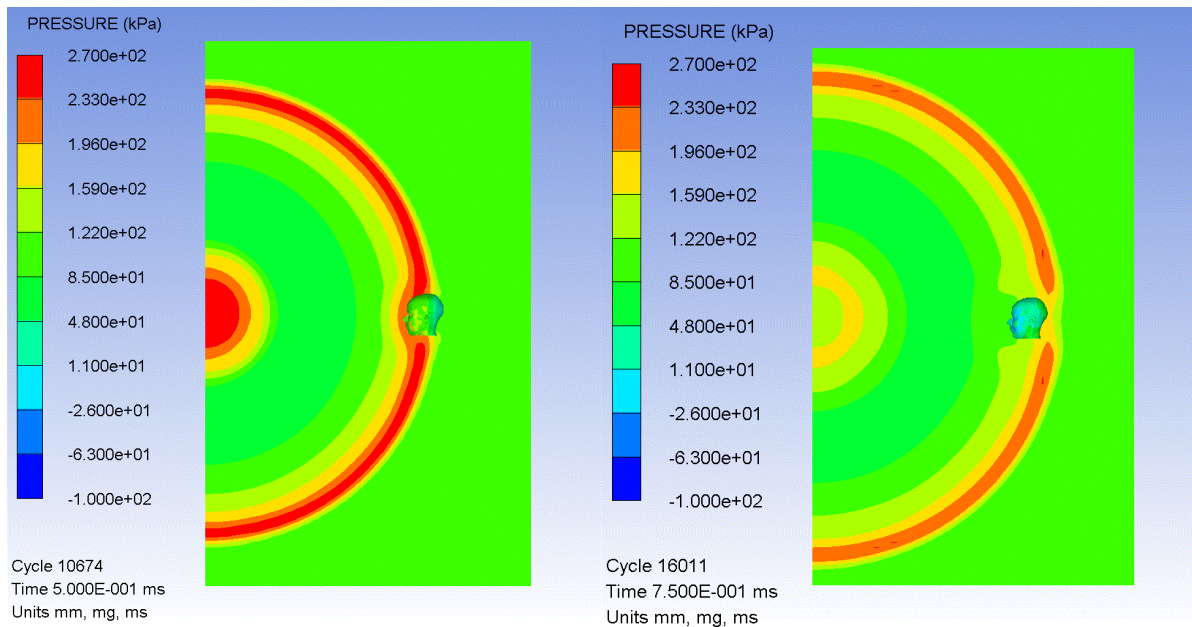
4.2 BRAIN PRESSURE RESPONSE TO HORIZONTAL BLAST

The time-lapse illustration of the 250g TNT anterior blast-head simulation in the mid-sagittal plane shows that the shock front of the 3D spherical blast wave expanded and propagated purely along the radial direction (Figure 4-2). The pressure time histories of blast overpressure (BOP) and the typical intracranial pressure time histories at several intracranial sites are shown in Figure 4-3. Behind the shock front, the dipping of the ambient pressure below standard atmospheric pressure, i.e. under-pressure, was observed. When the shock front propagated across the head, a slight wave reflection formed at the front of the head (Figure 4-2b). This reflection caused the small curvilinear inflection in the pressure time histories given in Figure 4-3a (the pressure produced by the gauge in front of the head in air) between approximately 0.3-0.5s. Judging from the very modest reflection and the discontinuity of high-level pressure behind the head (Figure 4-2d), it is believed that most of the energy of the blast wave impinging on the head was absorbed, resulting in the pressure waves propagating inside the head. The small reflected portion where the shock front reached the head and the discontinuity of high-level pressure behind the head were also observed in the blast-head simulations of the other two blast orientations.



(a)

(b)



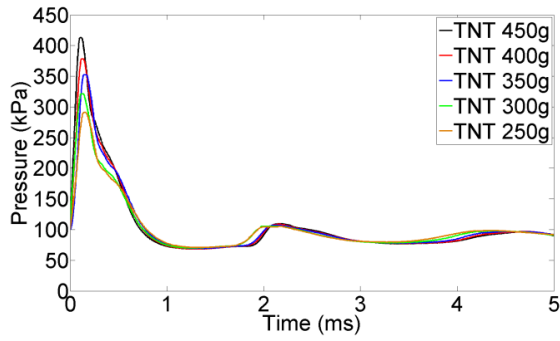
(c)

(d)

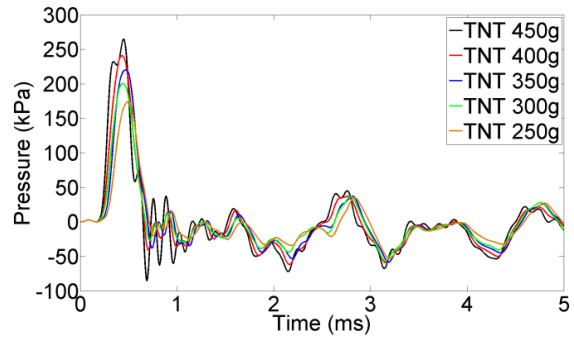
Figure 4-2. Blast wave propagating through the head during the first 0.5 ms of the 250g TNT blast-head simulation of the anterior blast scenario: (a) 0.2 ms, (b) 0.4 ms, (c) 0.5 ms, (d) 0.75 ms

The pressure waveforms of the blast waves in open-space air of the fifteen simulations were typical Friedlander waves (Friedlander 1976), which began with a sharply rising over-pressure followed by an under-pressure, finally returning to the normal ambient pressure after the subsidence of the blast energy (Figure 4-3a). The magnitudes of the BOPs recorded outside the head at the blast incident side were several times that of the standard atmospheric pressure. As the TNT weight increased, the peak BOP at the incident side grew as well (Figure 4-3a). The 250g, 300g, 350g, 400g, and 450g TNT charges had BOPs of 291 kPa, 321 kPa, 349 kPa, 379 kPa, and 413 kPa, respectively (Figure 4-3a). In every horizontal blast-head simulation, gauge No. 24 was kept at the same location in the air space, so the recorded peak BOP value corresponding to each blast level remained the same for every blast orientation. The total duration of the apparent BOP pulse lasted about 0.8 ms for every blast.

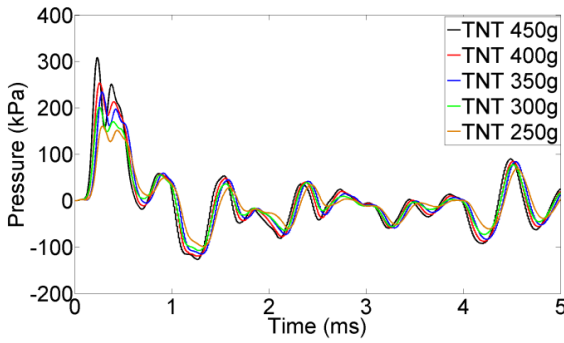
The pressure time histories of the various intracranial locations exhibited a pattern that was similar to that of the ambient pressure-time history: the intracranial pressures began with sharply rising and falling to form a pulse, which thereafter returned to zero pressure. Higher peak BOPs caused higher peak positive pressures in the brain for most intracranial locations, while the duration of the pressure pulse at the same cerebral location remained the same. The pressure pulse durations at the various intracranial sites were primarily related to the locations. The pressure pulse duration on the side of the head that was proximal to blast was smaller than that on the distal side to blast. The magnitude of the pressure wave attenuated during its propagation from the proximal to distal side of the head. For example, for the 300g TNT case for the anterior blast exposure, the peak positive pressure recorded by the gauge No. 6 at the frontal cortex was 201 kPa, while the gauge No. 14 at the occipital cortex had 138 kPa, so the corresponding percentage of attenuation in magnitude was calculated to be 31 %.



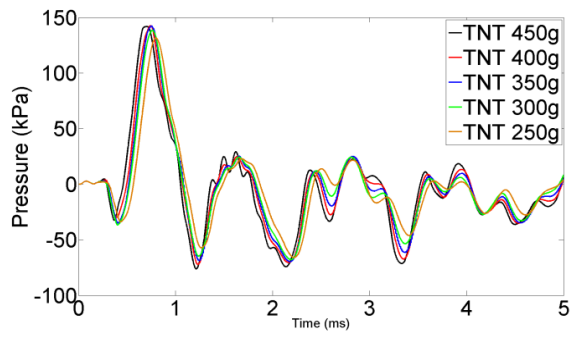
(a)



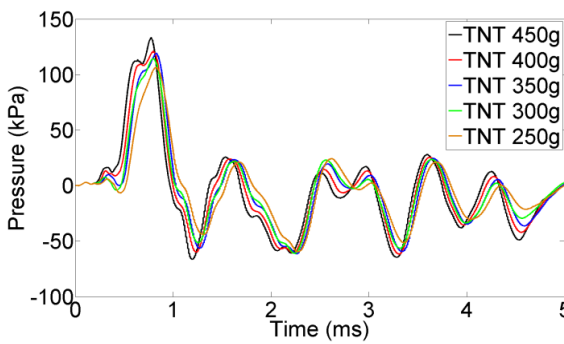
(b)



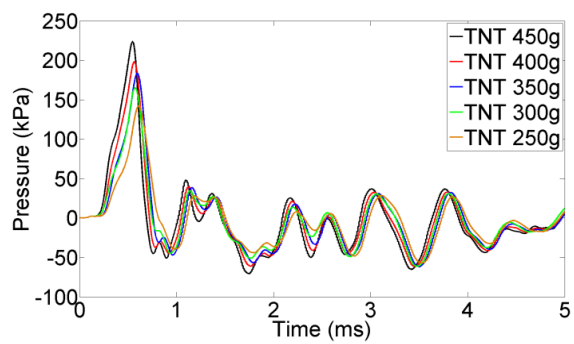
(c)



(d)



(e)



(f)

Figure 4-3. Pressure-time histories recorded by various gauge points for the anterior blast-head simulations: (a) No. 24 in atmosphere (b) No. 2 in the CSF at SSS, (c) No. 6 on the frontal cortex, (d) No. 14 in the occipital cortex, (e) No. 18 at the posterior margin of the tentorium cerebelli, (f) No. 19 on the lower brainstem

The highest value and the lowest value of the peak positive pressures existed on the proximal blast area and on the distal blast area of the brain, respectively, for all the simulations. Within the anterior blast exposure cases, the highest values of peak intracranial pressure occurred at the frontal cortex (gauge No. 6), ranging from 161 kPa to 308 kPa, while the lowest values occurred at the midsagittally posterior parietal area (gauge No. 12), ranging from 87 kPa to 94 kPa. Among the gauges from No. 6 to No. 14, the peak positive pressures for the gauges No. 6 to No. 12 exhibited an apparent gradient of the peak pressure attenuation, while gauges No. 12 to No. 14 exhibited a slight increasing gradient of peak pressure, as the areas of their corresponding coronal cross sections of the brain decreased. The peak pressures recorded by the gauge No. 14 for the anterior blast exposure ranged from 132 kPa to 142 kPa. The mitigation of the intracranial pressure indicated that the pressure wave traveling in the head has some blast energy absorbed by the viscoelastic brain tissue. The pressure wave attenuation was also obvious in the simulation sets of the right lateral blast exposures and the posterior blast exposures. Because the skull chamber was broader in the middle and was narrower in the front and back, the levels of the intracranial pressure waves were reinforced as they traveled from the broader cerebral cross-section to the narrower one, as long as the attenuation effects of the brain tissue was comparatively secondary to the concentration effect of the narrow region in the present simulations.

There was a timing delay between the arrival times of the peak positive pressures at the proximal blast location and at the distal blast location in the brain. For the anterior blast simulation set, the timing delay was 0.44 ms for gauge No. 6 and No. 14 (Figure 4-3c and Figure 4-3d); for the right lateral blast simulation set, the timing delay was 0.25 ms between gauges No. 22 and No. 23; for the posterior blast simulation set, the timing delay was also 0.44 ms between

gauge No. 14 and No. 6. The timing delay was interpreted as the time for the intracranial pressure wave to propagate from the proximal blast side to the distal side in the brain. The peak positive pressure in the CSF at SSS of gauge No. 2 did not show a notable difference among the three blast orientations while the anterior blast simulation set had a slightly higher level. Therefore, the peak pressures of gauge No.2 of the anterior blast simulation set were taken as the input loadings on the bridging vein finite element model to later estimate the injury occurrence of subdural hemorrhage instead of simulating bridging vein responses for all the three blast orientations.

In the cortex, the right lateral exposure orientation to the blasts had the highest levels of cortex pressures at the proximal side, i.e. right temporal cortex, with the range from 240 kPa to 421 kPa (gauge No. 22), as compared to 221 kPa to 402 kPa at the occipital cortex (gauge No. 14) of the posterior blast exposure simulation set, and to 161 kPa to 308 kPa at the frontal cortex (gauge No. 6) of the anterior blast exposure simulation set. The most injurious loading direction for cortex predicted for the horizontal blasts is very similar to the published bTBI simulation study of Taylor and Ford (2009), who revealed that the lateral blast was more injurious than the frontal and posterior blasts.

In the brainstem, the posterior exposure orientation to the blasts had the highest pressure levels, with the range from 247 kPa to 446 kPa, among the three orientations. In the posterior exposure cases, the pressure levels on the lower brainstem were even higher than that on the occipital cortex. The pressure waves propagating into the lower brainstem were reinforced by the concentration effect of the foramen magnum, which had a narrow region, even though the lower brainstem and the occipital cortex were both proximal to the blast waves. The lower brainstem in

the posterior blast exposures had the highest intracranial pressures among all the cerebral locations for the three blast exposure orientations.

Figure 4-4 shows the distribution of the intracranial pressure wave in the brain from 0.2 ms to 0.8 ms for all the blast orientations. For each of the blast orientations, the high pressure region of the brain first occurred at the proximal side to the blast wave source, then moved to the central cerebral region, and finally occurred at the side which was distal to the blast source. The pressure wave propagation within the cranium was associated with a decreasing gradient in pressure magnitude for each blast orientation. The highest pressure always occurred in the cerebral regions which were proximal to the blast wave source for each orientation, so the severity of parenchymal injury is expected to be a function of proximity to the blast wave source. A high-level positive and negative pressure existed at the lower brainstem and spinal cord for all the three blast orientations. The intense compressive and tensile pressures as well as their sharp transition in the posterior fossa and foramen magnum, especially for the inferior aspect of the cerebellum, pons, medulla and cervical spinal cord, could make the parenchyma and vasculature particularly vulnerable to injury.

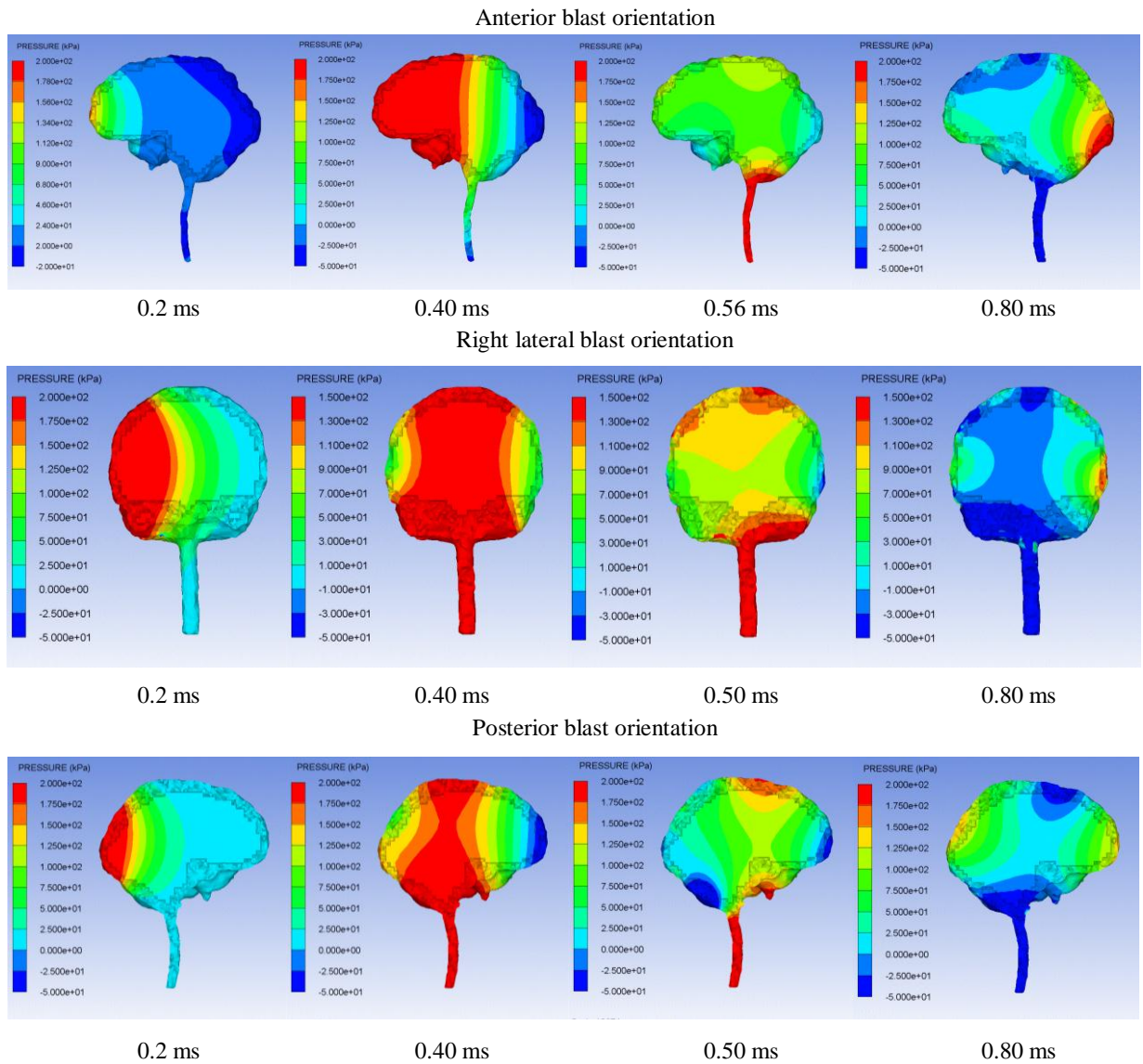


Figure 4-4. Pressure distributions of the brain in the 400g TNT blast-head simulations of all blast orientations

The pressure distribution patterns of the blast-induced TBI were distinct from that of the blunt impact induced TBI that exhibited a typical “coup and contrecoup” pressure phenomenon, in which the high level positive pressure prevailed at the impact side while high level negative pressure with similar magnitude prevailed at the opposite impact site of the brain simultaneously. The high negative pressure at the contrecoup side developed as the skull pulls the brain along due to the relative skull-brain motion resulted from the blunt impact on the cranium. In the simulation study of impact TBI published by Zhang et al. (2004), the predicted peak pressures at the coup and contrecoup sites ranged from 43 kPa to 130 kPa in compression at coup side, and from 32 kPa to 128 kPa in tension at contrecoup side. The pressure range at the coup cerebral region and that at the countercoup cerebral region were revealed to have nearly equal values. In contrast, in the present study, the anterior blast scenario possessed significantly higher peak positive pressures that ranged from 160 kPa to 308 kPa on the proximal side of the head, and the corresponding peak negative pressures were comparably lower in magnitude, ranging from -99 kPa to -127 kPa (Figure 4-3c); at the distal side from the blast (occipital cortex), the peak positive pressures still existed with a range from 132 kPa to 142 kPa which were still higher in magnitudes than the corresponding peak negative pressures ranging from -66 kPa to -76 kPa. The principal that the positive pressure was several times the magnitude of the negative pressure in the cranium applied to every blast orientation. Hence, it is concluded that the “coup-countercoup” intracranial pressure mechanism does not apply to the bTBI. Instead, the propagation of the intracranial pressure waves induced by the direct blast wave transmission into the head is the pressure distribution pattern of the bTBI.

In a published study by Ward et al. (1980), an intracranial pressure injury index was proposed to evaluate the occurrence and the injury severity of cerebral contusion. According to

this intracranial pressure tolerance criterion/index, the peak intracranial pressure of more than 235 kPa would induce serious cerebral contusion, while minor or no brain injuries would occur when the intracranial pressure was below 173 kPa. In between 173 kPa and 235 kPa, minor contusion or cortex hemorrhage would occur. Predicted intracranial pressure responses at the proximal side (frontal cortex) for all the blast simulation cases of the anterior blast exposure, except the 250g TNT case, were higher than 173 kPa, and the 400g TNT case had 252 kPa peak pressure which was more than the 235 kPa serious injury threshold. Therefore, people experiencing the anterior blast waves with the impinging BOP at the blast incident side from 321 kPa to 349 kPa would have a risk of suffering a minor contusion or cerebral cortex hemorrhage, and people experiencing the anterior blast wave with the impinging BOP at the blast incident side more than 379 kPa would be expected to have serious cerebral contusion. All the blast-head simulations of the right lateral blast exposures had peak positive pressures of more than 235 kPa at the cortex region proximal to the blast (right temporal cortex), indicating that people experiencing the lateral blast wave with the impinging BOP of more than 291 kPa at the blast incident side would have serious cerebral contusion. In the posterior blast cases, the peak positive pressures at the proximal side (lower brainstem) were all more than 235 kPa. Therefore, people experiencing the posterior blast wave with the impinging BOP of more than 291 kPa would have serious cerebral contusion.

The injury severities of the various cerebral locations including the cortex at the SSS, frontal cortex, occipital cortex, temporal cortexes, hypothalamus, and lower brainstem with respect to the five impinging BOPs at the blast incident side for the three blast exposure orientations are summarized in Table 4-1 (anterior exposure), Table 4-2 (right lateral exposure), and Table 4-3 (posterior exposure). For a better illustration, predicted contusion injury locations

and the associated severities for the three exposure orientations were pointed out on the mid-sagittal view of the brain in the Figure 4-5 (anterior exposure), Figure 4-6 (right lateral exposure), and Figure 4-7 (posterior exposure).

Table 4-1. Predicted contusion injury severities at typical cerebral sites with respect to impinging BOPs at the blast incident side in the anterior blast-head simulations

<i>Peak BOP (TNT weight)</i>	<i>Cortex at SSS</i>	<i>Frontal cortex</i>	<i>Occipital cortex</i>	<i>Temporal cortexes</i>	<i>Hypothalamus</i>	<i>Lower Brainstem</i>
291 kPa (250g)	None	None	None	None	None	None
321 kPa (300g)	Minor	Minor	None	None	None	None
349 kPa (350g)	Minor	Minor	None	None	Minor	Minor
379 kPa (400g)	Serious	Serious	None	Minor	Minor	Minor
413 kPa (450g)	Serious	Serious	None	Minor	Serious	Minor

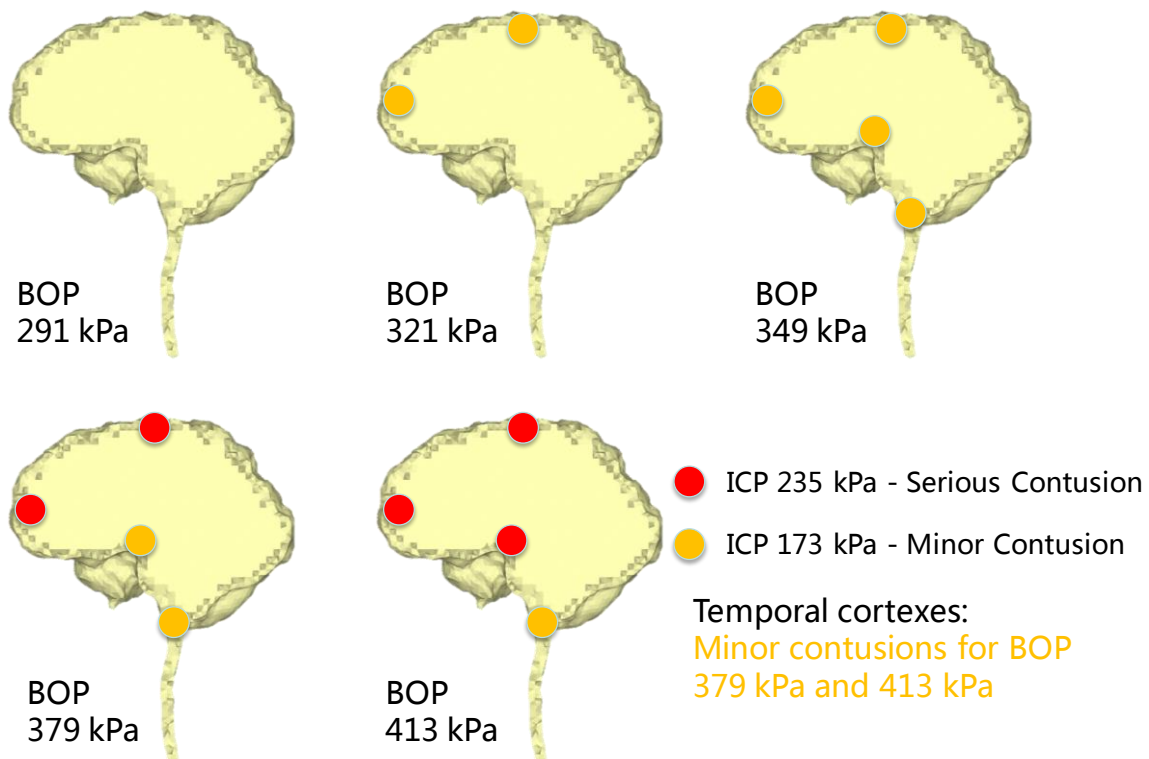


Figure 4-5. Predicted contusion injury location and severity of the anterior blast-head simulations

Table 4-2. Predicted contusion injury severities at typical cerebral sites with respect to impinging BOPs at the blast incident side in the right lateral blast-head simulations

<i>Peak BOP (TNT weight)</i>	<i>Cortex at SSS</i>	<i>Frontal cortex</i>	<i>Occipital cortex</i>	<i>Temporal cortexes</i>	<i>Hypothalamus</i>	<i>Lower Brainstem</i>
291 kPa (250g)	None	Minor	None	Serious	None	Minor
321 kPa (300g)	None	Minor	Minor	Serious	None	Serious
349 kPa (350g)	Minor	Serious	Minor	Serious	Minor	Serious
379 kPa (400g)	Minor	Serious	Minor	Serious	Minor	Serious
413 kPa (450g)	Minor	Serious	Serious	Serious	Minor	Serious

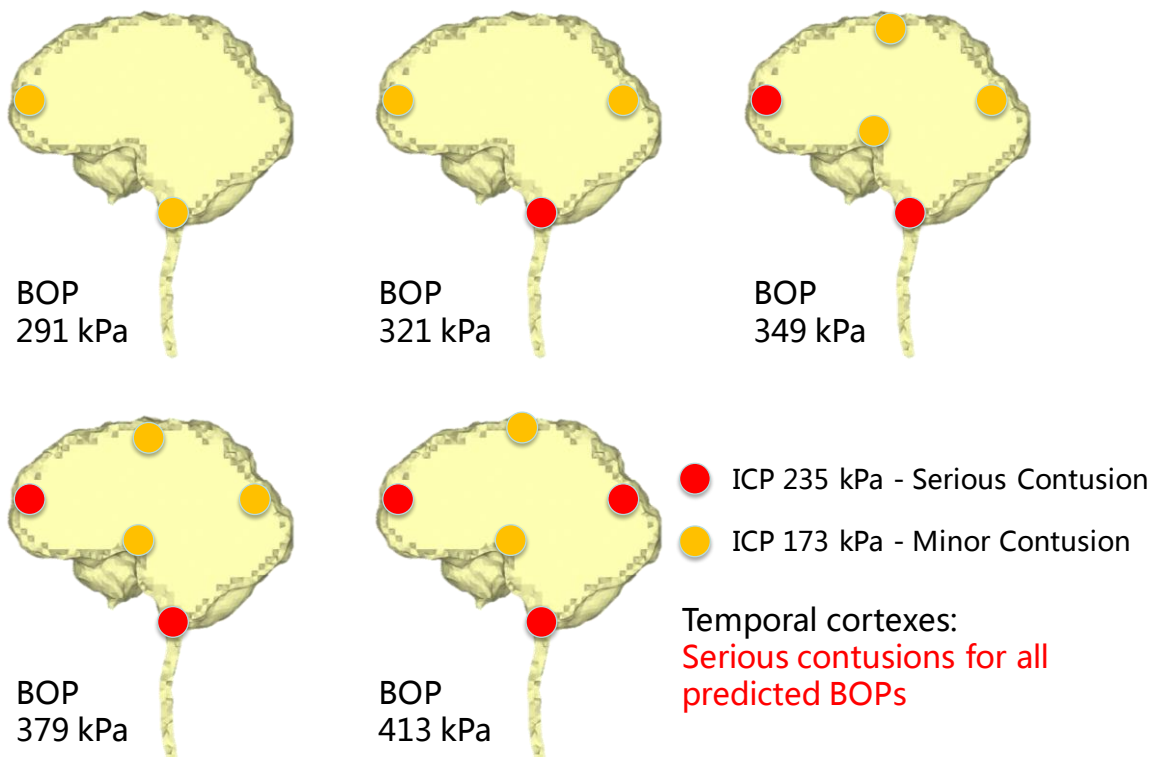


Figure 4-6. Predicted contusion injury location and severity of the right lateral blast-head simulations

Table 4-3. Predicted contusion injury severities at typical cerebral sites with respect to impinging BOPs at the blast incident side in the posterior blast-head simulations

<i>Peak BOP (TNT weight)</i>	<i>Cortex at SSS</i>	<i>Frontal cortex</i>	<i>Occipital cortex</i>	<i>Temporal cortexes</i>	<i>Hypothalamus</i>	<i>Lower Brainstem</i>
291 kPa (250g)	None	None	Minor	None	None	Serious
321 kPa (300g)	None	None	Serious	Minor	None	Serious
349 kPa (350g)	Minor	None	Serious	Minor	None	Serious
379 kPa (400g)	Minor	None	Serious	Serious	Minor	Serious
413 kPa (450g)	Minor	None	Serious	Serious	Minor	Serious

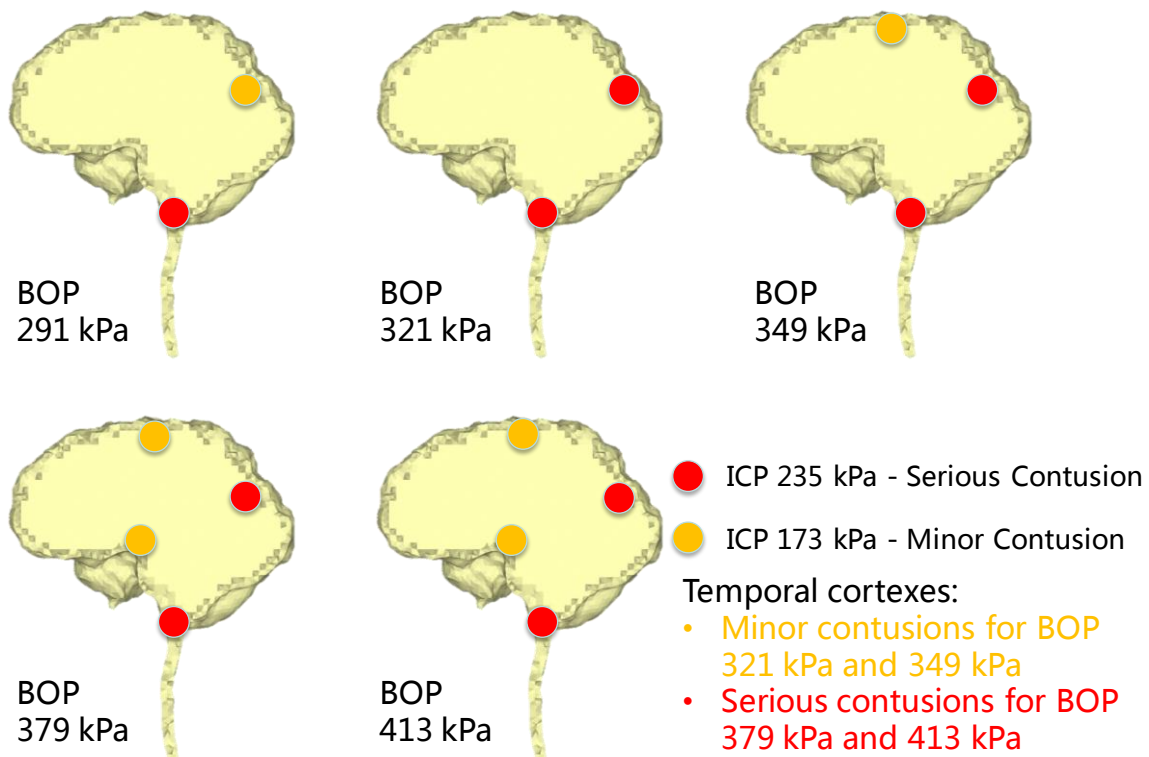


Figure 4-7. Predicted contusion injury location and severity of the posterior blast-head simulations

The lateral blast exposure was the most injurious orientation to the cortex among the three exposure orientations for the same blast severity, while the posterior exposure was the most injurious orientation to the lower brainstem. The lower brainstem is shown to be particularly vulnerable to have contusion in bTBI because the pressure waves were ultimately funneled into the foramen magnum and the vertebral column for every blast scenario (Figure 4-4), which subjected the inferior cerebellum, medulla and spinal cord to large pressure fluctuations. Although the positive peak pressure responses along the brainstem were similar to that of the cortex that was proximal to the blasts in the right lateral and posterior orientations, they created additional risks for injuries because the superficial veins along the anterior surface of the brainstem were likely to be vulnerable to injury. The posterior fossa area with the large peak-peak pressure differences contained the intracranial portion of the vestibulo-cochlear and trigeminal nerves, which, if damaged, could contribute to the dizziness, hearing loss and headache that were observed acutely with mild blast TBI (Hoffer et al. 2013, Hoffer et al. 2013). The intracranial pressure injury index of Ward et al. (1980) was stated as applicable to cerebral contusion, so, for the injuries of the spinal cord, this criterion may not apply. Therefore, this pressure-based injury criterion was not used in the present study for injury severity analysis of the spinal cord. A detailed quantitative assessment of spinal cord injury severity would be discussed once its widely recognized injury criterion became available.

In the literature of impact TBI, relative motion between the skull and brain has been validated as a cause of subdural hemorrhage during the impact or acceleration events (Gennarelli and Thibault 1982, Depreitere et al. 2006). Magnitudes of the relative skull-brain motion during impact and quasistatic circumstances have been assessed quantitatively by using *in vivo* MRI techniques (Feng et al. 2010, Monea et al. 2012). However, in the present study using the finite

element simulations, it was found no predicted relative displacement existed between the skull and the cortex at the SSS during the transient blast wave propagation through the head (zero displacement plots are not shown here). Therefore, unlike for the TBIs induced by impact or acceleration, primary bTBI is conjectured to not be caused by the relative motion between the skull and brain. The combination of this fact and the foregoing discussions of the pressure distribution pattern of bTBI consolidates our conclusions that the bTBI injury mechanism is primarily attributed to the propagation of the intracranial pressure wave induced by the direct transmission of the blast wave into the cranium and that the "coup-contrecoup" injury mechanism observed for impact- or acceleration-induced TBIs (Hardman and Manoukian 2002, Zhang et al. 2004) does not apply to bTBI.

4.3 BRAIN SHEAR STRESS RESPONSE TO HORIZONTAL BLAST

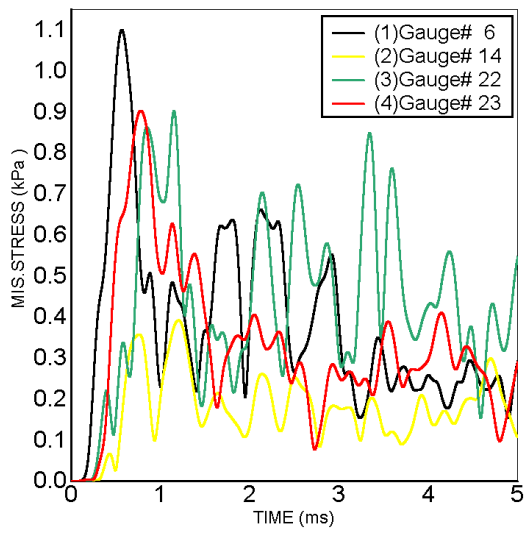
Von-Mises stress was taken as the indicator of the cerebral shear stress analysis for the present study. By examining the shearing responses throughout the brain in all the fifteen simulation cases, the cortex, brainstem, and spinal cord were found to be the primary locations that experienced high-level shear stresses, and the inner brain had the lowest shear stresses, which were all less than 0.1 kPa. It is believed that the density difference between the brain matter and the CSF caused the sliding over one another, stretching the neurons that traverse the interfaces between the areas of different densities. This sliding force between the brain and the CSF caused high-level shear stress at the cerebral surface adjacent to the CSF, whereby the intracranial tissues absorbed the kinematic energy of the blast wave transferred to them. The cortico-medullary junction (gray matter-white matter junction) experiencing high-level shear stresses

contained significant amounts of the neuron axons, which connected the gray matter and white matter, and thus appear to be particularly vulnerable to shear stresses. These in turn, caused DAI lesions by stretching, separating, and disrupting the nerve fiber tracts (Taber et al. 2006, McAllister 2011).

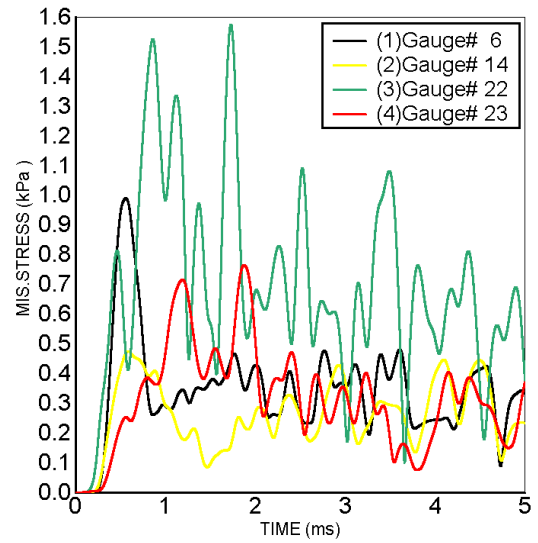
Like the pressure responses, for the same cerebral location, the pattern of the time-history of von-Mises stress remained the same as the blast strength varied, although the peak von-Mises stress increased with increasing blast strength. For every simulation case, the peak shear stresses in the brainstem and spinal cord were higher than that in the cortex. In the anterior blast cases, the highest von-Mises stresses of cortex occurred at the frontal region (gauge No. 6) with the peak values ranging from 0.73 kPa to 1.10 kPa; for the right-lateral blast cases, the highest von-Mises stresses in the cortex occurred at the right temporal region (gauge No. 22) with the peak values ranging from 1.09 kPa to 1.58 kPa; in the posterior blast cases, the highest von-Mises stresses of cortex occurred in the right temporal region (gauges No. 22) with the peak values ranging from 0.74 kPa to 1.18 kPa. The anterior blast cases had the highest shear stresses at the lower brainstem/medulla oblongata with peak values ranging from 1.55 kPa to 2.81 kPa, whereas the right lateral and posterior blast cases had the highest shear stresses in the spinal cord, which have peak values ranging from 1.33 kPa to 2.06 kPa, and from 1.48 kPa to 2.10 kPa, respectively. The spinal cord was not the point of interest of this study, so the injury analysis of DAI did not include the results of the spinal cord.

The von-Mises stress results of all the fifteen horizontal blast-head simulations are not shown here. As a typical example, the time histories of von-Mises stress for the gauges No. 6, No. 14, No. 22, and No. 23 at the cortex in the 450g TNT cases are shown in Figure 4-8. In each of the blast orientations, the von-Mises stress time histories at some of the cortex locations

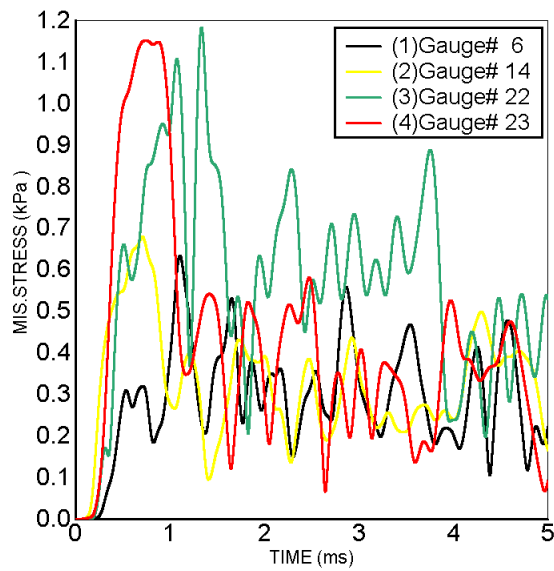
showed a "impulse-like" pattern, i.e. a similar pattern of the BOP and the intracranial pressure time histories, such as the gauges No. 6 and No. 23 in the anterior blast cases, the gauge No. 6 in the right lateral blast cases, and the gauge No. 23 in the posterior blast cases. Despite of the "impulse-like" time history pattern of the von-Mises stresses of some cerebral locations, the time histories of von-Mises stresses of several cerebral locations still developed after 1 ms throughout the whole simulation time, showing a time history pattern quite different from the "impulse-like" pattern of the intracranial pressure-time histories. Figure 4-9 shows the time histories of von-Mises stresses on the lower brainstem of the three 450g TNT blast-head simulations of three exposure directions, along with the corresponding intracranial von-Mises stress distributions at the occurring times of the peak von-Mises stresses at the lower brainstem of the three orientations. Because the foramen magnum contained the anatomic structures with different densities in this limited space, which could concentrate more energy from the blast, the lower brainstem did not show any clear or unique pattern of the von-Mises stress time histories which developed and maintained high levels through the whole simulation time (Figure 4-9a). The concentration of high von-Mises stresses on the cerebral tissues adjacent to the CSF is clearly revealed in every blast orientation (Figure 4-9b).



(a)



(b)



(c)

Figure 4-8. von-Mises stress time histories of the gauge points No. 6 (frontal cortex), No. 14 (occipital cortex), No. 22 (right temporal cortex), and No. 23 (left temporal cortex) in the 450g TNT blast-head simulation cases: (a) Anterior blast orientation, (b) Right lateral blast orientation, (c) Posterior blast orientation

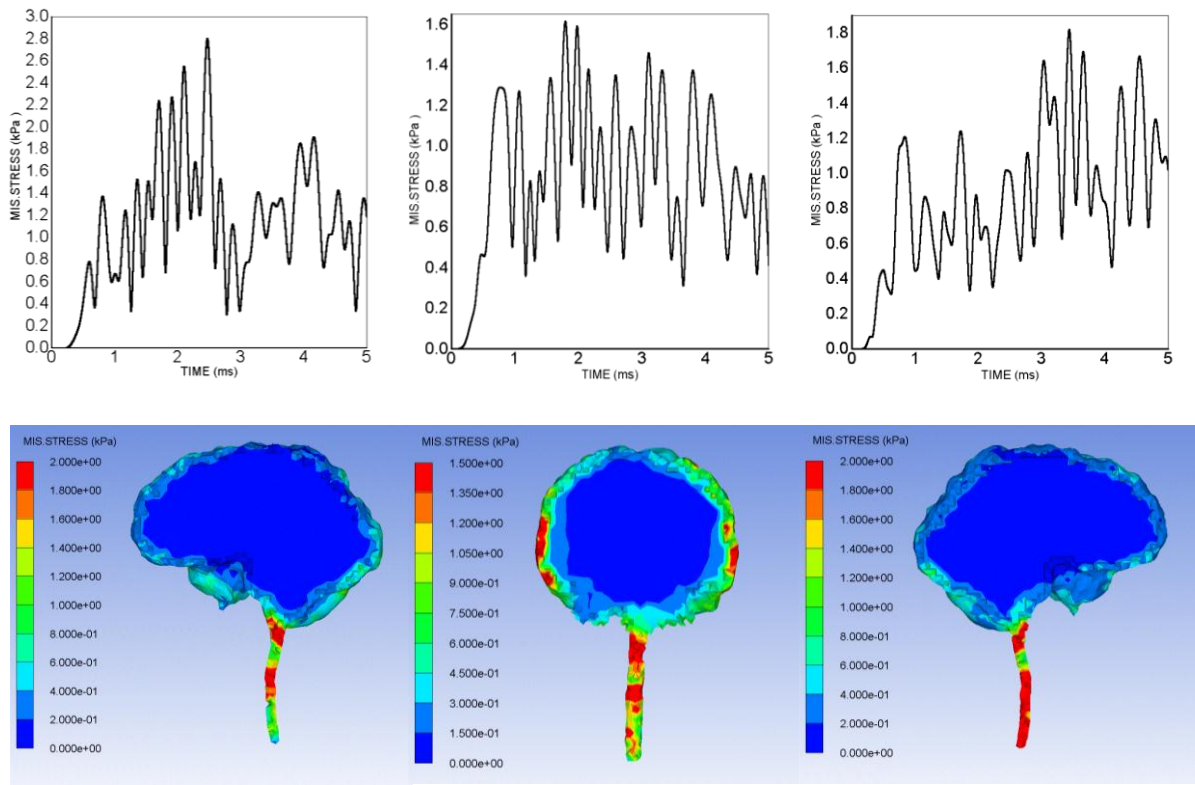


Figure 4-9. von-Mises stress time-histories of gauge No. 19 at lower brainstem and the associated von-Mises stress distributions showing peak von-Mises stresses in the 450g TNT blast-head simulation cases: left - anterior orientation (2.45 ms), middle - right lateral orientation (1.85 ms), right - posterior orientation (3.43 ms)

Among all the three simulation sets, the anterior blast-head simulations had the highest values of peak von-Mises stresses at the lower brainstem/medulla oblongata. The right lateral blast-head simulations had two primary intracranial sites (right temporal cortex and lower brainstem/inferior cerebellum within the posterior fossa) experiencing high-level von-Mises stresses with similar magnitudes. Similar to the anterior blast scenario, the posterior blast scenario had high-level von-Mises stress at the lower brainstem site, but the magnitudes were lower. Shear stress was proposed as the primary injury predictor of axonal injury for impact TBI in the study of Zhang et al. (2004), who estimated the tolerable von-Mises stress levels within the brainstem to be 6.0 kPa, 7.8 kPa, 10.0 kPa for 25%, 50%, 80% probability of mild TBI. The highest value (2.81 kPa) of von-Mises stress in the present study was much lower than this axonal injury criterion, therefore, it is hypothesized that shear stress might not be the primary injury causation of blast TBI as opposed to intracranial pressure. However, without the direct evidence from clinical study or a rigorous quantitative study relating axonal damage to specific pressure and shear stress levels, it was hard to conclude which type of mechanical responses in the brain was the primary TBI causation.

5.0 BLAST-HEAD INTERACTION SIMULATIONS OF EXPOSURE TO GROUND BLAST

This chapter presents the second blast-head simulation scenario, which simulated a person (only the human head was modeled) experienced the blast waves generated from a variety of TNT detonations the near ground in front of the person. The charges of the TNT detonations were still 250g, 300g, 350g, 400g, and 450g. The patterns of the blast waves and the intracranial pressure waves were analyzed. The regions with highest injury in the human head were found to be the lower brainstem and the frontal cortex, which were closest to the impinging blast waves. The injury severities of cortical contusions in the ground blast scenario were estimated based on the predicted intracranial pressure levels. The high shear stresses (von-Mises stresses) distributed on the surface of the whole brain model. The frontal and temporal cortexes sustained the highest amounts of shear stresses. Based on the available axonal injury criterion based on von-Mises stress, shear stress was conjectured as the inferior injury causation as opposed to intracranial pressure.

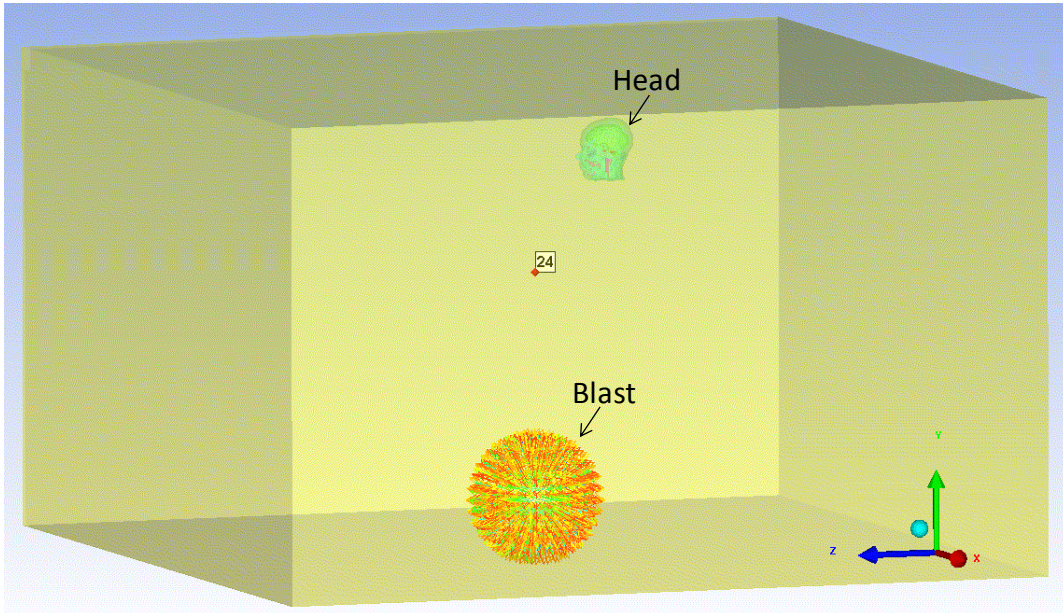
5.1 PREPROCESSING OF SIMULATIONS

The air space Euler-FCT model was established as described earlier in the section 3.3, therefore the dimension, mesh, and material properties of the air space model were the same as that used in

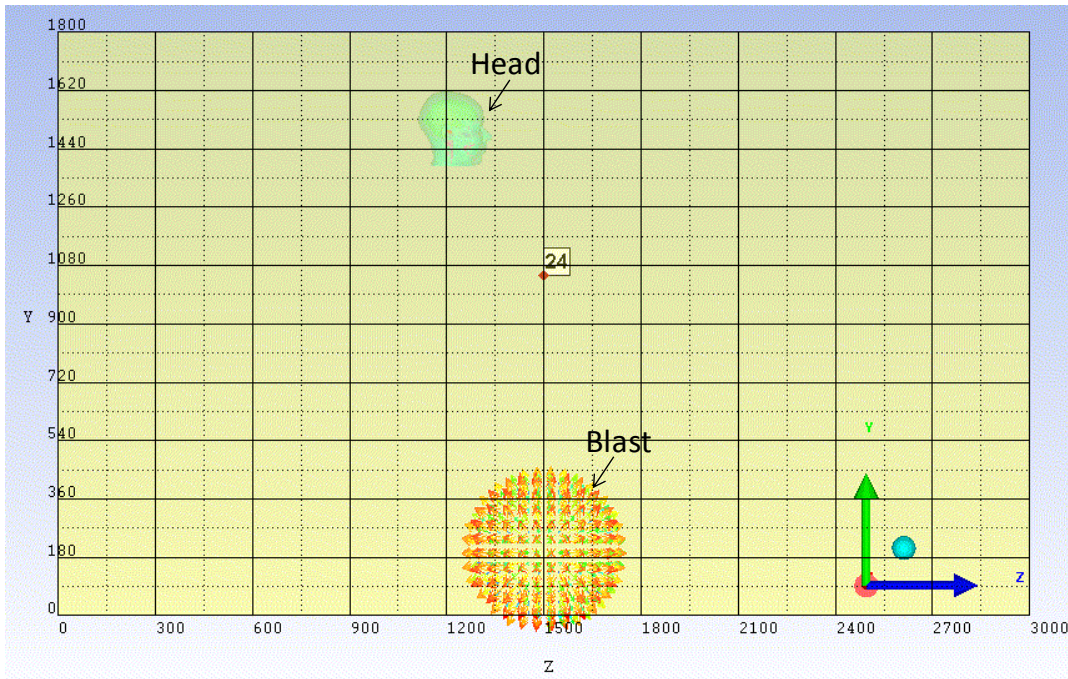
the simulations of horizontal blasts. The bottommost surface of the 3D air space model was left as a closed boundary condition, and all other five surfaces were assigned as open boundary conditions which let the blast waves propagate out of the space in order to make the simulated blasts comparable to the real free-field blasts. The closed boundary condition of Euler-FCT mesh reflects any blast wave toward it back to the mesh, thus the bottommost surface of air space performed like an actual reflective ground plane in the battle field.

The detonations of the five TNT charges were modeled as five 2D spherical air blasts of 200 millimeter radius in AUTODYN[®]. Then the state information of each air blast 2D model was transferred into the 3D air space to form an initial 3D spherical air blast model for each of the five ground blast-head simulations (Figure 5-1a). In the 3D air space, the detonation center of each spherical blast was located 200 millimeter vertically away from the ground surface, also had the x-z coordinate coincident with that of the center of the ground surface. In sum, the coordinate of the detonation center was (1500 mm, 200 mm, 1500 mm).

The person exposed to ground blasts was modeled to be 1.62 meters high and the face was a 150 mm distance from the detonation center along the z direction (Figure 5-1b). A gauge point was placed in the 3D space above the blasts. In addition, the location of the air gauge was kept the same as that in the simulations of horizontal blast exposures in order to quantify the extent that the pressure levels of the blasts which were reinforced by ground reflections. The twenty-three gauges in the FE head model were kept at the same locations as these in the simulations of horizontal blast exposures. The bottom of the neck was not assigned any restriction. The duration of every ground blast-head simulations was set to 5 milliseconds.



(a)



(b)

Figure 5-1. Ground blast exposure simulation scenario: (a) 3D view, (b) Y-Z plane view

5.2 BRAIN PRESSURE RESPONSE TO GROUND BLAST

Similar to the explosions in the open space, the ground explosion formed a hemispherical blast wave expanding and propagating radially in the 3D air space, taking the 250g TNT ground blast-head simulation as an illustrative example (Figure 5-2). At the beginning of the simulation, the bottom half of the initial spherical blast wave traveled toward the ground. Upon the initial blast wave reaching the ground, it was then reflected back to the space above. The reflected blast wave reinforced the initial blast wave and formed a new hemispherical blast wave which had a higher pressure level near the ground (the lower part of the entire blast wave). In the lower part, the initial blast wave completely merged with the reflected wave to form a single shock front which propagated horizontally. While in the upper part of the blast wave, the reflected wave did not fully merged with the initial blast wave due to the distance between the shock fronts of the initial and reflected blast waves. This made a secondary blast wave behind the initial blast wave (Figure 5-2).

The blast wave impinged the head model from below. Relative skull-brain motion was not observed during the process of the blast wave-head interaction. The time lapse pressure distribution of the brain in Figure 5-3 shows that the high pressure region transmitted from the spinal cord to the brainstem, and then to the cerebellum and cerebrum. In the ground blast scenario, the blast incident regions were the spinal cord, brainstem, cerebellum, and frontal lobe, which had higher levels of positive pressure than those of the distal regions including the parietal and occipital lobes. In the transmission of the intracranial pressure wave, the magnitude attenuation of the positive pressure was remarkable. The spinal cord exhibited high pressure levels in terms of both positive and negative pressure.

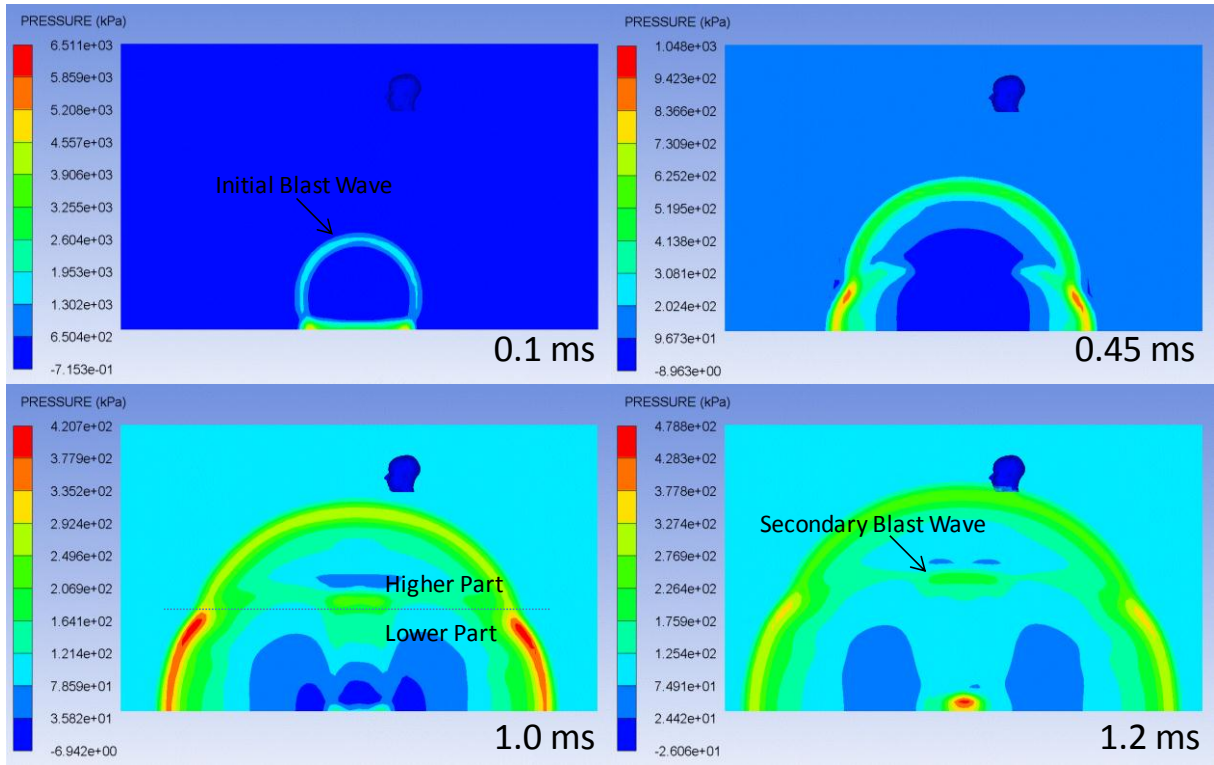


Figure 5-2. Blast wave propagating during the first 1.2 ms of the 250g TNT ground blast-head simulation

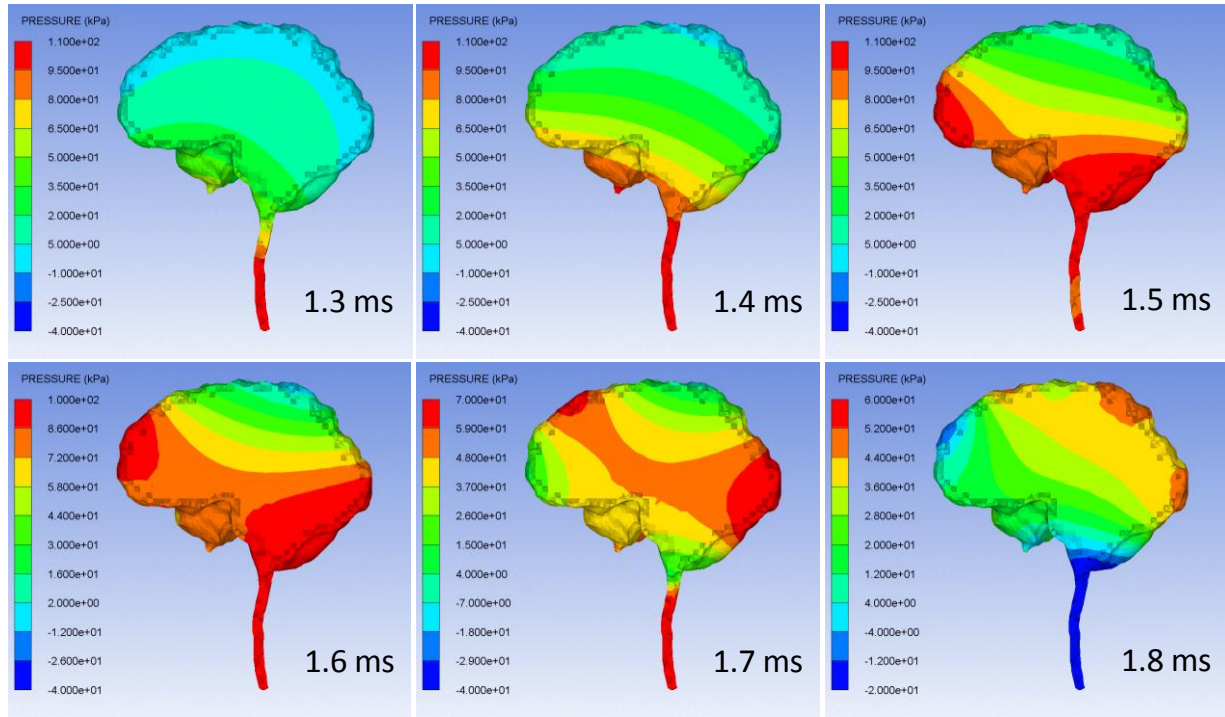
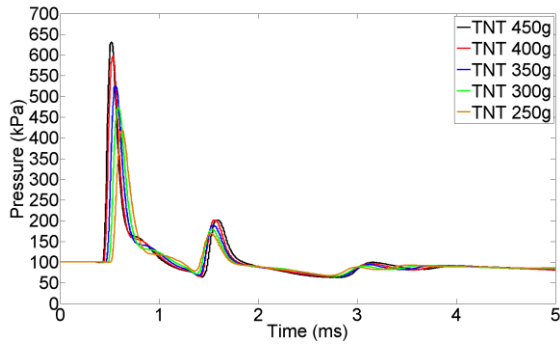


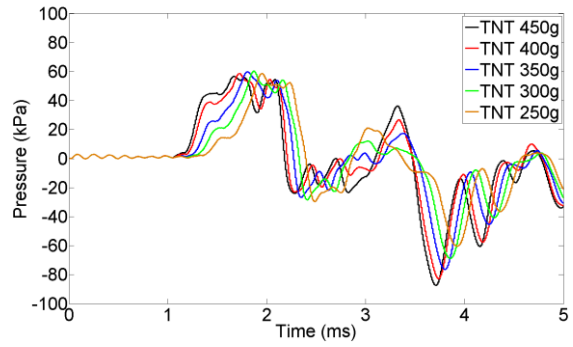
Figure 5-3. Pressure distributions of the brain in the 250g TNT ground blast-head simulation from 1.3 ms to 1.8 ms

Except for the parietal lobe, various intracranial locations had the wave patterns that were similar to that of the ambient blast wave. In these locations, the typical pattern of the pressure-time histories contained a main crest which possessed the peak positive pressure. The pressure time histories of the BOPs at some proximal locations had two crests (Figure 5-4c to Figure 5-4f). The first crest corresponded to the peak positive pressure of the initial blast wave, while the second crest corresponded to the secondary blast wave. The initial blast wave had a much higher pressure level than that of the secondary blast wave. With the increase of the TNT mass, the peak positive pressures of both the first and second wave crests increased and occurred earlier. The peak BOP value recorded for the smallest, 250g TNT charge, was about 4 times (419 kPa) of the standard atmospheric pressure, while that of the second crest was 169 kPa (Figure 5-4a). The ambient pressure eventually returned to the standard atmospheric pressure after the blast energy in the air space completely dissipated.

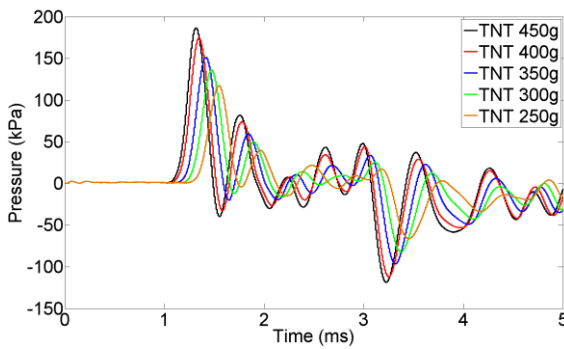
Higher peak BOPs caused higher peak positive pressures that occurred earlier in time in the proximal cerebral locations, while the pulse durations remained basically the same. However, in the CSF at the SSS, a distal cerebral location in the ground blast-head simulations, increased TNT mass did not increase the value of the peak positive pressure, instead, it increased the area that the main crest enveloped and increased the amplitude of the peak negative pressure (Figure 5-4b). In every ground blast-head simulation, the amplitude of the peak negative pressure was bigger than that of the peak positive pressure in the CSF at SSS. In contrast, at most intracranial locations proximal to blasts, the peak negative pressures had higher amplitudes than for the SSS, but they were lower than their respective positive pressures (Figure 5-4c to Figure 5-4f).



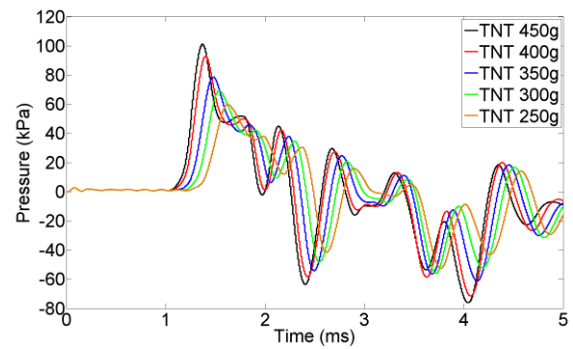
(a)



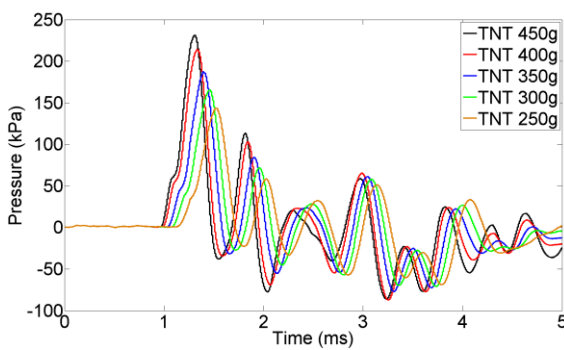
(b)



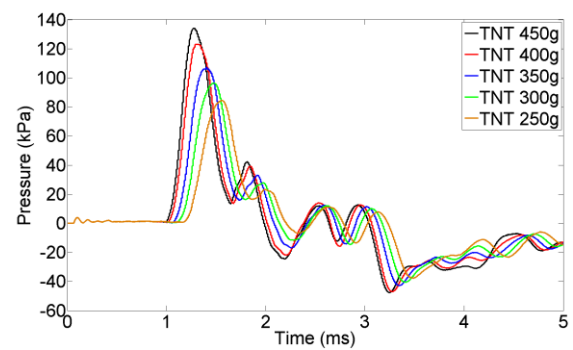
(c)



(d)



(e)



(f)

Figure 5-4. Pressure-time histories recorded by various gauge points of the five ground blast-head simulations: (a) No. 24 in atmosphere (b) No. 2 in the CSF at SSS, (c) No. 6 on the frontal cortex, (d) No. 14 on the occipital cortex, (e) No. 19 on the lower brainstem, (f) No. 21 on the hypothalamus

The pressure ranges of the typical cerebral sites are summarized in the Table 5-1, from which, it can be seen that the peak positive pressures at the locations of the side proximal to blast were higher than that of the distal side. The difference in the peak positive pressures between the proximal side and the distal side of the ground blast-head simulations was similar to that of the horizontal blast-head simulation scenario due to the same attenuation effect of the viscoelastic brain parenchyma.

Table 5-1. Pressure ranges in kPa at various cerebral locations: No. 3 (cortex at SSS), No. 6 (frontal cortex), No. 11 (brain parenchyma), No. 14 (occipital cortex), No. 19 (lower brainstem), No. 21 (hypothalamus), No. 22 (right temporal cortex)

<i>TNT</i> <i>mass</i>	<i>Gauge Number</i>						
	No.3	No.6	No. 11	No. 14	No. 19	No. 21	No.22
250g	[-55 to 57]	[-66 to 117]	[-30 to 58]	[-53 to 60]	[-69 to 143]	[-38 to 84]	[-35 to 91]
300g	[-62 to 58]	[-82 to 136]	[-30 to 69]	[-56 to 69]	[-71 to 165]	[-41 to 96]	[-40 to 103]
350g	[-69 to 58]	[-97 to 151]	[-32 to 77]	[-61 to 79]	[-77 to 187]	[-43 to 107]	[-45 to 113]
400g	[-74 to 57]	[-112 to 174]	[-37 to 91]	[-71 to 93]	[-87 to 215]	[-47 to 123]	[-57 to 129]
450g	[-78 to 55]	[-119 to 187]	[-41 to 98]	[-76 to 101]	[-86 to 231]	[-48 to 134]	[-63 to 137]

At the cerebral locations of the proximal side, the peak positive pressures were several times the amplitudes of the peak negative pressures. In comparison, at the distal side, the amplitudes of the peak positive pressures were very close to that of the peak negative pressures. Taking the 450g TNT ground blast-head simulation as an example, in the lower brainstem (gauge No. 19), the peak positive pressure was 231 kPa, which was almost three times of the amplitude of the peak negative pressure -86 kPa; whereas, in the occipital cortex (gauge No. 14), the peak positive pressure was 101 kPa, which was just 25 kPa more than the amplitude of the peak negative pressure was -76 kPa. At the cortex of SSS (gauge No. 3), except for the 250g

TNT case, the amplitudes of peak negative pressures were bigger than the peak positive pressures. Because the peak negative pressures developed after the blast wave propagated through the brain, the residual strain energy in the brain was speculated to be the cause of the negative pressures, indicating that tensile stress was the dominant cause of injury in the parietal cortex when blasts took place on the ground.

The lower brainstem experienced the highest peak positive pressures with the magnitudes ranging from 143 kPa to 231 kPa. This range was very close to that observed for the lower brainstem in the horizontal blast-head simulation scenario, despite of the longer head to blast source distance in the ground blast-head simulation scenario. The frontal cortex experienced the second highest level of peak positive pressures with the range being from 117 kPa to 186 kPa. This range was far below that of the horizontal and right lateral blast-head simulations. This large pressure difference in the same location between the ground blast scenario and the two horizontal blast-head simulation sets can be attributed to the longer distance from the blast center to the head and the protection of the head structure beneath the forehead in the ground blast scenario. However, the peak positive pressures of the frontal cortex in the 400g TNT and 450g TNT cases of the ground blast scenario were higher than that of the posterior blast scenario. Among all the intracranial locations, the frontal cortex tolerated the highest level of peak negative pressures ranging from -66 kPa to -119 kPa, which was considered less harmful to the brain than the associated positive intracranial pressures, which had higher magnitudes.

The internal brain parenchyma had its maximum positive pressures below 100 kPa and its maximum negative pressures above -50 kPa. The relatively low pressure conditions of the internal brain in the ground blast scenario were similar to that of the horizontal blast scenario, addressing the internal brain as the "safe region". An interesting outcome here is that

hypothalamus, though proximal to the blast, did not experience significant peak positive pressure. This could be attributed to the protection of the two skull layers on the pathway that the blast waves propagated to the hypothalamus. The temporal lobes experienced similar amounts of both positive and negative pressures to that of the hypothalamus.

The contusion injury severity and occurrence at various cerebral regions in the ground blast-head simulations were assessed using the cortical contusion criterion suggested by Ward et al. (1980). None of the cerebral locations had peak positive pressure of more than 235 kPa, the pressure level that induced the severe contusion. However, the frontal cortex in the 400g and 450g cases, and the lower brainstem in the 350g, 400g, and 450g cases were subjected to positive pressures above 173 kPa, therefore minor contusions would occur in the lower brainstem once the TNT mass exceeded 350g and in the frontal cortex once the TNT mass was more than 400g.

The "coup-contrecoup" injury pattern was still not observed in the ground blast-head scenario. However, at the distal side of the brain including the parietal and occipital cortexes, the peak positive pressures (compression) and the peak negative pressures (tension) occurred sequentially with equivalent magnitudes. This kind of compression to tension transition in the ground blast scenario was more obvious than for the horizontal blasts scenario, and thus could decrease the injury tolerance of the brain tissue at the distal side. In comparison, the impact induced TBI has the compression and tension with equivalent levels occurring simultaneously at the coup side and the contrecoup side, respectively (Zhang et al. 2004). Again, the posterior fossa was found to be the "vulnerable region", which subjected the inferior aspect of the cerebellum, pons, medulla, and cervical spinal cord to high positive pressures. It was expected that if the TNT charges of the ground blasts exceed a certain amount, the high level pressures at

the posterior fossa could injure its associated parenchyma and vasculature, for example causing brainstem hemorrhage.

5.3 BRAIN SHEAR STRESS RESPONSE TO GROUND BLAST

The shear stress analysis here is based on the von-Mises stress of brain. The brain experienced the highest amounts of shear stresses during the time range from 1.6 ms to 2.1 ms. As a typical example to illustrate the distributions of the von-Mises stresses, the time-lapse distributions of cerebral von-Mises stresses shown in the sagittal cross-sectional view for the 250g TNT ground blast-head simulation are depicted in Figure 5-5 at different times ranging from 1.6 ms to 2.1 ms in 0.1 ms intervals. The brain cortex, lower brainstem, lower cerebellum, spinal cord, and any other regions adjacent to the CSF, were again revealed to be the primary locations experiencing high level von-Mises stresses, i.e. the concentration of high shear stresses. In comparison, the central parenchyma experienced relatively low level shear stresses (Figure 5-5). In the core region of the central parenchyma, the von-Mises stresses were below 0.1 kPa for all the five simulations.

Although the spinal cord had much higher von-Mises stress than the other parts, it is not included in the discussion for TBI of the current study because the spinal injury is not considered as a topic of bTBI. However, it is hypothesized that the narrow column space concentrating a higher level of energy and the large density variations throughout its anatomic layers subjected the spinal cord to the large fluctuations of shear stresses.

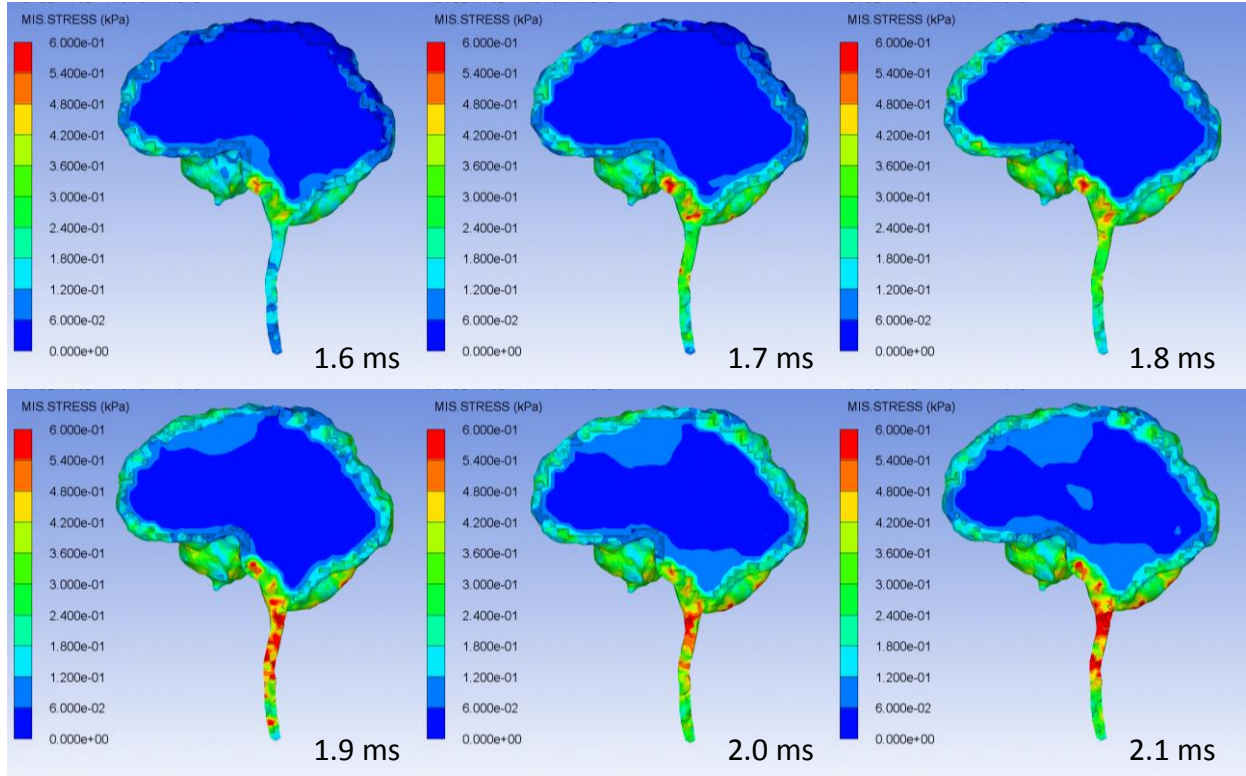
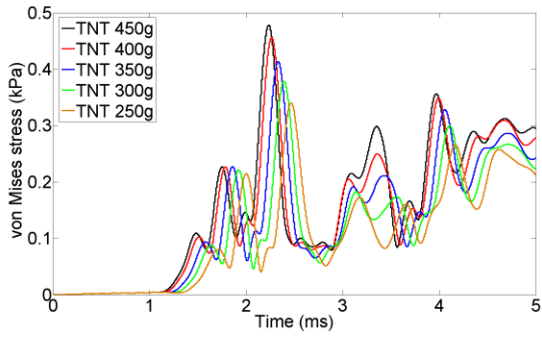
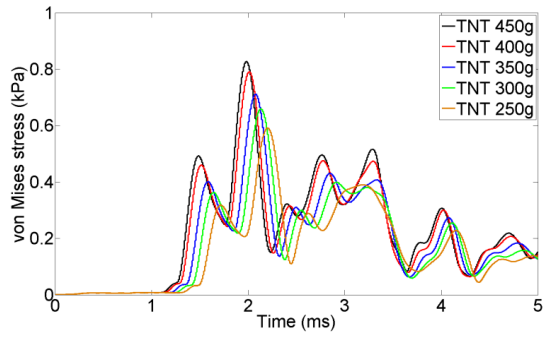


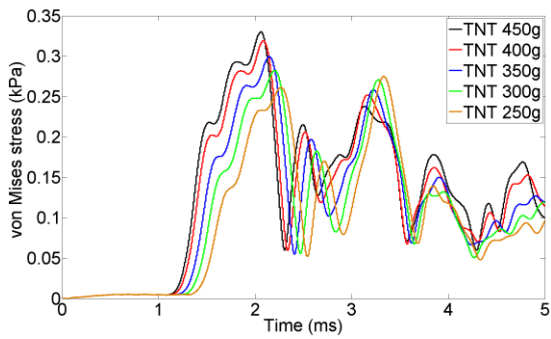
Figure 5-5. Distributions of von-Mises stress of the brain were shown in the sagittal cross-sectional view for the 250g TNT ground blast-head simulation at different times from 1.6 ms to 2.1 ms



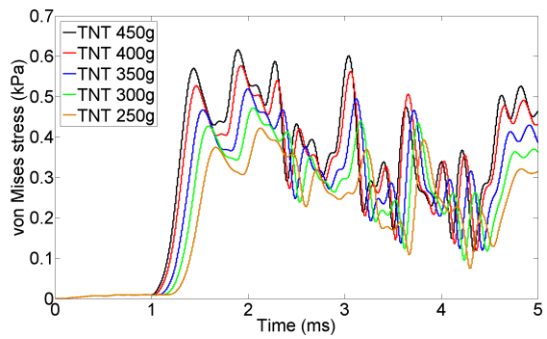
(a)



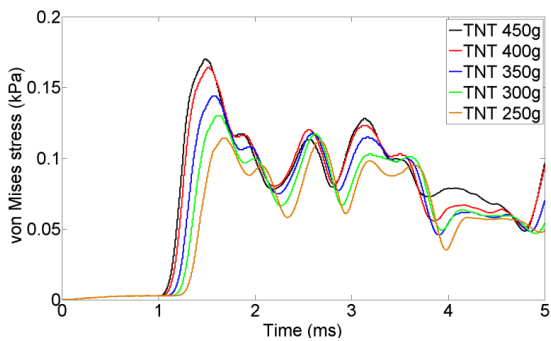
(b)



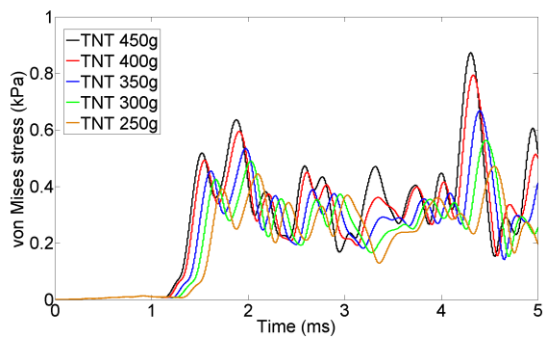
(c)



(d)



(e)



(f)

Figure 5-6. The time histories of von-Mises stress recorded by various gauge points of the five ground blast-head simulations: (a) No. 3 on cortex at SSS, (b) No. 6 on the frontal cortex, (c) No. 14 on the occipital cortex, (d) No. 19 on the lower brainstem, (e) No. 21 on the hypothalamus, (f) No. 22 on the right temporal cortex

The time histories of von-Mises stresses predicted at the cortex at SSS, frontal cortex, occipital cortex, lower brainstem, hypothalamus, and right temporal cortex are shown in Figure 5-6. The von-Mises stresses of the central parenchyma were less than 0.1 kPa for all the simulations, and therefore were not shown here. At any location in the brain, with the increase in the explosive mass from 250g TNT to 450g TNT, the pattern of von-Mises stresses stayed the same, while the peak value of the von-Mises stresses increased and occurred earlier. This phenomenon was similar to the relationship between the pressure responses of the brain and the blast intensity.

Although the shear stresses did not show an "impulse" pattern of the intracranial pressure, they still increased largely in the beginning stage. The von-Mises stresses at most cerebral sites except for the hypothalamus did not reach the peak magnitudes early (before 1.8 ms) in the blast wave-head interactions for all the five simulation cases. Figure 5-6 shows that the peak von-Mises stresses in the cortex at the SSS, frontal cortex, occipital cortex, lower brainstem, and right temporal cortex occurred after 1.8 ms, when the primary pressure waves had already passed these locations. This delay between the peak von-Mises stresses and peak intracranial pressures can be attributed to the time lag effect of brain viscoelasticity. Moreover, after the peak magnitudes occurred, the von-Mises stress maintained a high level. This is quite different from the "impulse" pattern of the intracranial pressures. Taking the 450g TNT simulation case as an example, the von-Mises stress of the lower brainstem reached a peak magnitude of 0.62 kPa at 1.89 ms, while at 3.04 ms, the stress magnitude was 0.6 kPa, which was still considered high as compared with the peak magnitude. The other example was that in the right temporal cortex, the peak magnitude of von-Mises stress was 0.87 kPa occurring at 4.31 ms. Before 4.31 ms, the highest stress magnitude was 0.63 kPa occurring at 1.87 ms. Therefore, it is thought that the

consistent high shear stresses at the gray matter-white matter junctions might reduce the tolerance of neuron fiber tracks to shear stresses.

In the 450g TNT simulation case, the von-Mises stresses in the frontal cortex, lower brainstem, and the right temporal cortex were higher than 0.6 kPa. Among the locations proximal to blast, the hypothalamus had the lowest von-Mises stress 0.17 kPa, which was also the lowest von-Mises peak value possessed by all the cerebral locations, as shown in Figure 5-6. At the locations distal to blast, the cortex at the SSS and the occipital cortex had von-Mises stresses lower than 0.5 kPa. Therefore, with the exception of the hypothalamus, the von-Mises stresses were higher at the locations proximal to blasts. The temporal cortexes were subjected to the highest von-Mises stresses among all the cerebral locations in the 400g TNT and 450g TNT cases. However, in the 250g, 300g, and 350g TNT cases, the highest von-Mises stresses occurred in the frontal cortex instead of the temporal cortexes. The left temporal cortex had high shear stresses equivalent to the right temporal cortex, and therefore only the information of the right lateral temporal cortex was explicitly shown here.

Table 5-2 summarizes the peak von-Mises stresses at the frontal cortex, occipital cortex, and the right temporal cortex for all simulation cases. From Table 5-2, it is observed that the highest von-Mises stress of the brain in the ground-blast simulations was 0.87 kPa, which was much lower than that of the horizontal simulations. Therefore the cerebral von-Mises stresses in the ground blast-head simulations were far below the axonal injury criterion proposed by Zhang et al. (2004). This again supported the hypothesis that shear stress might not be the main injury causation of blast TBI as opposed to intracranial pressure. However, the positive correlation between the TNT mass and the shear stress at every cerebral location implies that once the TNT

mass exceeded a certain amount, the shear stress of brain could exceed the injury criterion and cause DAI injury.

Table 5-2. Peak von-Mises stresses in kPa at frontal cortex (gauge No. 6), occipital cortex (gauge No. 14), right temporal cortex (No. 22) of the five simulations cases

<i>Location/gauge number</i>	<i>TNT mass</i>				
	250g	300g	350g	400g	450g
Frontal cortex/No. 6	0.59	0.66	0.71	0.79	0.83
Occipital cortex/No. 14	0.27	0.28	0.30	0.32	0.33
Right temporal cortex/No. 22	0.47	0.56	0.67	0.80	0.87

6.0 BLAST-HEAD INTERACTION SIMULATIONS OF EXPOSURE TO BLAST IN A SMALL ROOM

In this chapter, a computational scheme was developed to determine the propagation patterns of the blast waves generated in a small room, which has complex wave reflections. This scheme was to simulate the scenario of a blast wave detonated in the space of a small room with one wall opened to the street battle. The charges of the detonated TNT in the small room were still 250g, 300g, 350g, 400g, and 450g as used in the foregoing two blast-head simulation scenarios. The mechanical responses of human head to the complex blast waves were analyzed to evaluate the brain injury severities and the correlations between the blast waves and the potential injuries. The von-Mises stresses of the brain were analyzed as well.

6.1 PREPROCESSING OF SIMULATIONS

The dimension, mesh, and material properties of the room model were modeled as a 3D air space by using the methods described earlier in the section 3.3. This simulation scenario consisted of five blast-head simulations which also used the 250g, 300g, 350g, 400g, and 450g TNT spherical charges. The FE head model was placed one meter away from the anterior surface of the room space and was at the center of the X-Z plane in which it was located. The head model faced to the 3D blast waves which were located at the anterior surface of the room space. Therefore, the

location and orientation of the FE head model, along with the blast settings and locations were completely identical to that of the anterior blast-head simulations.

Except for the anterior wall, all five other room walls were given closed boundary conditions which acoustically performed like rigid walls of a room. The anterior room surface was assigned an open boundary condition in order for the blast energy in the 3D space to be partially released, since a perfectly sealed room space was not realistic in real battle field. The boundary condition settings of the room space made it equivalent to a partially enclosed small room. Figure 6-1 shows the computational schematic of a 3D air blast within the Euler-FCT model of the small room.

An air gauge point (No. 24) was placed in the 3D space in front of the human face. And the other air gauge point (No. 25) was placed in the space behind the human head in order to track the time histories of the reflected blast waves impinging on the back of the head model (Figure 6-1). The locations of the twenty-three gauge points in the FE head model were kept the same as that in the simulations of horizontal blast exposures in order to comparatively quantify the intracranial pressure levels which were reinforced by the wall reflections. The bottom of the neck was not assigned any constraint, consistent with the foregoing simulation scenarios. The duration of every room blast-head simulation was set to 10 milliseconds because the reflected blast waves needed more time than the foregoing simulations to be fully completed.

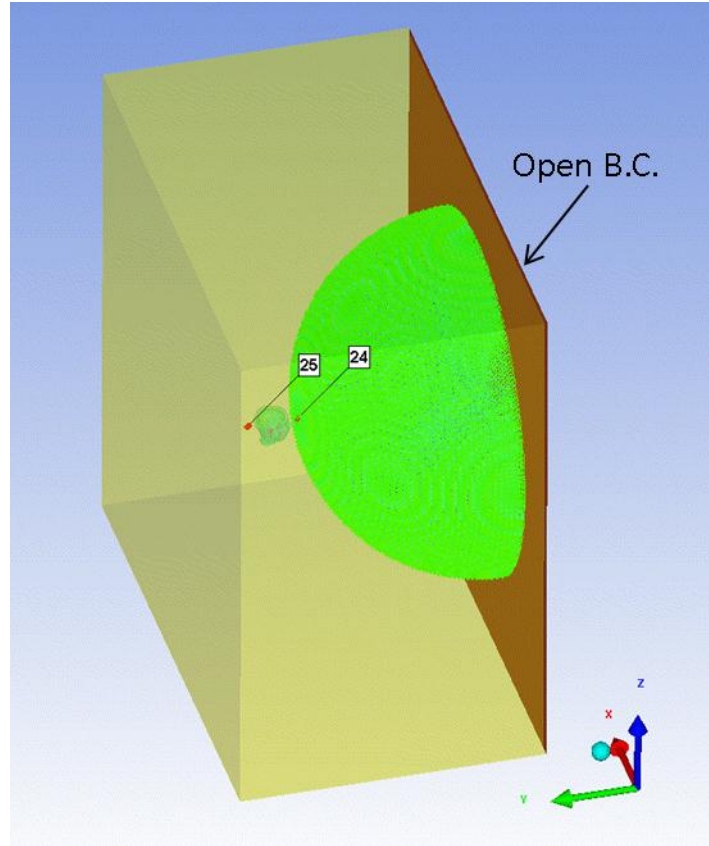


Figure 6-1. Computational schematic of 3D air blast within the small room which was assigned with open boundary condition (B.C.) at the anterior surface

6.2 BRAIN PRESSURE RESPONSE TO BLAST IN A SMALL ROOM

The five space surfaces assigned with closed boundary conditions reflected any blast wave incident upon them. The time-lapse contours of the blast waves moving in the room space at 2.0ms, 3.0 ms, 4.0 ms, 4.5 ms, 5.0 ms, and at 8.0 ms were shown in Figure 6-2. Figure 6-3 shows the time histories of the atmospheric pressures at the front space (gauge No. 24) and at the rear space (gauge No. 25) of the head model. It is observed that the wall reflections greatly affected the patterns of blast waves, and therefore very complex blast waves moving within the room space were formed. The reflected blast waves made this blast-head simulations scenario quite different with the foregoing ones.

Before impinging on the walls, the initial blast wave propagated the same as in the anterior blast-head simulations. Therefore, the peak pressures of the initial blast waves were the same as those observed in the anterior blast-head simulations (Figure 6-3a). Once the initial blast wave reached the walls, they were reflected and then propagated in new directions (Figure 6-2). The top wall, the bottom wall, the left lateral wall, and right lateral wall reflected the initial blast waves at 0.95 ms, and formed four symmetrical blast waves propagating toward the posterior wall obliquely, as shown in the 2.0 ms and 3.0 ms pictures in Figure 6-2. The initial blast wave reached the posterior wall at 1.65 ms, and formed a horizontal blast wave propagating toward the anterior wall. The new horizontal wave impacted on the back side of the head model around 3.0 ms, and therefore was indicated by the second wave crest shown in Figure 6-3b.

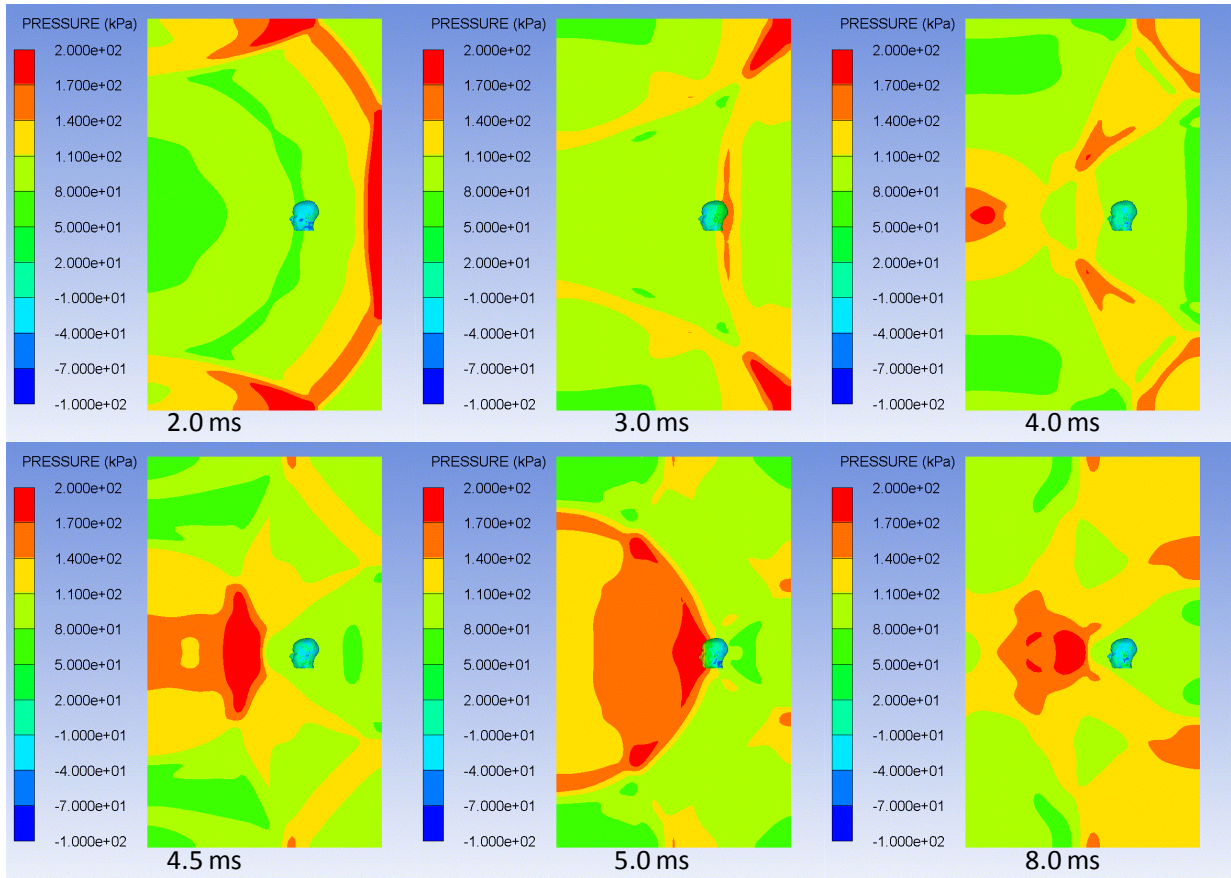
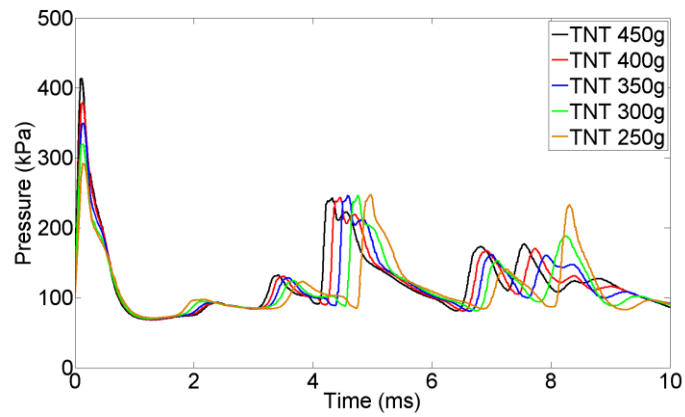
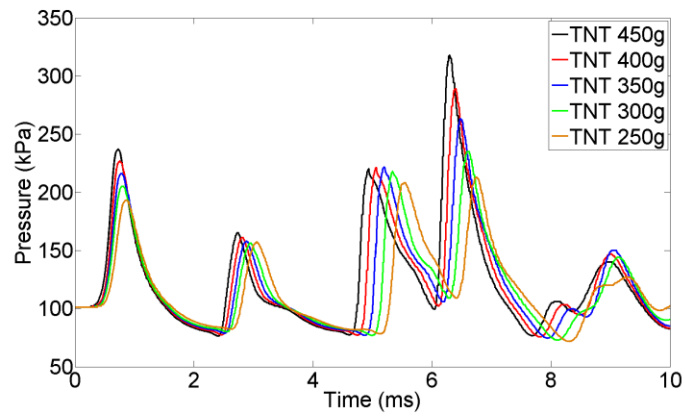


Figure 6-2. Time-lapse contours of a blast wave propagating within the room at 2.0 ms, 3.0 ms, 4.0 ms, 4.5 ms, 5.0 ms and at 8.0 ms for the 250g TNT room blast-head simulation



(a)



(b)

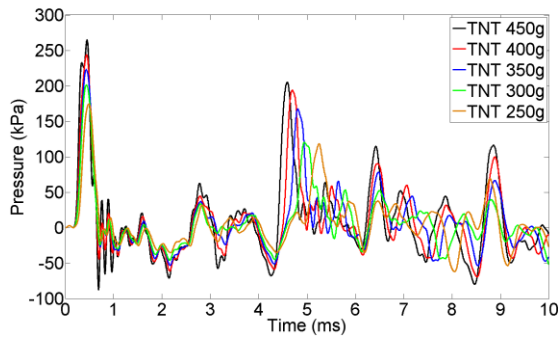
Figure 6-3. Atmospheric pressure time histories tracked by (a) the air gauge point No. 24 in the frontal space of the head model, (b) the air gauge point No. 25 in the rear space of the head model

The four oblique reflected blast waves interacted with the horizontal reflected blast waves as shown in the pictures at 3.0 ms, 4.0 ms, and 4.5 ms in Figure 6-3. Since the energy of the four oblique reflected waves was higher than that of the horizontally reflected waves, the interaction formed a new blast wave propagating toward the posterior wall. This new blast wave impacted the face of the head model around 5.0 ms, as shown by the 5.0 ms picture in Figure 6-2. This is also revealed by the second blast wave crest in Figure 6-3a. After 5.0 ms, the four oblique waves were reflected by the posterior wall and formed two strong blast waves impacting on the back side of the head model, as shown by the third and the fourth blast wave crests in Figure 6-3b. The fourth wave crest recorded by gauge No. 25 had the peak positive pressures ranging from 213 kPa to 318 kPa, which was the highest level among all the blast wave crests passing through the rear space of the head model. After the major energy of the blast waves in the room had dissipated from the anterior surface of the room space, the final reflected blast wave impacted on the head model 8.0 ms, as shown in the 8.0 ms picture in Figure 6-2.

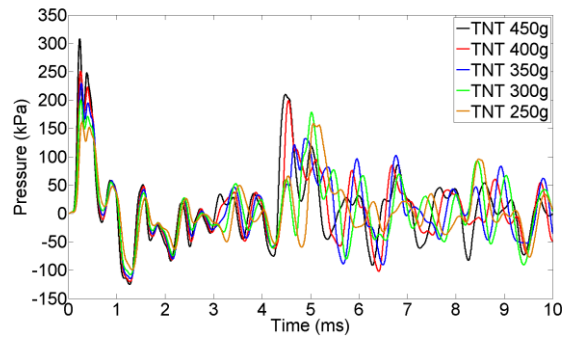
Figure 6-4 shows the pressure-time histories recorded by various intracranial gauge points. As expected, the initial blast wave and the reflected blast waves impacting on the head model resulted in a variety of pressure waves in the head model. For all of the intracranial locations, the initial crests of the intracranial waves were identical to those in the anterior blast-head simulations because the mechanical responses of the head model were identical to that in the anterior blast-head simulations before the reflected waves impacted on the head model. Around 3.0 ms, the intracranial waves exhibited a second crest which was caused by the reflected blast wave shown in the 3.0 ms picture in Figure 6-2. However, the second intracranial wave-crest was insignificant in the frontal cortex as compared to the other locations. Around 5.0 ms, the intracranial locations experienced their highest or the second highest wave crests, which

were induced by the reflected blast waves impacting on the face of the head horizontally at 5.0 ms, as shown in the 5.0 ms picture of Figure 6-2. Around 6.5 ms, the occipital cortex, the posterior margin of the tentorium cerebelli, the lower brainstem, and the right temporal cortex experienced significant wave crests, which were caused by the fourth crest of the blast waves, shown in Figure 6-3b, impacting on the rear side of the head model.

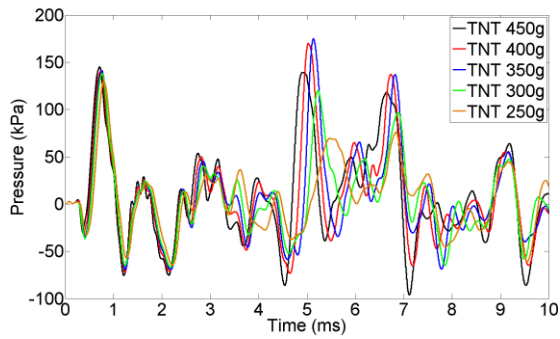
In the CSF at the SSS, frontal cortex, and lower brainstem, the peak positive pressures were achieved by the initial crests of the intracranial pressure waves formed by the initial, direct blast waveform for all the five cases. In the occipital cortex, the peak positive pressures for the 350g TNT and 400g TNT cases were created by the reflected blast waves; while for the 250g TNT, 300g TNT, and 450g TNT cases, the initial crests of the intracranial pressure waves created the peak positive pressures. In the posterior margin of the tentorium cerebelli, all the cases except the 450g case achieved the peak positive intracranial pressures from the reflected blast waves. In the left and right temporal cortexes, all the cases except the 250g case achieved the peak positive pressures from the initial blast wave. Therefore, the blast waves reflected by the room did increase the peak intracranial pressures at some cerebral locations.



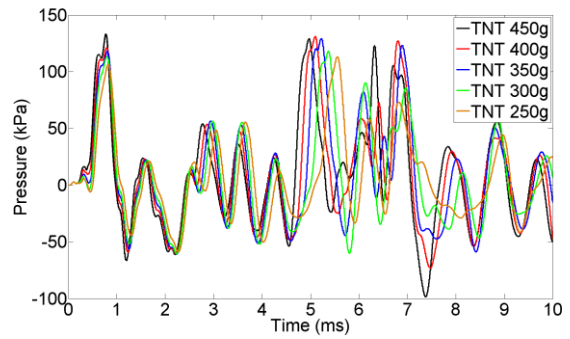
(a)



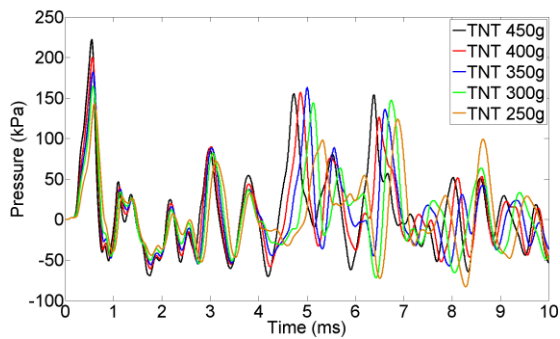
(b)



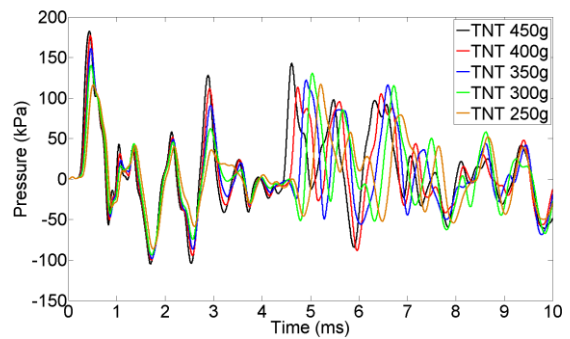
(c)



(d)



(e)



(f)

Figure 6-4. Pressure-time histories recorded by various gauge points for the room blast-head simulations: (a) No. 2 in CSF at SSS, (b) No. 6 in the frontal cortex, (c) No. 14 in the occipital cortex, (d) No. 18 at the posterior margin of the tentorium cerebelli, (e) No. 19 on the lower brainstem, (f) No. 22 on the right temporal cortex

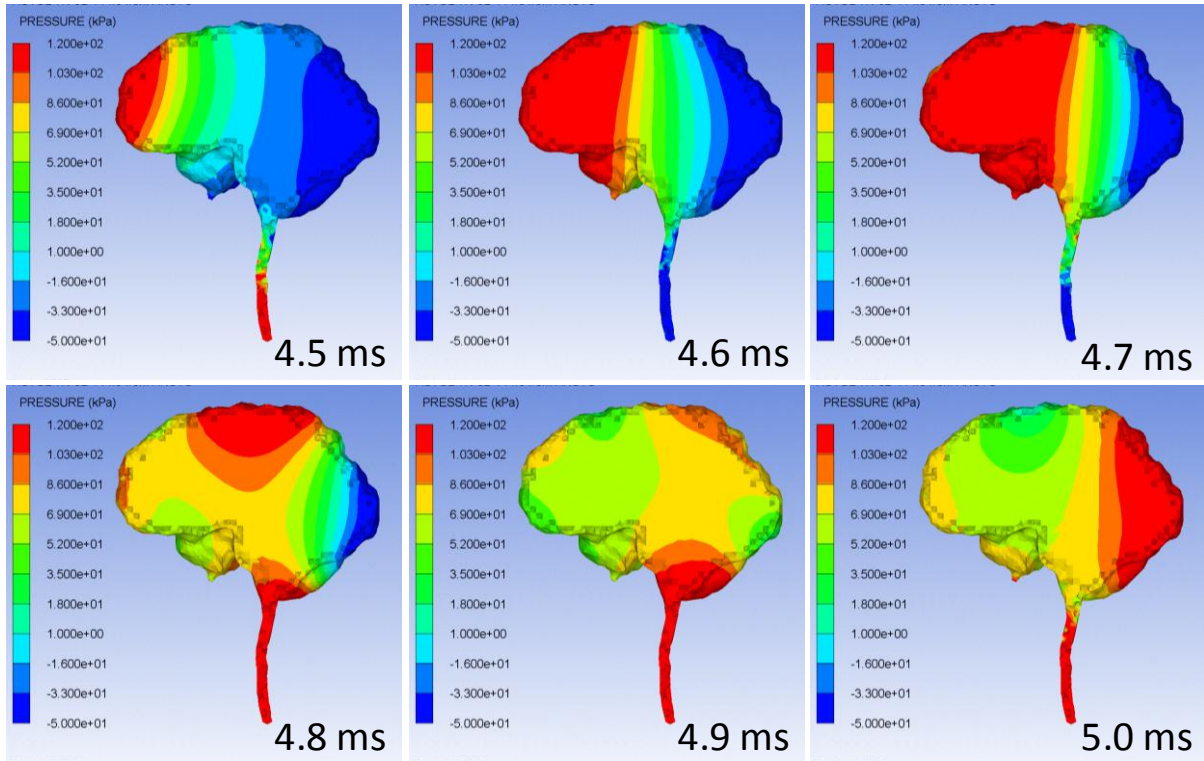


Figure 6-5. Pressure distributions of the brain in the 400g TNT room blast-head simulation from 4.5 ms to 5.0 ms

For the 450g TNT case, the occipital cortex achieved a peak negative pressure of -96 kPa at 7.1 ms; and the posterior margin of the tentorium cerebelli achieved a peak negative pressure of -99 kPa at 7.4 ms. Compared with the corresponding peak positive pressures, the magnitudes of these peak negative pressure were still at high levels. Since they were caused by the reflected blast waves impinging on the back of the head and were lower than the peak negative pressures obtained from the initial blast waves, the conclusion that the reflected blast waves could increase the peak intracranial pressures was validated. As discussed above, the sharp transitions from the high positive pressures (compression) to the high negative pressures (tension) at the same cerebral locations might bring additional damage to the brain. Sharper transitions from compression to tension were observed for the room blasts. Therefore, the room blast scenarios are also speculated to have higher potential to create damage than the open-field blast scenarios.

The time-lapse pressure distributions of the 400g TNT room blast-head simulation from 4.5 ms to 5.0 ms are shown in Figure 6-5, from which it is clearly observed that the intracranial pressure waves propagated from the frontal part to the rear part of the brain. The intracranial pressure waves during this time range were produced by the strongest reflected blast wave.

Contusion occurrences and severities at several cerebral locations were again evaluated by using the same index suggested by Ward et al. (1980), and are summarized in Table 6-1 and Figure 6-6. The prediction of contusion injury severities at the SSS cortex, frontal cortex, temporal cortexes, hypothalamus, and lower brainstem were identical to that of the anterior blast-head simulations. The only exception was the occipital cortex, which had a minor contusion in the 350g TNT case, but it had no injury in any other anterior blast-head simulation. The minor contusion in the occipital cortex for the 350g TNT case was induced by the strongest reflected blast wave impacting the head at 4.5 ms.

Table 6-1. Predicted contusion injury severities at typical cerebral sites with respect to impinging BOPs at the blast incident side in the room blast-head simulations

<i>Peak BOP (TNT weight)</i>	<i>Cortex at SSS</i>	<i>Frontal cortex</i>	<i>Occipital cortex</i>	<i>Temporal cortexes</i>	<i>Hypothalamus</i>	<i>Lower Brainstem</i>
291 kPa (250g)	None	None	None	None	None	None
321 kPa (300g)	Minor	Minor	None	None	None	None
349 kPa (350g)	Minor	Minor	Minor	None	Minor	Minor
379 kPa (400g)	Serious	Serious	None	Minor	Minor	Minor
413 kPa (450g)	Serious	Serious	None	Minor	Serious	Minor

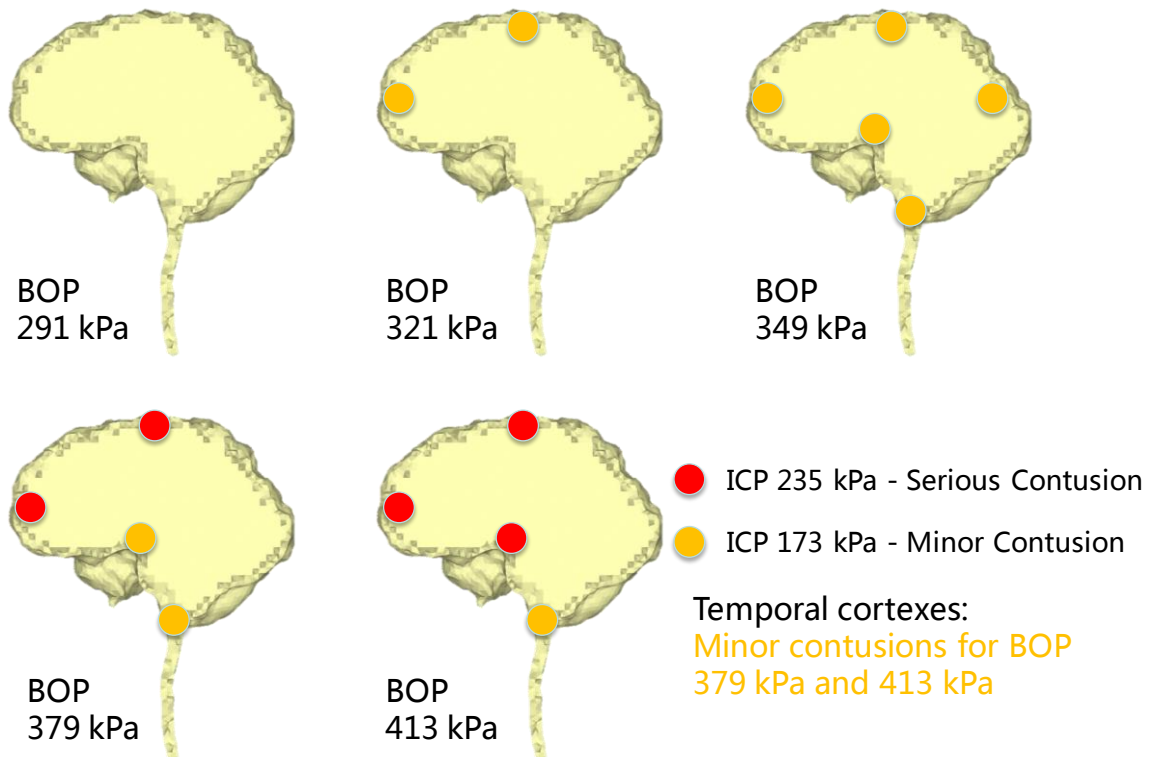


Figure 6-6. Predicted contusion injury location and severity of the room blast-head simulations

6.3 BRAIN SHEAR STRESS RESPONSE TO BLAST IN A SMALL ROOM

The analysis of the brain shear stress response to the room blasts was based on the von-Mises stresses of the brain as in the foregoing chapters. The time-lapse distributions of the cerebral von-Mises stresses in the sagittal cross-sectional view for the 400g TNT ground blast-head simulation were depicted in Figure 6-7 at different times ranging from 4.5 ms to 5.0 ms with 0.1 ms interval as the counterpart of the pressure distributions shown in Figure 6-5. Similar to the horizontal blast-head simulations and the ground blast-head simulations, the high shear stresses mainly occurred at the brain surfaces which were adjacent to the CSF, while the central parenchyma were subjected to comparatively low von-Mises stresses which were less than 0.15 kPa in all the five room blast-head simulations.

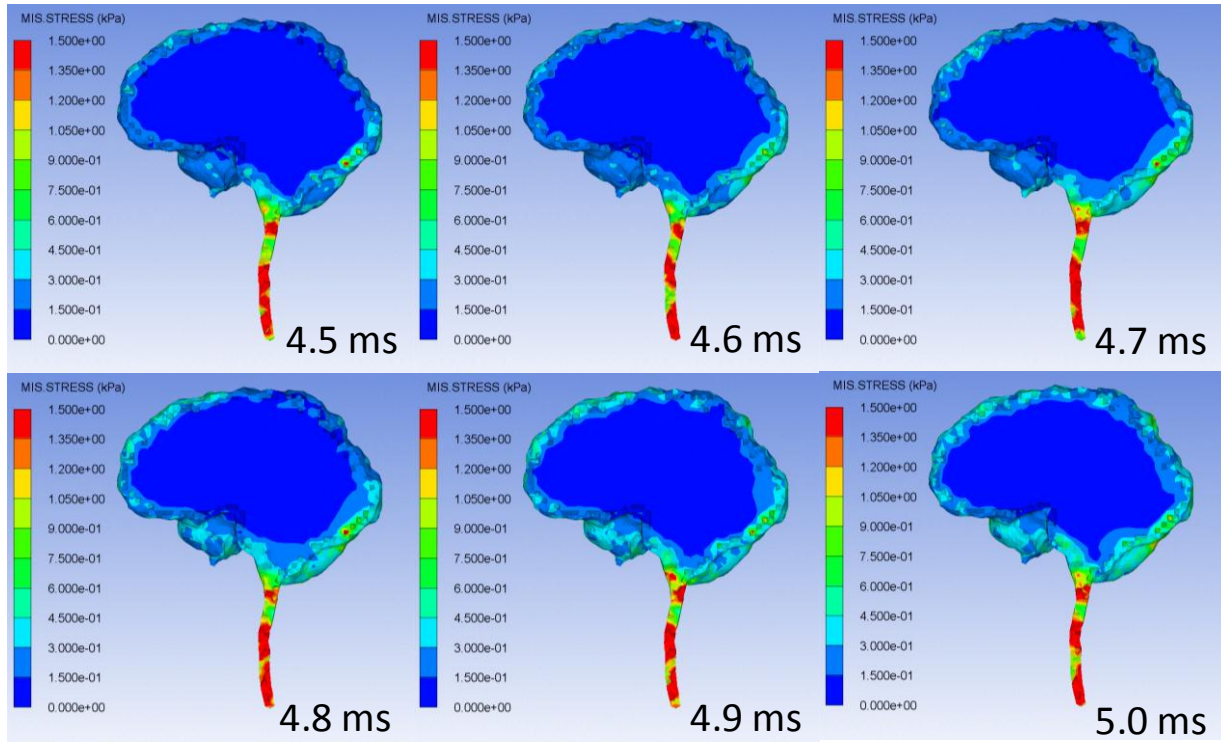
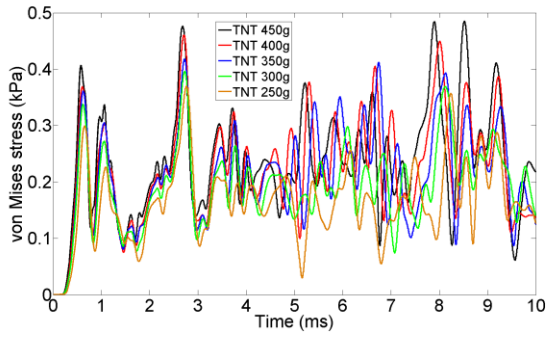
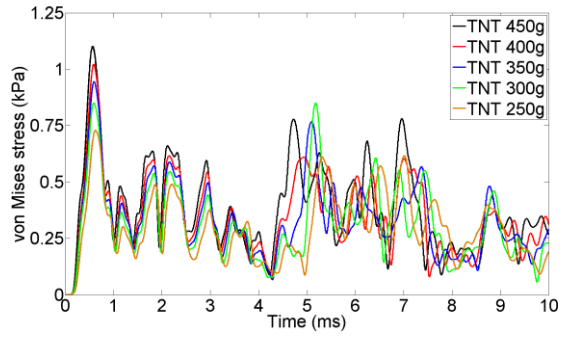


Figure 6-7. Distributions of von-Mises stress in the sagittal cross-sectional view of the brain for the 400g TNT room blast-head simulation at different times from 4.5 ms to 5.0 ms

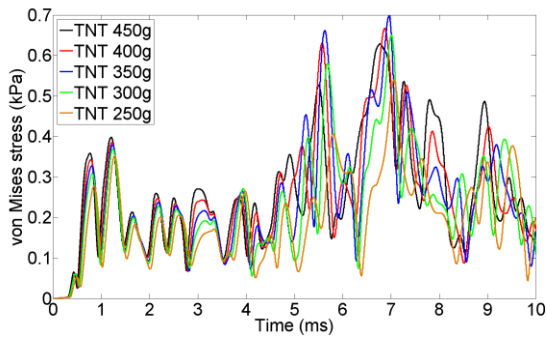
The time histories of the von-Mises stresses predicted at the cortex at the SSS, frontal cortex, occipital cortex, lower brainstem, hypothalamus, and right temporal cortex are shown in Figure 6-8. The time histories of the von-Mises stresses in the central parenchyma are not shown here because they were several orders of magnitude lower than that at the brain surface. Figure 6-8 shows that most of the cerebral locations experienced fluctuations of high von-Mises stresses. Before the reflected blast waves impacted the head model, the von-Mises stresses of the brain were identical to that of the anterior blast-head simulations. At the same cerebral location, the patterns of the von-Mises stresses for the simulations were similar but still had differences for the five levels of blast. At the hypothalamus, the patterns of the von-Mises stresses for the simulations remained the same during the whole 10 ms, while the peak von-Mises stress increased and occurred earlier as the explosive mass increased. However, in the cortex at the SSS, frontal cortex, occipital cortex, lower brainstem, and right temporal cortex, each of the patterns for the von-Mises stresses remained the same before 4 ms for each site, and varied thereafter, exhibiting the influence of the reflected blast waves. This phenomenon was similar to that observed for the pressure responses of the brain.



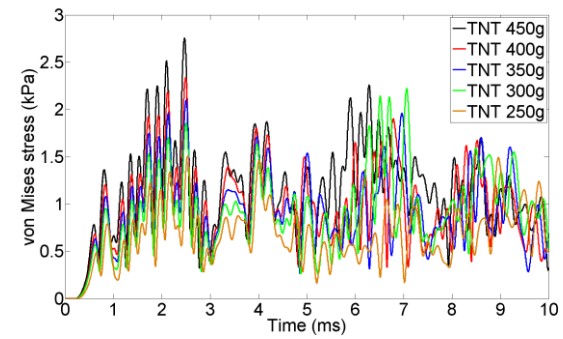
(a)



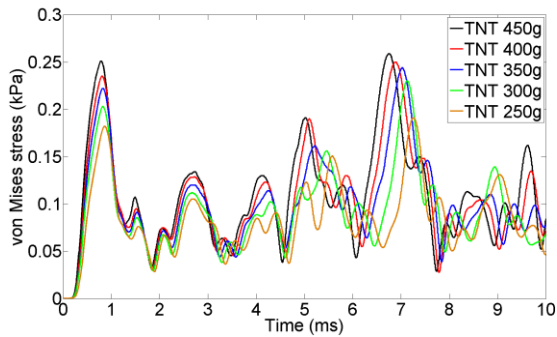
(b)



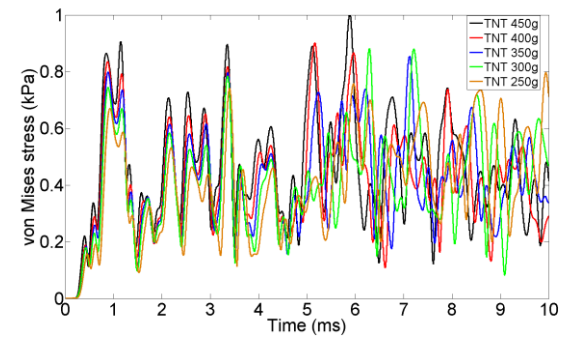
(c)



(d)



(e)



(f)

Figure 6-8. The time histories of von-Mises stress recorded by various gauge points for the room blast-head simulations with five amounts of TNT: (a) No. 3 on cortex at SSS, (b) No. 6 on the frontal cortex, (c) No. 14 on the occipital cortex, (d) No. 19 on the lower brainstem, (e) No. 21 on the hypothalamus, (f) No. 22 on the right temporal cortex

In the cortex at the SSS, the 450g TNT simulation case had the highest von-Mises stress after 4 ms, while the other four cases achieved the highest von-Mises stresses before 4 ms. In the frontal cortex, except the 300g TNT case, the other four cases had the highest von-Mises stresses before 1 ms. In the occipital cortex, all the five simulation cases achieved the highest von-Mises stresses around 7.0 ms, and the 350g TNT case had the highest von-Mises stress. In the lower brainstem, except the 300g TNT case, the other four cases had the highest von-Mises stresses before 4 ms. In the temporal cortexes, the highest von-Mises stresses of all the five simulation cases happened after 4 ms. Therefore, there was not a clear rule that governed the time of occurrence of the highest von-Mises stresses in the brain for the room blast scenario because the magnitudes of the von-Mises stresses at any cerebral location were affected by the intensities of the reflected blast waves impacting on the head model. Hence, the occurrence times of the highest von-Mises stresses at a cerebral location could indicate the intensity differences between the initial blast wave and the reflected waves impacting on the adjacent area of this location.

The maximum von-Mises stress of all the room blast-head simulations occurred at the lower brainstem for the 450g TNT case, with the same value (2.81 kPa) as that of the anterior blast-head simulations. According to the axonal injury criterion proposed by Zhang et al. (2004), the room blast-head simulations did not obtain any DAI lesions. This indicated that shear stress might not be the main injury causation of blast TBI as opposed to intracranial pressure in the room blast scenario, even though the reflected blast waves enhanced the level of shear stresses at some of the cerebral locations. While the consistent fluctuations of high level shear stresses might reduce the tolerance of the brain tissue to shear stress. Therefore, a DAI injury criterion including both the shear stress magnitude and the fluctuation of high shear stress should be addressed in future research.

7.0 FINITE ELEMENT ANALYSIS OF SUBDURAL HEMORRHAGE

Subdural hemorrhage/hematoma is the bleeding caused by BV damage or rupture within the subdural space (Gennarelli and Thibault 1982, Yamashima and Friede 1984). Subdural hemorrhage is one of the leading injury types of traumatic brain injury. In order to assess the occurrence and injury severity of subdural hemorrhage for the blast-head simulations conducted in the foregoing context, mechanical properties of BV were estimated by fitting experimental inflation results of a BV sample to a selected anisotropic hyperelastic constitutive model, and the finite element analysis (FEA) of BV rupture was performed by using the internal pressure loadings identical to the CSF pressures at SSS of the anterior blast-head simulations, which had the highest CSF pressures at the SSS among all the blast-head simulations. For every explosive mass, the highest CSF pressure at SSS in the anterior blast-head simulations and that in the room blast-head simulations were the same, therefore, this chapter conducted the FEA of subdural hemorrhage based solely on the results of the anterior blast-head simulations.

7.1 MECHANICAL TESTING OF HUMAN BRIDGING VEIN

Although some results of the mechanical experiments on human bridging vein were published recently (Pang et al. 2001, Monson et al. 2005), it was impossible to fit these experimental data to the hyperelastic constitutive models which were able to represent the 3D constitutive relations

between stress and strain. Hence, a standard inflation experiment for blood vessels was devised to generate suitable experimental data which could be used for curve fitting the measured mechanical properties of human bridging vein.

Three human bridging veins were harvested at autopsy. The bridging vein (BV) segments were catheterized (polyethylene venous catheter) after opening the superior sagittal sinus, and were maintained at *in-vivo* length with the microvascular clamps against the catheter. After the excision, the clamped vein samples and catheters were transported to the testing laboratory in containers with phosphate buffered saline (PBS) solution. The BV surrounding tissues were cleaned before mounting the BV samples onto the perfusion cannulae of the inflation-extension biomechanical testing system (Santelices et al. 2007, VanEpps et al. 2009) equipped with a non-contacting laser micrometer (Beta LaserMike, Dayton, OH). One intact BV sample maintained its integrity for the full testing. Figure 7-1 shows an intact human bridging vein was mounted in the inflation-extension vascular testing system before the onset of the inflation test. The BV segment was bathed in water and was kept at its *in-vivo* longitudinal stretch after pre-measuring the *in vivo* length of the BV segment. The structure of BV was extremely soft, therefore the shape of its cross section was deformed remarkably due to the lack of internal pressure after excision, therefore, the equilibrium state between the internal and external hydraulic pressures of BV was achieved by the adjustment of pre-perfusion such that the zero-load-state outer diameter of the BV could be accurately measured. The zero-load-state outer diameter of the BV was measured to be 2.027 mm by the laser micrometer. The inner diameter was 1.76 mm, as estimated from the average ratio of the wall thickness versus outer diameter of BVs in Monson et al. (2005).

Before the inflation test, ten preconditioning cycles were carried out on the BV section to eliminate the tissue-softening effects. After the preconditioning, the pressure-radius (P - r) curve was obtained by inflating the vessel segment across a range of pressures from 0-20 mm Hg (0-2.67 kPa) at the constant rate of 0.5 ± 0.1 mm Hg/s (66.6 ± 13.3 Pa/s). During the inflation, the increasing BV external diameter was measured by the laser micrometer. The corresponding inflating pressure was measured by a pressure sensor (TruWave transducer, Edwards lifesciences, Irvine, CA). The measured data of the changing diameter versus the corresponding inflation pressure were recorded by a PC-based data acquisition system. This data was then processed and was used for the following work of characterizing the mechanical properties of bridging vein in a selected anisotropic hyperelastic constitutive model. Ideally, multiple specimens would be tested and averaged, however additional samples were not available. Nonetheless, a method of fitting data from any future experiments has been devised.

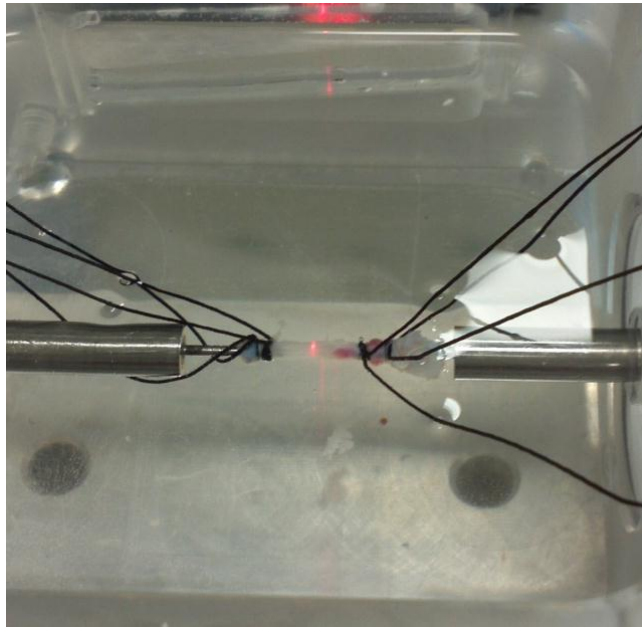


Figure 7-1. Human bridging vein mounted in the inflation-extension vascular testing system (Wang et al. 2012)

7.2 CONSTITUTIVE MODELING AND MATERIAL CURVE FITTING OF BRIDGING VEIN

The elastin/ground matrix and collagen fibers are the two major structures bearing the mechanical loadings in blood vessels, which also contain smooth muscle cells. Compared to arteries, veins have thinner vessel walls, higher contents of collagenous fibers, and lower contents of smooth muscle cells (Rezakhaniha and Stergiopoulos 2008). Consistent research efforts in academia have been put into developing accurate constitutive models to numerically describe the nonlinear phenomenon exhibited in the loading processes of blood vessels.

Strain energy function (SEF) per unit volume is the preferred method to characterize the nonlinear mechanical properties of vascular tissue. Using the SEF for blood vessels, the constitutive relations can be derived from the SEF. Furthermore, the Cauchy stress and tangent stiffness matrix can be derived from the SEF in order to implement the user-defined material subroutine in a commercial finite element analysis package (Gasser et al. 2006, Sun et al. 2008, Li et al. 2012).

Early SEF frameworks for biological soft tissues are purely phenomenon-based functions, such as the well-known Fung constitutive model (Fung et al. 1979), which is a mathematical function bearing little physiological meaning. Lately, a structure based or perhaps constituent based SEF for arteries was proposed by Holzapfel et al. (2000) to characterize the passive structural responses of the non-collagenous matrix and the collagen fibers. This model treats the non-collagenous material as an isotropic ground matrix, which is reinforced by two families of anisotropic frameworks of collagen fibers. The advantage of this constitutive model over the phenomenon-based SEFs is its ability to completely describe the 3D stress and strain relationship of vascular tissues, and thus a more accurate finite element implementation can be realized.

Based on the classic theories of the fiber-reinforced finite elasticity, the Holzapfel-Gasser-Ogden model has been widely recognized in the active biomechanical research of blood vessels. In the present study, this SEF was adopted for the constitutive modeling of human bridging vein, which is constituted mainly by elastin and collagen. As mentioned above, veins contains less smooth muscle cells than arteries, thus even more striking, the Holzapfel-Gasser-Ogden model is naturally more suitable for the constitutive modeling of vein than the arterial modeling which was initially developed by Holzapfel et al. (2000).

The Holzapfel-Gasser-Ogden model was adopted for the mechanical characterization of human bridging veins in the present study. The strain energy of the bridging vein was constituted by a part W_{iso} associated with isotropic finite deformations and a part W_{aniso} associated with anisotropic finite deformations. W_{iso} , the isotropic part of the overall response of the vessel tissue, represented the non-collagenous matrix in the form

$$W_{iso} = \frac{1}{2}c(I_1 - 3) \quad (7.1)$$

W_{aniso} , the anisotropic part of the overall SEF of vessel wall, arising only from the anisotropic finite deformations of the two families of collagen fibers, had the form

$$W_{aniso} = \frac{k_1}{2k_2} \sum_{i=4,6} \{exp[k_2(I_i - 1)^2] - 1\} \quad (7.2)$$

Hence, the complete strain energy function is given by

$$W = \frac{1}{2}c(I_1 - 3) + \frac{k_1}{2k_2} \sum_{i=4,6} \{exp[k_2(I_i - 1)^2] - 1\} \quad (7.3)$$

where c , k_1 , and k_2 were the effective material parameters. The variables c and k_1 had dimensions of stress, and k_2 was dimensionless. I_1 is the first principal invariant of the right Cauchy-Green deformation tensor derived from the deformation tensor of the vascular material. The

orientations of the two families of collagen fibers were defined by the two unit vectors \mathbf{a}_1 and \mathbf{a}_2 respectively. I_4 and I_6 denoted the squares of the collagen stretches in the directions of \mathbf{a}_1 and \mathbf{a}_2 , respectively. I_4 and I_6 had the final derived forms in terms of the two independent stretches λ and λ_z , and the mean fiber angle β :

$$I_4 = I_6 = \lambda^2 \cos^2 \beta + \lambda_z^2 \sin^2 \beta \quad (7.4)$$

where λ was the radial stretch, λ_z was the axial stretch. The mean fiber angle β was assigned to be 29° for the directions of both unit vectors. The value of β was obtained directly from the value of the collagenous fiber angle of arterial media by Holzapfel et al. (2000) because experimentally detecting the fiber angle of BV was too hard to be performed using the traditional measuring methods such as optical microscopy (Nierenberger et al. 2012).

The determination of the material parameters in the constitutive model used the experimental data obtained using the processes described in section 7.1 above. A pressure versus radius (P - r) curve was generated using the data produced by the conducted pressure-inflation test on the human bridging vein section. To derive the analytical solution of the pressure versus radius relationship corresponding to the vascular inflation test, Cauchy's equation of equilibrium was adopted in the form

$$\text{div} \sigma + \mathbf{b} = 0 \quad (7.5)$$

where $\text{div}(\bullet)$ represented the spatial divergence of tensor field (\bullet), and σ was the Cauchy stress.

In the absence of body forces \mathbf{b} , equation (7.5) had the self-equilibrated form

$$\text{div} \sigma = 0 \quad (7.6)$$

In cylindrical coordinates (r, θ, z) , because of the symmetry, equation (7.6) had only the normal stresses σ_{rr} , $\sigma_{\theta\theta}$, σ_{zz} which were the principal stresses. Thus, equation (7.6) consisted of just the radial equation

$$\frac{d\sigma_{rr}}{dr} + \frac{1}{r}(\sigma_{rr} - \sigma_{\theta\theta}) = 0 \quad (7.7)$$

The conducted inflation test involved the homogeneous pressure P applied to the internal surface of the bridging vein segment with closed ends. Therefore the boundary conditions of the bridging vein were $\sigma_{rr} = -P$ for $r = a$ and $\sigma_{rr} = 0$ for $r = b$, where a was the inner radius, and b was the outer radius. Using the above boundary conditions, integration of equation (7.7) led to the forms

$$P = \int_{\lambda_b}^{\lambda_a} (\lambda^2 \lambda_z - 1)^{-1} \psi'_\lambda d\lambda \quad (7.8)$$

$$\psi'_\lambda = \partial W / \partial \lambda \quad (7.9)$$

where λ_a and λ_b were the values of λ at $r = a$ and $r = b$. The detailed derivations of equation (7.8) can be found in Ogden (2009). The present study considered the bridging vein segment as a thin-walled tube. Following the derivations in Holzapfel and Ogden (2010), equation (7.8) was approximated to be

$$P = \varepsilon \lambda^{-1} \lambda_z^{-1} \psi'_\lambda \quad (7.10)$$

where ε was the ratio of the vessel wall thickness to the internal radius in the unloaded configuration. The bridging vein segment was kept at its *in-vivo* length in the present inflation test, so the axial stretch was 1 in equation (7.10), which provided the necessary analytical equation/relationship of pressure versus circumferential stretch of bridging vein.

The raw experimental data (P - r data) of the conducted inflation test was processed into the form of pressure versus circumferential stretch (P - λ data). With the analytical function for this processed experimental data, the values of the material parameters in the form of Holzapfel-Gasser-Ogden model could be obtained using curve fitting methods.

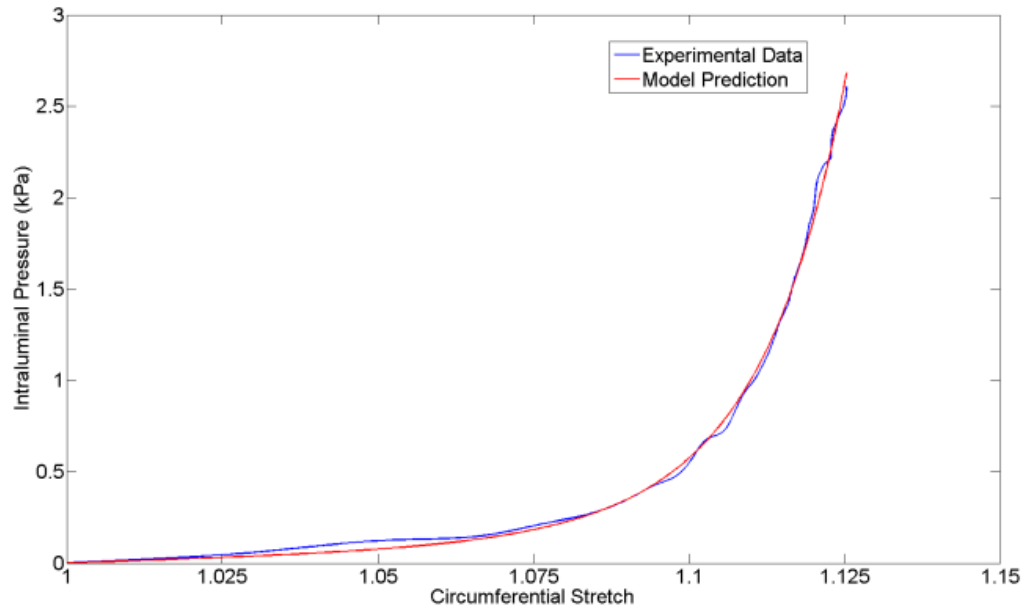


Figure 7-2. Experimental data and analytical solution from fitted material parameters

A modified Levenberg-Marquardt method was used to fit the analytical equation of pressure versus stretch to the P - λ data set. The parameters obtained for equation (7.3) were: $c = 1.203$ kPa, $k_1 = 0.725$ kPa, $k_2 = 87.88$. Table 7-1 summarizes the material parameters of the Holzapfel-Gasser-Ogden model for the tested human bridging vein. The fitted material parameters were adopted in the following finite element analysis of bridging vein.

Table 7-1. Material parameters of human bridging vein

C (kPa)	k_1 (kPa)	k_2 (dimensionless)	B (deg)
1.203	0.725	87.88	29

7.3 INJURY PREDICTION OF SUBDURAL HEMORRHAGE

Specific assumptions were made for the finite element analysis (FEA) of the human bridging vein. First, since the bridging vein connects the superior sagittal sinus and the brain, the effective length of the bridging vein FE model involved in the mechanical responses of the superior sagittal sinus was assumed to be the CSF layer thickness from the skull to the brain at the SSS in the adopted finite element human head model. Therefore the effective length of the bridging vein segment for simulation was determined to be 6.5 mm. The kinematics of human head model in all the foregoing blast-head simulations revealed that there was no skull-brain relative displacement at all for all of the blast-head interaction simulations. Therefore, just the blast-induced peak CSF pressures at SSS were considered to be the mechanical cause of bridging vein damage/rupture.

Note that the simulations of the anterior blast exposures had the highest peak pressure levels in the CSF at the SSS among all the three simulation sets of the horizontal blast-head simulations. Also, the peak CSF pressures at the SSS of the anterior blast-head simulations were identical to that of the room blast-head simulations. Therefore, the maximum positive CSF pressure at the SSS region in each of the five anterior blast-head simulations was assigned to be the intraluminal pressure loading on the bridging vein finite element model. For each of the anterior blast-head simulations, one bridging vein finite element simulation was performed using the respective peak CSF pressure recorded by the gauge No. 2 at SSS (Figure 4-3b). The cross-sectional dimension of the bridging vein model was modeled to be the same as that of the bridging vein segment in the inflation test. The length of the bridging vein finite element model was its effective length, 6.5 mm. The two end surfaces of every bridging vein finite element model were assigned with displacement-fixed boundary conditions. Since the bridging vein was

modeled as a pure cylindrical shell, axis-symmetry was used to simplify the finite element modeling, i.e., only 1/4 of the bridging vein was modeled. The axial yield stress ($\sigma_Y = 1.15$ MPa) and the axial ultimate stress ($\sigma_U = 1.32$ MPa) of human bridging veins were estimated from the BV failure experiments using uniaxial stretching (Monson et al. 2005). Because Monson et al. (2005) stretched the bridging vein samples purely along the cylindrical axis, the vein ultimate stress they found was used as the rupture criteria against the maximum axial Cauchy stress for each of the bridging vein simulations.

Figure 7-3 shows the axial Cauchy stress of the bridging vein finite element analysis corresponding to each of the five impinging BOPs at the blast incident side. Because the axial Cauchy stress from the BV simulations of 291 kPa and 321 kPa BOPs were below the yield stress of the BV, a blast victim was not predicted to be at a great risk of suffering a subdural hemorrhage by these blast levels. In the BV simulation of 349 kPa BOP, the maximum axial Cauchy stress was 1.24 MPa (Figure 7-3), which exceeded the yield stress of bridging veins instead of the ultimate stress. In the BV simulation of 379 kPa BOP, the maximum axial Cauchy stress was just above the ultimate stress of bridging veins. Hence it was concluded that as long as the impinging BOP at the blast incident side exceeded 379 kPa, the bridging vein would definitely rupture.

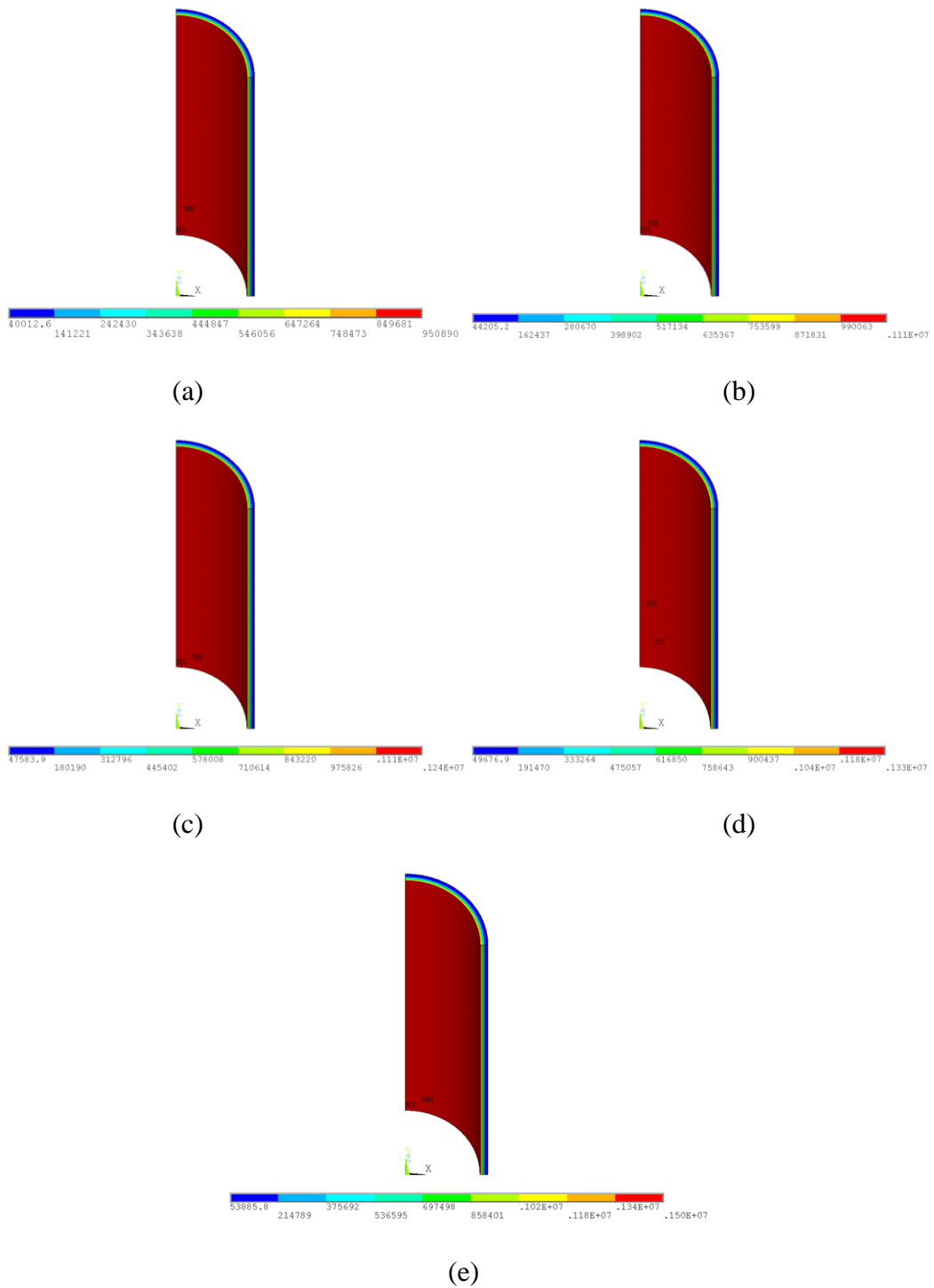


Figure 7-3. Axial Cauchy stress of the bridging vein finite element analysis corresponding to impinging BOP at the blast incident side: (a) 291 kPa, (b) 321 kPa, (c) 349 kPa, (d) 379 kPa, (e) 413 kPa

Although the axial Cauchy stresses which had the maximum value between the yield stress and ultimate stress did not necessarily indicate the occurrences of bridging vein ruptures, yielding of blood vessels could involve fiber failures, which might lead to a later onset of vascular injury. Therefore, the prediction of bridging vein rupture in the present study was based on the criterion of bridging vein yielding. In sum, subdural hemorrhage was predicted to occur once the impinging BOP at the blast incident side exceeded 349 kPa. In other words, a peak blast-induced CSF pressure at the SSS above 220 kPa was estimated to lead to subdural hemorrhage. The impinging BOP at the blast incident side, the respective CSF pressure at the SSS, the induced respective maximum axial Cauchy stress of the bridging vein, and the bridging vein failure prediction for each of the five cases of anterior blast exposure are summarized in Table 7-2.

Table 7-2. Peak pressure tracked by the gauge No. 2 in the CSF at SSS, and the respective maximum axial Cauchy stress and failure prediction of the BV with respect to the impinging BOP at the blast incident side

<i>Peak BOP (TNT weight)</i>	<i>Peak Pressure of Gauge No. 2</i>	<i>BV Maximum Axial Cauchy Stress (MPa)</i>	<i>Failure Prediction</i>
291 kPa (250g)	175 kPa	0.95	No
321 kPa (300g)	202 kPa	1.11	No
349 kPa (350g)	220 kPa	1.24	Yes
379 kPa (400g)	241 kPa	1.33	Yes
413 kPa (450g)	270 kPa	1.50	Yes

8.0 CONCLUSIONS AND DISCUSSIONS

In the present study, a full human head FE model and a numerical blast domain model were created. Three scenarios of blast wave-head interaction simulations were conducted to reproduce the human head exposures to horizontal blast waves from three principal directions, to the ground blasts, and to the blast waves within a room. Five blast-head computer simulations of 250g, 300g, 350g, 400g, and 450g TNT charges at one meter distance were conducted for each of the three scenarios.

In the blast-head simulation scenario involving the horizontal anterior, right lateral, and posterior blast exposures, the sensitivities of the intracranial mechanical responses to blast intensities and exposure orientations were studied. The time-lapse pressure distribution of the brain revealed that the intracranial pressure wave propagated from the proximal blast side to the distal side for any blast orientation. At most of the cerebral locations, the pressure-time histories had an “impulse-like” pattern, which was very obvious at the proximal cerebral sites to the blasts. During the process of intracranial wave propagation from the proximal side to the distal side, attenuation of the pressure amplitude was observed, and the highest pressure levels were found to be at the parts of the brain that were proximal to blast for any blast orientation. On both the proximal side and distal side of the brain exposed to blasts, the positive pressures were much more significant than the negative pressures. The main peak positive pressure and the subsequent peak negative pressure occurred over a very short period of time which was less than 0.8 ms.

This sudden transition from high-level compression to tension might introduce an additional mechanism of axonal injury. This hypothesis also agrees with that was proposed by Taylor and Ford (2009).

The intracranial pressure pattern at the blast proximal site and distal site predicted by the present study was quite different with the "coup and contrecoup" intracranial pressure pattern observed for a human head sustaining impact or acceleration loadings. It is concluded that the direct blast wave propagation into the brain instead of the blast-induced impact generated the propagating intracranial pressure wave. This conclusion was similar to that described in the literature (Moore et al. 2009, Taylor and Ford 2009, Nyein et al. 2010), which excluded the "coup and contrecoup" pattern from the intracranial pressure patterns of bTBI too. But they did not analyze the pressure changes along the pathway of the propagating intracranial wave as we did. We discovered that absorption in the cerebral tissue resulted in decreasing intracranial pressures from the peak at the proximal side of the head along the path of propagation through the brain until the pressure levels were enhanced by the wave concentration effects of the narrow occipital region. The distribution pattern of the blast-induced intracranial pressure is still controversial. Chafi et al. (2009) predicted that the alternating compression and tension occurred at both of the coup and contrecoup sites due to the brain translational and rotational movement which might be attributed to the blast-induced impact. Ganpule et al. (2012) predicted that the typical "coup and contrecoup" pattern occurred at the blast proximal site and the distal site, and that highest positive pressure occurred at the inner parenchyma instead of the proximal cerebral site.

The pressure levels in the cortex were at the side proximal to the blast and the highest levels were found to be due to the lateral blast exposure as compared to the frontal and posterior

blast exposures, indicating that the highest risk in suffering serious cortical injury was obtained by the exposures to the side blast waves. The same conclusion was also derived by Taylor and Ford (2009), who only simulated one blast level of the blast wave with 1.3 MPa peak pressure. The other two references (Moore et al. 2009, Nyein et al. 2010) having the same conclusion with us on the distribution pattern of the blast-induced intracranial pressure, did not investigate the brain responses to the three blast exposure orientations. To our knowledge, the present study is the only one including the human head responses to more than three blast levels for the anterior, right lateral, posterior blast exposure orientations.

It was discovered that the pressure wave invariably traveled into the posterior fossa and vertebral column contents, and caused high pressures in these regions, particularly the lower brainstem and the spinal cord. Among all the fifteen horizontal blast-head simulations, the highest intracranial pressure occurred in the lower brainstem of the posterior exposure. It is found that the narrow regions, such as the foramen magnum, were able to concentrate the pressure waves and thus to enhance the pressure levels there. Therefore, it is speculated that the injury of the brainstem and the spinal cord caused by the pressure wave transmitted into the posterior fossa and the foramen magnum might be one of the primary injury mechanisms of bTBI. We have not found any literature containing a similar point of view on the injury pattern of the brainstem in bTBI.

Besides the above findings on the pressure wave patterns of the brain responses to the blast waves, it was also found that there was a higher possibility that serious cerebral contusion could occur on the side of the brain that was proximal to the blast based on an intracranial pressure injury index published by Ward, et al. (1980). The injury severities of the contusions at several cerebral locations of the horizontal blast-head simulation scenario were predicted with

respect to the impinging BOPs at the blast incident side for each of the exposure orientations. For all the simulation cases of the right lateral blast exposure, serious cortical contusions were predicted to occur. The posterior blast exposure was predicted to be less harmful than the right lateral blast exposure on the cortex, but to be the most harmful orientation to the brainstem, which was predicted to have serious contusion in every simulation case of the posterior orientation. The anterior blast exposure was the least harmful exposure orientation, for which the 291 kPa BOP at the blast incident side was the only case without injury among all the fifteen simulation cases. Chafi et al. (2009) also used this pressure-based contusion criterion to predict blast-induced contusion in their computational study, however, they did not predict specific locations of contusions. To date, the summary of the cerebral contusion in bTBI in the present study is the only one predicting the locations and the injury severities of the blast-induced cerebral contusion with respect to the blast levels and the orientations.

In the evaluation of the shear stress responses of the human brain to the horizontal blast waves, the von-Mises stresses at the lower brainstem and the spinal cord were predicted to be higher than the other intracranial areas for all three blast orientations. The anterior blast exposure was predicted to have the highest magnitude of von-Mises stress among the three orientations. The von-Mises stresses on the cortex regions were found to be much larger than those inside the brain. Despite that blast wave being propagated throughout the brain within 1 ms, the von-Mises stresses of the brain still developed and kept high levels at several cerebral locations over the whole simulation time. Similar to the present study, Taylor and Ford (2009) also predicted that the gray-white matter junction and the inferior regions such as brainstem had high von-Mises stresses and that the von-Mises stresses of the brain continued developing high levels through the whole simulation time. By investigating the maximum shear stress, Chafi et al. (2009) predicted

that high shear stress was initially in the cortical region at the coup site, and then propagated to other areas inside the brain, showing a different pattern than that of the present study. Chafi et al. (2009) also found that the midbrain sustained a small amount of shear stress, which was in agreement with the present study. Chafi et al. (2009) predicted that both the coup and contrecoup sites had the highest shear stress, and that the axonal injury could occur. However, the present study did not predict the highest shear stress at the contrecoup site. Moore et al. (2009) and Ganpule et al. (2012) did not report the shear stress data.

Using the axonal injury tolerance level proposed by Zhang et al. (2004) based on the magnitude of von-Mises shear stress, the present study predicted that shear stress-induced brain injury would not occur under any circumstance of the present numerical simulations. Since both high level pressures and shear stresses occurred on the brainstem or the spinal cord during the blast events, future research attention should be addressed to the detailed injury mechanism of the brainstem and the spinal cord in bTBI, i.e. to perform the microscopic biomechanical analysis of the blast-induced injury there in order to evaluate the combinatorial effect of the pressure impulse and high maintained shear stress.

To date, no other student was found with a similar computational study on the brain responses to the ground blasts and the room blasts. In the simulation scenario of the human exposures to the ground blasts, it was found that the reflections from the ground enhanced the levels of the atmospheric blast waves generated from the same explosive charges as for the horizontal blasts scenario. However, because the distance of the human head and the detonation center for a standing person was longer than one meter, the resultant intracranial pressures and von-Mises stresses were lower than that of the horizontal blasts simulation scenario. Similarly, the cerebral regions that were proximal to the blast waves had higher peak pressures than the

distal regions. At the distal side of the brain including the parietal and occipital cortexes, the peak positive pressures (compression) and the peak negative pressures (tension) took place sequentially with equivalent magnitudes. This kind of compression to tension transition could decrease the injury tolerance of the brain tissue to the high pressures. Similar to the horizontal blast scenario, the high von-Mises stresses also prevailed on the brain surface regions which were adjacent to the CSF. In contrast, the internal parenchyma had very low von-Mises stresses, which were almost negligible. The von-Mises stresses also developed throughout the whole simulation time. With even lower levels of the von-Mises stresses than that of the horizontal blast scenario, it was predicted that the diffuse axonal injury would not occur in the ground blast-head scenario.

In the simulation scenario where the human exposures were to blast waves traveling in a room, it was predicted that the wall-reflected blast waves induced high level intracranial pressures. At the posterior cerebral regions, the levels of the wave reflections-induced positive pressures were even higher than the positive pressures induced by the initial blast waves. Although the wave reflection-induced peak positive pressures at the other cerebral regions were not predicted to be higher than those induced by the initial blast waves, the occurrence of more high-pressure fluctuations in these regions was conjectured to decrease the brain tolerance to contusion. Based only on the peak positive pressures, most of the cerebral regions had the same contusion injury severity as for the anterior blast-head simulations, except the occipital cortex, which had a peak positive pressure higher than the threshold of minor contusion for the 349 kPa BOP case due to the reflected blast waves impinging on the back of head. The levels of the von-Mises stresses were enhanced by the reflected blast waves in a number of cerebral regions, but the diffuse axonal injury was still not predicted to appear.

The susceptibility to subdural hemorrhages, induced by human bridging vein failure as a result of blast injury, was studied through finite element simulations on a vein submodel. In every blast-head scenario, the relative skull-brain motion was predicted to be minimal (< 0.01 mm) in the primary blast loading events. High blast-induced intracranial pressures at SSS rather than relative skull-brain motion (excessive shear stresses) were found to be the main injury mechanism of blast-induced subdural hemorrhage. The outputs (CSF pressure at the SSS) of the five blast-head simulations for the anterior blast exposure, possessing the highest level of CSF pressure at the SSS among all the blast-head simulation scenarios, served as the loading conditions for the separate finite element model of the bridging vein. Results from the BV finite element analysis predicted that blast waves of 379 kPa impinging BOP at the blast incident side in an open-space would lead to bridging vein rupture, since the resulting maximum axial Cauchy stress exceeded the ultimate stress of the BV. Although the 349 kPa BOP case did not lead to a complete BV rupture, the resultant maximum axial Cauchy stress reached the axial yield stress of BV, suggesting an irreversible damage of the fibers of the BV. So, the yielding of the BV may also lead to subdural hemorrhage. Therefore, a more conservative estimation of the injury threshold of the blast subdural hemorrhage was 349 kPa BOP at the blast-incident side of the human head.

Future improvements to the modeling are planned. Since the BV material constitutive model is only based on one sample of BV, more BV samples will be tested for a better estimation of material parameters. Experimental techniques to measure the zero-stress-state of vessels and the longitudinal force (Jankowski et al. 2004) in the inflation test will be adopted to get a more accurate estimation of the BV mechanical properties. In addition, more geometric details can be added to the head model such as the falx and tentorium cerebelli, and the

separation of white matter, gray matter, cerebellum, and brainstem. The separate constitutive modeling of the white matter and gray matter will be considered once the separate geometric modeling between them is accomplished. And the future finite element head model would be validated against more cadaveric head experiments.

In sum, the understanding of cerebral mechanical responses to the blasts in the various cases along with the injury predictions of contusion and subdural hemorrhage in the present study were essential for improving the medical care of bTBI and for developing the next-generation protective gear to better protect people from blasts.

BIBLIOGRAPHY

ANSYS (2012). <http://www.ansys.com>.

AUTODYN (2003). Theory Manual Revision 4.3, Concord, CA: Century Dynamics, Inc.

Bauman, R. A., G. Ling, L. Tong, A. Januszkiewicz, D. Agoston, N. Delanerolle, Y. Kim, D. Ritzel, R. Bell, J. Ecklund, R. Armonda, F. Bandak and S. Parks (2009). "An introductory characterization of a combat-casualty-care relevant swine model of closed head injury resulting from exposure to explosive blast." J Neurotrauma **26**(6): 841-860.

Belytschko, T., W. K. Liu and B. Moran (2000). Nonlinear finite elements for continua and structures, Wiley.

Benzinger, T. L., D. Brody, S. Cardin, K. C. Curley, M. A. Mintun, S. K. Mun, K. H. Wong and J. R. Wrathall (2009). "Blast-related brain injury: imaging for clinical and research applications: report of the 2008 st. Louis workshop." J Neurotrauma **26**(12): 2127-2144.

BrainSuite (2011). <http://www.loni.ucla.edu/Software/BrainSuite>.

Chafi, M. S., G. Karami and M. Ziejewski (2009). "Biomechanical Assessment of Brain Dynamic Responses Due to Blast Pressure Waves." Annals of Biomedical Engineering **38**(2): 490-504.

Chen, Y. and W. Huang (2011). "Non-impact, blast-induced mild TBI and PTSD: concepts and caveats." Brain injury **25**(7-8): 641-650.

Chen, Y. and M. Ostojca-Starzewski (2010). "MRI-based finite element modeling of head trauma: spherically focusing shear waves." Acta Mechanica **213**(1-2): 155-167.

Cheng, J., J. Gu, Y. Ma, T. Yang, Y. Kuang, B. Li and J. Kang (2010). "Development of a rat model for studying blast-induced traumatic brain injury." Journal of the Neurological Sciences **294**(1-2): 23-28.

Cooper, P. W. (1996). Explosives engineering, Wiley-VCH.

DePalma, R. G., D. G. Burris, H. R. Champion and M. J. Hodgson (2005). "Blast injuries." N Engl J Med **352**(13): 1335-1342.

Depreitere, B., C. Van Lierde, J. V. Sloten, R. Van Audekercke, G. Van der Perre, C. Plets and J. Goffin (2006). "Mechanics of acute subdural hematomas resulting from bridging vein rupture." J Neurosurg **104**(6): 950-956.

El Sayed, T., A. Mota, F. Fraternali and M. Ortiz (2008). "Biomechanics of traumatic brain injury." Computer Methods in Applied Mechanics and Engineering **197**(51): 4692-4701.

Elder, G. A. and A. Cristian (2009). "Blast-related mild traumatic brain injury: mechanisms of injury and impact on clinical care." Mt Sinai J Med **76**(2): 111-118.

Elsayed, T., A. Mota, F. Fraternali and M. Ortiz (2008). "Biomechanics of traumatic brain injury." Computer Methods in Applied Mechanics and Engineering **197**(51-52): 4692-4701.

Fairlie, G. (1998). The numerical simulation of high explosives using AUTODYN-2D & 3D. Expro '98, Institute of Explosive Engineers 4th Biannual Symposium.

Feng, Y., T. M. Abney, R. J. Okamoto, R. B. Pless, G. M. Genin and P. V. Bayly (2010). "Relative brain displacement and deformation during constrained mild frontal head impact." Journal of The Royal Society Interface **7**(53): 1677-1688.

Friedlander, F. G. (1976). The wave equation on a curved space-time, Cambridge university press.

Fung, Y. C., K. Fronek and P. Patitucci (1979). "Pseudoelasticity of arteries and the choice of its mathematical expression." Am J Physiol **237**(5): H620-631.

Ganpule, S., A. Alai, E. Plougonven and N. Chandra (2012). "Mechanics of blast loading on the head models in the study of traumatic brain injury using experimental and computational approaches." Biomechanics and Modeling in Mechanobiology.

Gasser, T. C., R. W. Ogden and G. A. Holzapfel (2006). "Hyperelastic modelling of arterial layers with distributed collagen fibre orientations." Journal of The Royal Society Interface **3**(6): 15-35.

Gennarelli, T. A. and L. E. Thibault (1982). "Biomechanics of acute subdural hematoma." J Trauma **22**(8): 680-686.

Grujicic, M., W. C. Bell, B. Pandurangan and P. S. Glomski (2010). "Fluid/Structure Interaction Computational Investigation of Blast-Wave Mitigation Efficacy of the Advanced Combat Helmet." Journal of Materials Engineering and Performance.

Grujicic, M., W. C. Bell, B. Pandurangan and T. He (2010). "Blast-wave impact-mitigation capability of polyurea when used as helmet suspension-pad material." Materials & Design **31**(9): 4050-4065.

Han, H., W. Tao and M. Zhang (2007). "The dural entrance of cerebral bridging veins into the superior sagittal sinus: an anatomical comparison between cadavers and digital subtraction angiography." Neuroradiology **49**(2): 169-175.

Hardman, J. M. and A. Manoukian (2002). "Pathology of head trauma." Neuroimaging Clin N Am **12**(2): 175-187, vii.

Hiermaier, S. (2008). Structures Under Crash and Impact: Continuum Mechanics, Discretization and Experimental Characterization, Springer.

Hoffer, M. E., C. Balaban, R. Nicholas, D. Marcus, S. Murphy and K. Gottshall (2013). "Neurosensory Sequelae of Mild Traumatic Brain Injury." Psychiatric Annals **43**(7): 318-323.

Hoffer, M. E., C. Balaban, M. D. Slade, J. W. Tsao and B. Hoffer (2013). "Amelioration of Acute Sequelae of Blast Induced Mild Traumatic Brain Injury by N-Acetyl Cysteine: A Double-Blind, Placebo Controlled Study." PLoS ONE **8**(1): e54163.

Hoffer, M. E., C. D. Balaban, K. R. Gottschall, B. J. Balough, M. R. Maddox and J. R. Penta (2010). "Blast exposure: vestibular consequences and associated characteristics." Otology & Neurotology **31**: 232-236.

Hoge, C. W., D. McGurk, J. L. Thomas, A. L. Cox, C. C. Engel and C. A. Castro (2008). "Mild traumatic brain injury in U.S. Soldiers returning from Iraq." N Engl J Med. **358**: 453-463.

Holzapfel, G. A., T. C. Gasser and R. W. Ogden (2000). "A new constitutive framework for arterial wall mechanics and a comparative study of material models." Journal of Elasticity **61**(1): 1-48.

Holzapfel, G. A. and R. W. Ogden (2010). "Constitutive modelling of arteries." Proceedings of the Royal Society A: Mathematical, Physical and Engineering Sciences **466**(2118): 1551-1597.

Horgan, T. and M. Gilchrist (2003). "The creation of three-dimensional finite element models for simulating head impact biomechanics." International Journal of Crashworthiness **8**(4): 353-366.

Hughes, T. J. R. (2000). The finite element method: linear static and dynamic finite element analysis, Dover Publications.

ICBM (2011). www.loni.ucla.edu/ICBM.

Jankowski, R. J., R. L. Prantil, M. O. Fraser, M. B. Chancellor, W. C. De Groat, J. Huard and D. A. Vorp (2004). "Development of an experimental system for the study of urethral biomechanical function." Am J Physiol Renal Physiol **286**(2): F225-232.

Kleiven, S. (2006). "Evaluation of head injury criteria using a finite element model validated against experiments on localized brain motion, intracerebral acceleration, and intracranial pressure." International Journal of Crashworthiness **11**(1): 65-79.

Kocsis, J. D. and A. Tessler (2009). "Pathology of blast-related brain injury." The Journal of Rehabilitation Research and Development **46**(6): 667.

Lee, E., M. Finger and W. Collins (1973). JWL equation of state coefficients for high explosives. Other Information: Orig. Receipt Date: 31-DEC-73; Medium: ED; Size: Pages: 8.

Lee, E., H. Hornig and J. Kury (1968). ADIABATIC EXPANSION OF HIGH EXPLOSIVE DETONATION PRODUCTS, California Univ., Livermore. Lawrence Radiation Lab.

Li, D., A. M. Robertson, G. Lin and M. Lovell (2012). "Finite element modeling of cerebral angioplasty using a structural multi-mechanism anisotropic damage model." International Journal for Numerical Methods in Engineering **92**(5): 457-474.

Ling, G., F. Bandak, R. Armonda, G. Grant and J. Ecklund (2009). "Explosive blast neurotrauma." J Neurotrauma **26**(6): 815-825.

Long, J. B., T. L. Bentley, K. A. Wessner, C. Cerone, S. Sweeney and R. A. Bauman (2009). "Blast overpressure in rats: recreating a battlefield injury in the laboratory." J Neurotrauma **26**(6): 827-840.

Materialise (2011). <http://biomedical.materialise.com/mimics>.

McAllister, T. W. (2011). "Neurobiological consequences of traumatic brain injury." Dialogues Clin Neurosci **13**(3): 287-300.

Miller, K. (1999). "Constitutive model of brain tissue suitable for finite element analysis of surgical procedures." J Biomech **32**(5): 531-537.

Monea, A. G., I. Verpoest, J. Vander Sloten, G. Van der Perre, J. Goffin and B. Depreitere (2012). "Assessment of Relative Brain-Skull Motion in Quasistatic Circumstances by Magnetic Resonance Imaging." Journal of Neurotrauma **29**(13): 2305-2317.

Monson, K., W. Goldsmith, N. Barbaro and G. Manley (2005). "Significance of source and size in the mechanical response of human cerebral blood vessels." Journal of Biomechanics **38**(4): 737-744.

- Moore, D. F., A. Jérusalem, M. Nyein, L. Noels, M. S. Jaffee and R. A. Radovitzky (2009). "Computational biology — Modeling of primary blast effects on the central nervous system." NeuroImage **47**: T10-T20.
- Moss, W., M. King and E. Blackman (2009). "Skull Flexure from Blast Waves: A Mechanism for Brain Injury with Implications for Helmet Design." Physical Review Letters **103**(10).
- Murthy, J. M., J. S. Chopra and D. R. Gulati (1979). "Subdural hematoma in an adult following a blast injury. Case report." J Neurosurg **50**(2): 260-261.
- Nahum, A. M., R. Smith and C. C. Ward (1977). "Intracranial Pressure Dynamics During Head Impact." Proceedings of the 21st Stapp Car Crash Conference, Society of Automotive Engineers, Inc., Warrendale, PA: 339-366.
- Nierenberger, M., R. Wolfram-Gabel, S. Decock-Catrin, N. Boehm, Y. Rémond, J.-L. Kahn and S. Ahzi (2012). "Investigation of the human bridging veins structure using optical microscopy." Surgical and Radiologic Anatomy.
- Ning, X., Q. Zhu, Y. Lanir and S. S. Margulies (2006). "A Transversely Isotropic Viscoelastic Constitutive Equation for Brainstem Undergoing Finite Deformation." Journal of Biomechanical Engineering **128**(6): 925.
- Nyein, M. K., A. M. Jason, L. Yu, C. M. Pita, J. D. Joannopoulos, D. F. Moore and R. A. Radovitzky (2010). "In silico investigation of intracranial blast mitigation with relevance to military traumatic brain injury." Proceedings of the National Academy of Sciences **107**(48): 20703-20708.
- Ogden, R. (2009). Anisotropy and Nonlinear Elasticity in Arterial Wall Mechanics. Biomechanical Modelling at the Molecular, Cellular and Tissue Levels. G. Holzapfel and R. Ogden, Springer Vienna. **508**: 179-258.
- Pang, Q., X. Lu, H. Gregersen, G. von Oettingen and J. Astrup (2001). "Biomechanical properties of porcine cerebral bridging veins with reference to the zero-stress state." J Vasc Res **38**(1): 83-90.
- Panzer, M. B., B. S. Myers, B. P. Capehart and C. R. Bass (2012). "Development of a Finite Element Model for Blast Brain Injury and the Effects of CSF Cavitation." Annals of Biomedical Engineering **40**(7): 1530-1544.
- Prevost, T. P., A. Balakrishnan, S. Suresh and S. Socrate (2011). "Biomechanics of brain tissue." Acta Biomaterialia **7**(1): 83-95.
- Rafaels, K., C. R. Dale Bass, R. S. Salzar, M. B. Panzer, W. Woods, S. Feldman, T. Cummings and B. Capehart (2011). "Survival Risk Assessment for Primary Blast Exposures to the Head." J Neurotrauma.

Rezakhaniha, R. and N. Stergiopoulos (2008). "A Structural Model of the Venous Wall Considering Elastin Anisotropy." Journal of Biomechanical Engineering **130**(3): 031017.

Ruan, J. S. (1994). Impact biomechanics of head injury by mathematical modeling. 9519955 Ph.D., Wayne State University.

Ruan, J. S. and P. Prasad (1995). "Coupling of a finite element human head model with a lumped parameter Hybrid III dummy model: preliminary results." J Neurotrauma **12**(4): 725-734.

Saljo, A., F. Arrhen, H. Bolouri, M. Mayorga and A. Hamberger (2008). "Neuropathology and pressure in the pig brain resulting from low-impulse noise exposure." J Neurotrauma **25**(12): 1397-1406.

Santelices, L. C., S. J. Calano, J. C. Erhart, R. L. Prantil, J. L. Haney, D. A. Vorp and J. M. Ahearn (2007). "Experimental system for ex vivo measurement of murine aortic stiffness." Physiol Meas **28**(8): N39-49.

Shen, F., T. E. Tay, J. Z. Li, S. Nigen, P. V. S. Lee and H. K. Chan (2006). "Modified Bilston Nonlinear Viscoelastic Model for Finite Element Head Injury Studies." Journal of Biomechanical Engineering **128**(5): 797.

Shuck, L. Z. and S. H. Advani (1972). "Rheological Response of Human Brain Tissue in Shear." ASME Journal of Basic Engineering **94**: 905-911.

Sporns, O., R. H. Kraft, P. J. McKee, A. M. Dagro and S. T. Grafton (2012). "Combining the Finite Element Method with Structural Connectome-based Analysis for Modeling Neurotrauma: Connectome Neurotrauma Mechanics." PLoS Computational Biology **8**(8): e1002619.

Sun, W., E. L. Chaikof and M. E. Levenston (2008). "Numerical Approximation of Tangent Moduli for Finite Element Implementations of Nonlinear Hyperelastic Material Models." Journal of Biomechanical Engineering **130**(6): 061003.

Sundaramurthy, A., A. Alai, S. Ganpule, A. Holmberg, E. Plougonven and N. Chandra (2012). "Blast-Induced Biomechanical Loading of the Rat: An Experimental and Anatomically Accurate Computational Blast Injury Model." Journal of Neurotrauma **29**(13): 2352-2364.

Taber, K. H., D. L. Warden and R. A. Hurley (2006). "Blast-related traumatic brain injury: what is known?" J Neuropsychiatry Clin Neurosci **18**(2): 141-145.

Tanielian, T. L. and L. H. Jaycox (2008). Invisible wounds of war: Psychological and cognitive injuries, their consequences, and services to assist recovery, Rand Corporation.

Taylor, P. A. and C. C. Ford (2009). "Simulation of Blast-Induced Early-Time Intracranial Wave Physics leading to Traumatic Brain Injury." Journal of Biomechanical Engineering **131**(6): 061007.

- Terrio, H., L. A. Brenner, B. J. Ivins, J. M. Cho, K. Helmick, K. Schwab, K. Scally, R. Bretthauer and D. Warden (2009). "Traumatic brain injury screening: preliminary findings in a US Army Brigade Combat Team." J Head Trauma Rehabil. **24**: 14-23.
- Van Leer, B. (1977). "Towards the ultimate conservative difference scheme. IV. A new approach to numerical convection." Journal of computational physics **23**(3): 276-299.
- Van Leer, B. (1979). "Towards the ultimate conservative difference scheme. V. A second-order sequel to Godunov's method." Journal of computational physics **32**(1): 101-136.
- VanEpps, J. S., R. Londono, A. Nieponice and D. A. Vorp (2009). "Design and validation of a system to simulate coronary flexure dynamics on arterial segments perfused ex vivo." Biomech Model Mechanobiol **8**(1): 57-66.
- Wang, C., J. B. Pahk, C. D. Balaban, J. Muthu, D. A. Vorp, M. C. Miller and J. S. Viperman (2012). Biomechanical Assessment of The Bridging Vein Rupture of Blast-Induced Traumatic Brain Injury Using The Finite Element Human Head Model. Proceedings of IMECE 2012, ASME.
- Wang, C., J. B. Pahk, C. D. Balaban and J. S. Viperman (2011). Computational Study on the Bridging Vein Rupture of Blast-Induced Traumatic Brain Injury Using a Numerical Human Head Model. Proceedings of IMECE 2011, ASME.
- Ward, C. C., M. Chan and A. M. Nahum (1980). "Intracranial Pressure-A Brain Injury Criterion." Proceedings, 24th Stapp Car Crash Conference, SAE Paper No. 801304.
- Willinger, R., H.-S. Kang and B. Diaw (1999). "Three-dimensional human head finite-element model validation against two experimental impacts." Annals of Biomedical Engineering **27**(3): 403-410.
- Yamashima, T. and R. Friede (1984). "Why do bridging veins rupture into the virtual subdural space?" Journal of Neurology, Neurosurgery & Psychiatry **47**(2): 121-127.
- Zalesak, S. T. (1979). "Fully multidimensional flux-corrected transport algorithms for fluids." Journal of computational physics **31**(3): 335-362.
- Zhang, L., K. H. Yang and A. I. King (2001). "Comparison of Brain Responses Between Frontal and Lateral Impacts by Finite Element Modeling." Journal of Neurotrauma **18**.
- Zhang, L., K. H. Yang and A. I. King (2004). "A Proposed Injury Threshold for Mild Traumatic Brain Injury." Journal of Biomechanical Engineering **126**(2): 226.